NASA-CR-201402

Annual Status Report

Project Title: Theoretical and Global Scale Model Studies of the Atmospheric Sulfur/Aerosol System
Project Number: NAGW-4908 (formerly NAGW-3770)
Project Director: Prasad Kasibhatla
Performance Period: 7/1/95 - 6/30/96

Phase III Activities

The primary focus during the third-phase of our on-going multi-year research effort has been on 3 activities, supported either wholly or in part by this Grant. These are:

1) A global-scale model study of the anthropogenic component of the tropospheric sulfur cycle;.

2) Process-scale model studies of the factors influencing the distribution of aerosols in the remote marine atmosphere; and

3) An investigation of the mechanism of the OH-initiated oxidation of DMS in the remote marine boundary layer.

In the following sections, we describe in more detail our research activities in each of these areas.

Global Model Studies of the Anthropogenic Sulfur cycle in the Troposphere

This aspect of our research focuses on quantifying the ability of the current generation of global chemical transport models (GCTMs) to reproduce regional and seasonal patterns in observed sulfate concentrations. The significance of such an analysis stems from the fact that results from these models are used to estimate the direct and indirect radiative forcing due to sulfate aerosols.

To address this issue, we have simulated the present-day distribution of anthropogenic sulfate using the GFDL global chemistry and transport model (GCTM). The GCTM has a horizontal resolution of ~265 km, and is driven using meteorological fields from a general circulation model. The most up-to-date, seasonally-varying anthropogenic sulfur emission inventory from the IGAC/GEIA project is used in this study. Parameterizations for dry deposition, precipitation scavenging of soluble gases and aerosols, and gas-phase and in-cloud oxidation of SO2 to sulfate, are included in the GCTM. A key feature of our study is the evaluation of model results against surface SOx concentration and wet deposition data from a network of stations in

North America and Europe. We find that the model results agree best with the measurements only when a non-photochemical pathway for the conversion of SO2 to sulfate in included in the model. We propose that this additional oxidation pathway may be related to heterogeneous reactions between SO2 and atmospheric aerosols that typically are not included in models of the atmospheric sulfur cycle. Despite this improvement, we find that while the model is generally able to reproduce the seasonal cycle of surface sulfate in North America, it is unable to reproduce the absence of a significant seasonal cycle in the western and central European sulfate measurements. iOur results therefore suggest that significant uncertainties remain in model-calculated global sulfate burdens, and therefore in the estimated radiative forcing of anthropogenic sulfate aerosols. We have also analyzed the factors governing the seasonal evolution of the anthropogenic sulfate burden in various regions of the NH mid-latitudes, and find that the amplitude of this seasonal cycle is significantly affected by the modeled seasonal amplitude in aqueous-phase sulfate production rates. It is therefore important that improved treatments of aqueous-phase chemistry be included in GCTMs used to study the global sulfate budget.

The results from this study have been documented in a manuscript (attached in Appendix A) that has been submitted to the *J. Geophys. Res.*.

Model Studies of Marine Boundary Layer Aerosols

This aspect of our research focuses on the development and application of a detailed box model to simulate the formation, growth, and removal of H2SO4-H2O aerosols in the marine boundary layer. In this model, the aerosol distribution is discretized using a finite number of uni-modal size bins, in a manner similar to the AERO2 model (*Raes et al.*, 1992). An attractive feature of our model is that the number and sizes of the individual bins are user specified parameters. Physical processes described in the model include formation of new particles by nucleation, condensational growth of newly formed and pre-existing particles, and coagulation between particles of different sizes. In it's current configuration, the rate of nucleation is calculated using the hydrate theory of *Jaeker-Voirol and Mirabel* (1989) and a user specified nucleation tuner (*Raes et al.*, 1992), with the size of the newly formed particles being a user-specified parameter. The growth of particles by co-condensation of H2SO4 and H2O is assumed to be limited by the rate of H2SO4 condensation, which is calculated using the modified Fuchs-Sutugin formulation (*Hegg*, 1990; *Kreidenweis et al.*, 1991), Coagulation coefficients between particles of different sizes are

calculated using the expression given by *Seinfeld* (1986). Simplified treatments of particle dry deposition and processing by clouds are also included in the model.

We have used this model to examine whether in situ sulfate particle production and growth can explain CN and CCN number concentrations in the marine boundary layer. Specifically, we have examined the hypothesis by *Pandis et al.* (1994) and *Russell et al.* (1995) that there is a linear relationship between DMS fluxes and marine boundary-layer CCN concentrations. This hypothesis was based on results from a model which used a simplified, bimodal representation of aerosol dynamics. Our results suggest that while the bimodal model reproduces certain aspects simulated in the more detailed bin model, it does not fully capture the time-scales over which the aerosol size-distribution evolves. Under certain conditions, this may lead to significant biases in the results from the bimodal model. Further analysis of these results is currently underway.

Studies of the OH-initiated DMS oxidation mechanism

In a parallel effort, Dr. Doug Davis is spearheading our efforts to develop and evaluate a detailed mechanism for the OH-initiated oxidation of DMS. One aspect of this effort has focussed on an analysis of sulfur field data-sets from two distinctively different marine boundary-layer environments: one involving a high-temperature, tropical setting (Christmas Island. 3N, 157W), and the other involving a very low-temperature, high-latitude setting (Palmer Station, Antarctica, 64S, 60W). These datasets are being used to help set boundaries on the rate coefficients for critical steps in the very complex OH-initiated oxidation of DMS.

The high-temperature tropical study has now established with a high degree of confidence that the dominant OH-abstraction reaction channel (~75%), although involving several as yet uncharacterized intermediate steps, does form SO_2 with 85±15 % efficiency. At this specific tropical site, therefore, boundary-layer SO_2 levels are virtually totally controlled by DMS oxidation. This represents the first time that this has been demonstrated in a marine environment. This same dataset has also shown quite convincingly that chlorine oxidation of DMS in a tropical setting is a very minor pathway (<15%) relative to oxidation by OH.

Concerning the low-temperature Antarctic study, these results indicate that the dominant OH reaction channel is addition, as indicated by earlier kinetic studies. We find, however, that as much as 15% of the addition reaction channel goes directly to $DMSO_2$ rather than DMSO. Our results also strongly suggest that the stable oxidation product MSA is predominantly formed via

the addition channel and not the abstraction channel. The lifetimes of DMSO, DMSO2, MSA, and H2SO4 in this marine boundary layer environment was estimated to be typically less than 2 hours due to surface and particle scavenging. We also find that, in the summertime Antarctic environment, approximately half of the DMS released in the marine boundary-layer is transported via shallow convection processes to the lower the lower and middle free troposphere, where it is oxidized to reservoir species. Still later it is returned to the boundary-layer in very non-uniform blobs at which time the mixing ratios of oxidation products such as DMSO and DMSO2 can be observed to increase by factors of 10 to 15. This is an important finding in that the product distribution in the lower free troposphere can be quite different from that in the boundary-layer. This follows from the fact that there are lower temperatures in the former regime, and due to the fact that DMSO (which is the major initial oxidation product from DMS) can undergo further chemistry via its reaction with OH, rather than being removed by physical processes.

Other Activities

In addition to the activities described above, this project has provided partial funding for our participation in: a) the development and application of a new-generation, assimilated-meteorology driven GCTM at NASA/GSFC, and b) an international intercomparison of short-lived tracer transport in GCTMs. Manuscripts describing the results from these activities have been submitted to the *J. Geophys. Res.*, and are included in Appendix B and C, respectively.

Planned Phase IV Activities

A major portion of our activities during the fourth and final phase of this project will involve the preparation and submission of manuscripts describing the results from our model studies of marine boundary-layer aerosols and DMS-oxidation mechanisms. It is anticipated that two papers describing the results from the marine boundary-layer aerosol studies, and two papers describing the DMS-oxidation study results will be submitted in the next few months.

We will then couple the aerosol dynamics model to the DMS-oxidation model, and use the coupled model to further analyze the Christmas Island and Antarctic datasets. We will also attempt to perform preliminary analysis on the ACE-1 dataset provided that it is becomes available in the near future. In addition, we plan to investigate the sensitivity of model results to

the functional form of the rate expression used to calculate the nucleation of marine H_2SO_4-H_2O aerosols. This may be important because recent measurements indicate that the rate of nucleation may be kinetically rather than thermodynamically controlled.

We will also initiate an effort to incorporate the representation of SOx emissions, transport, chemistry, and removal, directly into a regional climate model (RegCM2) with the ultimate goal of better characterizing the regional effect of sulfate aerosols on climate.

APPENDIX A

A THREE-DIMENSIONAL GLOBAL MODEL INVESTIGATION OF SEASONAL VARIATIONS IN THE ATMOSPHERIC BURDEN OF ANTHROPOGENIC SULFATE AEROSOLS

.

P. Kasibhatla[1]

W. L. Chameides[2]

and

J. St. John[2]

1. MCNC/Environmental Programs, Suite 112, 200 Park Office Building, Research Triangle Park, NC 27709, USA

2. School of Earth and Atmospheric Sciences, Georgia Institute of Technology, Atlanta, GA 30332, USA

ABSTRACT

A global three-dimensional chemical transport model is used to investigate seasonal variations of anthropogenic sulfur in the troposphere. Particular emphasis is placed on detailed comparisons of the modeled surface sulfur dioxide (SO_2) and sulfate (SO_4) concentrations, and sulfate wet deposition fluxes with measurements from the EMEFS and EMEP field programs in North America and Europe, respectively. Initial comparisons of model results with measurements reveal a systematic tendency of the model to overestimate SO_2 concentrations and underestimate SO_4 concentrations, while producing a reasonable fit to measured wet deposition fluxes. Through a series of sensitivity tests, we find that the addition of a non-photochemical pathway for converting SO_2 to SO_4 in the boundary layer with a pseudo first-order rate of constant of 1-2 x 10^{-6} s^{-1} provides the most reasonable method of bringing the model results into better agreement with the EMEFS and EMEP datasets. We propose that this additional pathway may be related to heterogeneous reactions between SO_2 and atmospheric aerosols that typically are not included in models of the atmospheric sulfur cycle. Despite the vastly improved simulation of surface SO_2 and SO_4 when this hypothetical heterogeneous oxidation pathway is included, the model is unable to simultaneously simulate the large seasonal cycle in surface SO_4 observed North America and the almost total absence of a seasonal cycle in surface SO_4 over Europe. The seasonal cycle in model-predicted column SO_4 burdens are similar to but not identical to those for surface SO_4 because of regional differences in transport, free tropospheric oxidation and in-cloud removal. We find that the summer-to-winter ratio in column SO_4 is larger over eastern North America than it is over Europe; however both are larger than that for eastern Asia, where wintertime column SO_4 is predicted to exceed summertime column SO_4.

1. INTRODUCTION

The environmental and climatic consequences of anthropogenic sulfur emissions have been the subject of much scientific debate in recent years. In the 1970's and 1980's, the discussion centered around the deleterious effects of "acid rain" and visibility degradation in and downwind of industrial regions in the United States and Europe, where emissions of sulfur gases from fossil-fuel combustion are most intense (*OECD, 1977; NAPAP, 1990*). More recently, the suggestion that atmospheric sulfate particles may significantly affect climate (*Bolin and Charlson, 1976; Twomey et al., 1984; Charlson et al., 1987, 1991, 1992*), has provided the impetus for a renewed interest in the global aspects of the tropospheric sulfur cycle. In this context, it is particularly important to assess the spatial and temporal impact of anthropogenic emissions on the atmospheric sulfur cycle, and the subsequent effect of this anthropogenic component on the radiative balance of the atmosphere.

Several investigators have attempted to address this question using three-dimensional, global chemical transport models (GCTMs). *Langner and Rodhe* (1991) presented the first such study, and a similar study has been performed by *Pham et al.* (1995). While these studies provide useful insights into aspects of the global sulfur cycle, they are based on models which are driven by monthly-mean, rather than synoptically-varying, meteorological fields. Studies using more sophisticated GCTMs have recently been performed by *Taylor and Penner* (1994), *Chin et al.* (1996), and *Feichter et al.* (1996).

In this study, we present results of model simulations of the anthropogenic sulfur cycle, using a GCTM similar in character to the models used by *Taylor and Penner* (1994), *Chin et al.* (1996), and *Feichter et al.* (1996). Our model is distinguished from these previous works in two important aspects. The first is the inclusion of a detailed evaluation of model results against

simultaneous regional air chemistry and deposition measurements. This evaluation allows us to more robustly assess the uncertainties inherent in the sulfate distributions derived from present-day GCTMs and to identify potential shortcomings in their chemical algorithms

The other unique aspect of this study is the focus on the seasonal-cycle in the simulated burden of anthropogenic sulfate, an issue which has received surprisingly little attention in previous GCTM studies. The seasonal variation of the column sulfate burden can have a significant effect on the direct radiative forcing of sulfate aerosols. Clearly, the month-to-month variation in radiative forcing depends on the monthly variation in sulfate aerosol loading. For example, *Haywood and Shine* (1995) calculated the global-mean radiative forcing in each month using modeled sulfate aerosol distributions from *Langner and Rodhe* (1991) and *Taylor and Penner* (1994). The *Taylor and Penner* (1994) distribution, which has a larger seasonal variation, yielded 20-30% more forcing in summer, and 20-30% less forcing in winter, than that obtained using the *Langner and Rodhe* (1991) distribution.

Interesting seasonal effects may also occur on regional scales in the industrialized regions of the northern mid-latitudes. For example, observations of surface sulfate concentrations in the eastern United States show a strong seasonal cycle in phase with the seasonal cycle in solar insolation (i.e, maxima in the summer and minima in the winter) [*Shaw and Paur, 1983*], while a similar seasonal cycle is largely absent or even reversed in the industrialized regions of western and central Europe (*Feichter et al., 1996*). If these seasonal variations in surface sulfate reflect seasonal variations in column sulfate, then the annually-averaged direct radiative cooling from sulfate aerosols over the two regions would be quite different even if the annually-averaged column sulfate burden is the same in the two regions. Over the eastern United States, the seasonal cycle in sulfate aerosol will tend to amplify the annual-mean radiative forcing, while there will be

no such effect over Europe. Recognizing the fact that much of the direct radiative forcing from anthropogenic sulfate is believed to occur in these two regions (*Charlson et al., 1991; Kiehl and Brieglib, 1993*), our ability to simulate the seasonal variability in sulfur over these regions provides a critical test of the reliability of present-day assessments of the climatic effects of anthropogenic sulfate aerosols.

2. MODEL DESCRIPTION

The GCTM used in this study was originally developed at the Geophysical Fluid Dynamics Laboratory (GFDL) [*Mahlman and Moxim, 1978; Levy et al., 1982; Levy et al., 1985; Levy and Moxim, 1989; Moxim, 1990*]. In recent years, the GCTM has been applied to study the cycling of reactive nitrogen compounds and ozone in the troposphere, in a joint effort between GFDL and the Georgia Institute of Technology (*Kasibhatla et al., 1991; Levy et al., 1991; Kasibhatla, 1993; Kasibhatla et al., 1993; Levy et al., 1993; Galloway et al., 1994; Kasibhatla et al., 1996; Levy et al., 1996; Moxim et al., 1996*). The model has a horizontal resolution of ~265 km, and 11 sigma levels in the vertical at standard pressures of 10, 38, 65, 110, 190, 315, 500, 685, 835, 940, and 990 mb. The model is driven using 12 months of 6-hour time-averaged meteorological fields from a GFDL general circulation model (*Manabe et al., 1974; Manabe and Holloway, 1975*).

In the current application, the GCTM is used to simulate the emissions, transport, transformation, and removal of two species: sulfur dioxide (SO_2) and aerosol sulfate (SO_4). The algorithms used to simulate each of these processes is discussed below.

2.1 Transport

The calculation of tracer advection in the GCTM is described by *Mahlman and Moxim* (1978). The calculations includes parameterizations for subgrid-scale horizontal transport, as well as vertical mixing by dry and moist convection. Details of these parameterizations can be found in *Levy et al.* (1982), *Levy and Moxim* (1989), and *Kasibhatla et al.* (1993).

2.2 Emissions

Because of our focus on the effects of anthropogenic sulfur, we only include anthropogenic sulfur emissions; specifically the Version 1B.1 global SO_x ($SO_2 + SO_4$) emission inventory compiled by the International Global Atmospheric Chemistry/Global Emissions Inventory Activity (GEIA/IGAC) [*Penner et al., 1994*]. This inventory contains seasonally-varying emissions of SO_x from fossil-fuel combustion and some biomass-burning activities at a horizontal resolution of $1^o x 1^o$ apportioned into 2 vertical levels (below 100 m and above 100 m) [*Voldner et al., 1996*; see also *Benkovitz et al., 1996*]. In our model, emissions occurring below 100 m are assigned to the bottom model level (990 mb), while emissions occurring above 100 m are assigned to the 940 mb model level. Direct emissions of SO_4 are known to comprise a small fraction of this SO_x source. Estimates of this fraction generally range from 1.4% in the United States *(Benkovitz et al., 1994)* to 5% in Europe *(Eliassen, 1978)*. Since reliable estimates of this quantity are not available, we simply assume that 2% of the total SO_x source is emitted in the form of SO_4, with the rest being emitted as SO_2.

2.3 Gas-Phase SO$_2$ Oxidation

Our chemical mechanism includes a pathway for converting SO$_2$ to SO$_4$ via gas-phase oxidation initiated by the reaction of SO$_2$ with OH. The rate of this process is calculated at each time-step in the GCTM using prescribed monthly-mean three-dimensional OH fields from *Spivakovsky et al.* (1990) and a reaction rate constant obtained from *DeMore et al.* (1994). Calculations with enhanced OH concentrations will also be presented to illustrate the sensitivity of our results to this prescribed OH distribution.

2.4 Cloud Parameterization

The treatment of aqueous-phase oxidation of SO$_2$ and precipitation scavenging of SO$_2$ and SO$_4$ requires specification of the cloudiness within each grid box of the model at each time step. Since the parent GCM does not explicitly represent clouds, the precipitation scavenging parameterization for GCTMs developed by *Kasibhatla et al.* (1991) was modified to calculate cloudiness in the model. In this modified scheme, a "rainy cloud fraction" and a "non-precipitating cloud fraction" is calculated for each model grid box to represent the fractional volume of air in each model grid-box that undergoes precipitation scavenging and aqueous-phase chemistry, respectively, during each time-step. The "rainy cloud fraction" is calculated using local model-calculated precipitation rates, and assumed cloud liquid water content and cloud height according to Equation 3 in *Kasibhatla et al.* (1991). The "non-precipitating cloudy fraction" is then calculated as:

non-precipitating cloud fraction = max[(9*rainy cloud fraction), (1-rainy cloud fraction)],

based on the assumption that roughly 10% of all clouds precipitate (*Lelieveld, 1990*), and the

constraint that:

non-precipitating cloud fraction + rainy cloud fraction < 1

As described in more detail below, we assume that precipitation scavenging via rainout occurs in the "rainy cloud fraction" of each grid box. Precipitation scavenging via washout, on the other hand, is assumed to occur in the fractions of the grid boxes that lie below the "cloud base" of each of the "rainy cloud fractions", with the "cloud base" assumed to be located at the top of the 940 mb model level (approximately 900 m). In-cloud aqueous-phase chemical processes, are assumed to occur in the "non-precipitating cloud fraction" of each grid box.

2.5 In-Cloud Aqueous-Phase SO_2 Oxidation

In addition to gas-phase oxidation, aerosol SO_4 may be generated in our mechanism via the aqueous-phase oxidation of SO_2 within the 'non-precipitating cloud fraction" of each grid box of the GCTM. A simplified scheme is adopted to account for the effect of oxidant-limitation on this rate. During each chemical time-step (approximately 56 minutes), we assume that there is a rapid conversion of SO_2 to SO_4 in the "non-precipitating cloudy fraction" of a model grid-box, with the amount of SO_2 converted being limited by the gas-phase H_2O_2 concentration within that grid box (*Chameides, 1984*). (In other words, if the H_2O_2 concentration within a grid box is greater than the SO_2 concentration, we assume that all the SO_2 within the "non-precipitating cloudy fraction" of that grid box is converted to SO_4. However, when the H_2O_2 concentration is less than that of SO_2, the amount of SO_2 converted to SO_4 within the "non-precipitating cloudy fraction" is set equal to the amount of H_2O_2 within that fraction). The gas-phase H_2O_2 concentration within each grid box is specified using three-dimensional, monthly-mean fields

from the NCAR CCM2 model (*Stacy Walters, private communication*). This simplified aqueous-phase chemistry scheme neglects the contribution of other potentially important aqueous-phase SO_2 oxidation pathways such as reaction with $(OH)_{aq}$ and $(O3)_{aq}$, as well as by reactions with dissolved NO_3 and NO_2 which may be important in regions of high anthropogenic nitrogen oxide emissions (*Chameides, 1984*). On the other hand, since we assume that the gas-phase H_2O_2 concentration in the "non-precipitating cloudy fraction" of a model grid-box relaxes back to its monthly-mean value within 1 hour, there is the potential to underestimate the H_2O_2 limitation, and therefore overestimate the rate of aqueous-phase SO_2 oxidation. Calculations illustrating the sensitivity of our model to the imposition of oxidant-limitation will be presented later.

2.6 Precipitation Scavenging

The GCTM includes a parameterization for precipitation scavenging of both SO_2 and SO_4 via rainout as well as washout of SO_2. As noted earlier, rainout of SO_2 and SO_4 is assumed to occur in the "rainy cloud fraction" of each model grid box. Following the scheme of Kasibhatla et al. (1991), we assume that all the liquid water within the "rainy cloud fraction" is removed from the atmosphere during each time step and that SO_4 is infinitely soluble, thus effectively assuming a precipitation scavenging efficiency for SO_4 within the "rainy cloud fraction" of unity. As in the case of aqueous-phase oxidation, the amount of SO_2 scavenged within the "rainy cloud fraction" during each time-step is assumed to be limited by the amount of H_2O_2. Thus, when the H_2O_2 concentration is greater than the SO_2 concentration, we adopt an effective precipitation scavenging efficiency for SO_2 within the rainy-cloud fraction of unity. When the H_2O_2 concentration is less than the SO_2 concentration, a proportionally decreasing precipitation

9

scavenging efficiency is adopted. Sensitivity calculations with maximum precipitation scavenging

efficiencies of 0.5 instead of 1 are also presented later.

Washout of SO_2 is assumed to occur in the fractions of each grid box that lie below the

"cloud base" (i.e., at the 940 and 900 mb model levels) of the "rainy cloud fractions". Washout of

aerosol SO_4 (which is assumed to be in the form of sub-micron particles) is neglected (*Langner*

and Rodhe, 1991). Similar to SO_2 rainout in the "rainy cloud fraction" of each model grid box,

washout of SO_2 is assumed to be limited by the amount of H_2O_2.

2.7 Dry Deposition

Surface dry deposition rates of SO_2 and SO_4 are calculated using a drag-coefficient

formulation (*Levy and Moxim, 1989*), which is consistent with the treatment of surface exchange

processes in the parent GCM. Monthly- and spatially-varying dry deposition velocities of SO_2

over land are calculated using a standard resistance-in-series model (*Wesely and Hicks, 1977;*

Wesely, 1989), in conjunction with a $1°\times1°$ map of land-use data (*Mathews, 1983*). The SO_2 dry

deposition velocity over water is assumed to be 0.8 cm/s, and a dry deposition velocity of 0.2 cm/

s is prescribed for SO_4 over all surfaces (*Ryaboshapko, 1983*).

3. BRIEF DESCRIPTION OF MEASUREMENTS USED FOR MODEL EVALUATION

Because of our focus on the anthropogenic fossil-fuel component of the global SO_x

budget, the most appropriate comparison is with measurements from regions where the local SO_x

budget is dominated by this source. Furthermore, since the GCTM used in this study is driven by

meteorology from a GCM, it is desirable that the measurements be of sufficiently long duration,

to permit a climatological evaluation of model performance. With these issues in mind, we have identified two long-term SO_x measurement datasets which are suitable for model evaluation. These datasets are briefly described below.

One dataset is comprised of surface measurements collected as part of the Eulerian Model Field Evaluation Study (EMEFS) over North America from July 1988 to May 1990 (*McNaughton and Vet, 1996*). Part of this dataset, comprised of near-daily measurements of SO_2 and SO_4 air concentrations from 122 air monitoring sites, and rainwater sulfate concentration and precipitation data from 129 deposition monitoring sites, has been provided to us by S. K. Seilkop (*private communication*). The second dataset is comprised of measurements of surface air concentrations of SO_2 and SO_4, rainwater sulfate concentrations, and precipitation data from Europe. These measurements were collected as part of the Co-operative Program for Monitoring and Evaluation of the Long Range Transmission of Air Pollutants in Europe (EMEP) [*Schaug et al, 1987*]. A subset of this dataset covering the period 1983-1992 at 61 sites located in Austria, The Czech Republic, Denmark, Finland, Germany, Great Britain, Italy, Norway, The Netherlands, Poland, Slovakia, and Sweden, was made available by J. Schaug (*private communication*). Since some of these sites are located at significant altitude which may artificially bias our model analysis due to orographical effects, we chose to only use data from sites located below ~ 500 m above m.s.l., and this reduced the number of EMEP sites considered in our analysis to 49.

The site-specific and near-daily EMEFS and EMEP observations were processed by first binning all the measurements into the model grid boxes, and then calculating monthly-mean air concentrations of SO_2 and SO_4, and wet deposition fluxes in each model grid-box where data is available. We then selected those grid boxes for which both summer and winter-mean SO_2 and SO_4 concentrations, as well as wet deposition fluxes, could be derived. This procedure yielded

seasonally-averaged data (at model grid resolution) for 42 grid boxes in North America and for 30 grid boxes in Europe, spanning the range from polluted to background continental sites (see Figures 1 and 2).

Figures 1 and 2 show the processed concentration and wet deposition data for summer and winter from North America and Europe, respectively. It can be seen that mean SO_2 concentrations generally range from 3 to 12 ppbv during winter, and from 1.5 to 6 pbbv during summer, in the highly industrialized regions of eastern North America and western and central Europe. At the cleaner continental sites, SO_2 concentrations generally range 0.5 to 3 ppbv during winter, and from 0.1-1.5 ppbv during summer. (In the rest of this paper, we will use the phrase "large source regions" to refer to regions where the mean surface SO_2 concentration is at least 1.5 ppbv during both summer and winter). There is also a seasonal variation in the wet deposition fluxes at most of the EMEFS and EMEP sites, with the highest fluxes (> 10 mMole S/m^2) occurring in the large source regions during summer.

An especially noteworthy feature of the data illustrated in Figure 1 and 2 is the different seasonal variations in surface SO_4 over North American and Europe. In the large source region of eastern North America between 35N and 50N, a strong seasonal cycle in surface SO_4 is evident, with mean summertime concentrations ranging from 2-4 ppbv, and wintertime concentrations generally falling below 1 ppbv. This is in sharp contrast to the observations in the large source regions of western and central Europe, where no seasonal cycle in surface SO_4 concentrations is evident.

One possible explanation for these different seasonal cycles is the different seasonal patterns in emissions between North American and Europe. Over Europe, SO_x emissions are significantly higher in winter that in summer (*Voldner et al.*, 1966), while over the eastern United

States SO_x emissions are fairly constant throughout the year. Since conversion of SO_2 to SO_4 is driven at least in part by photochemical processes, it is possible that the lack of a seasonal cycle over Europe is the result of the off-setting effects of photochemistry and emissions. However, it is not obvious if this explanation is consistent with the fact the summer-to-winter variation in wet deposition fluxes over the industrialized regions of North America are quite similar to those observed over Europe.

Thus, we see that the EMEFS and EMEP datasets provide a complex picture of regional, seasonal, and species-specific variability in SO_x. In the next sections, we examine the extent to which our model is able to reproduce these contrasting seasonal and regional signals.

4. EVALUATION OF MODEL RESULTS

The model described in Section 2 (which will be referred to as the BASE model) was initialized with a globally-uniform mixing ratio of 1 pptv for both SO_2 and SO_4, and integrated for a period of 16 months after an initial spin-up period of 2 months. In the following sections, we focus on the winter to summer variation in the simulated SO_x surface concentrations and wet deposition fluxes.

We begin our discussion by focussing on a detailed comparison of model results with the EMEFS and EMEP measurements in North America and Europe, respectively. In each region, the observed patterns of SO_2 and SO_4 mixing ratios and wet deposition fluxes are influenced by the distribution of SO_x emissions, as well as by transport processes, gas and aqueous-phase chemical processing of SO_2, dry deposition of SO_2 and SO_4, and precipitation scavenging of SO_2 and SO_4. Given the complex nature of the interaction between each of these processes, it is generally difficult to unambiguously evaluate the model's treatment of the individual processes that

influence the SO_4 budget through comparisons with ambient SO_4 data alone. However, comparisons with the combination of SO_2 and SO_4 mixing ratios and sulfate wet deposition fluxes contained in the EMEFS and EMEP datasets enable us to identify and improve specific shortcomings in the model, and provide a much more rigorous test of the overall performance of the model.

4.1 Comparisons with Surface EMEFS Measurements

Figures 3 and 4 show comparisons of simulated SO_x mixing ratios and wet deposition fluxes with the EMEFS measurements over North America during winter (December-January-February mean) and summer (June-July-August mean), respectively. In each figure, scatter plots of modeled versus measured variables are included on the left hand side, and maps showing the spatial distribution of the ratio of modeled to measured variables are included on the right hand side. Together these two types of plots provide an integrated view of model performance. The degree to which there is a positive correlation between a measured and modeled variable in the scatter plots is indicative of the model's ability to reproduce the spatial distribution of that variable, with deviations from the 1:1 line representing model bias. The location and magnitude of the model biases can then be inferred from the ratio maps.

Inspection of Figures 3 and 4 shows that the modeled SO_2 concentrations correlate well with the measurements, indicating that the model generally captures the large-scale spatial distribution of SO_2 in the EMEFS measurement region. However, the model systematically overestimates the SO_2 concentrations in both seasons, with ratios of calculated-to-measured SO_2 often above 1.5 and occasionally in excess of 2.5. In contrast to SO_2, the model systematically underestimates SO_4 mixing ratios in both seasons by a similar magnitude, and this bias is most

severe at the cleaner background sites during winter.

The scatter plots in Figures 3 and 4 show that the wet deposition fluxes at most of the EMEFS locations are simulated to within a factor of 2, though there are isolated locations with larger discrepancies. Since the wet deposition flux at any given location depends on the local precipitation climatology (which may not be adequately captured in the model), these larger discrepancies do not necessarily suggest a systematic shortcoming in the model's treatment of precipitation scavenging. A closer inspection of the spatial maps does reveal however that there is a tendency in the model to underestimate the wet deposition fluxes in the southwestern part of the EMEFS region, and overestimate the fluxes in the northeastern part of the domain.

4.2 Comparisons with Surface EMEP Measurements

Figures 5 and 6 show comparisons of SO_x mixing ratios and wet deposition fluxes over Europe, in a manner similar to those shown in the previous section. These comparisons show some similarities with those for North America, and also some important differences. Focussing first on the wintertime results, we find that the modeled SO_2 over Europe is again generally higher than the measurements, while SO_4 concentrations are significantly underestimated over the whole region. Unlike in North America, however, where SO_4 concentrations near the large source regions are simulated to within a factor of 2, the underprediction of SO_4 mixing ratios in the large source regions of Europe is consistently larger. The comparison of wet deposition fluxes for winter is similar to that for North America, with agreement to within a factor of 2 at most locations and some larger discrepancies at isolated locations.

In summer, the picture is more complex. The spatial maps in Figure 6 show that both SO_2 and SO_4 tend to be overpredicted in the southern part of the EMEP measurement region around

15

50N, and underpredicted in the northern part. However, when averaged over the entire EMEP region, we once again find a tendency to overpredict SO_2 and underpredict SO_4.

These results suggest that the discrepancies obtained for the summer over Europe arise from two different model shortcomings: (i) A shortcoming that is region-wide and causes an overprediction in SO_2 and an underprediction in SO_4; and (ii) A regionally varying problem that causes a SO_x overprediction in the south and an overprediction in the north. With regard to the regionally varying problem, it is interesting to note that a comparison of modeled and observed wet deposition fluxes over Europe in summer show a similar trend to that found for SO_x, with overpredictions in central and western Europe, and underpredictions in Scandinavia. The fact that the trend is the same for the both the primary and secondary pollutants (SO_2 and SO_4, respectively), as well as for the wet deposition fluxes, suggests that the regionally varying problem is related to transport rather than chemistry. Specifically, it is likely that the summertime northward flux of SO_x from the large source regions in western and central Europe may be underestimated in the model. The origin of the region-wide model discrepancy, which is common to all four intercomparisons (North America and Europe; summer and winter), is the subject of the next section.

4.3 Sensitivity of SO_2 Overprediction and SO_4 Underprediction to the Chemical Algorithms

The comparisons of our model results with the EMEFS and EMEP measurements for both summer and winter indicate a number of model deficiencies, but only one that is common to all four cases: namely, a systematic and, for the most part, significant overprediction in surface SO_2 and underprediction in surface SO_4. Interestingly, in spite of these errors, the model simulations produced little or no systematic error in the sulfate wet deposition flux.

In principal, an overprediction in SO_2 and underprediction in SO_4 could be caused by one or both of the following errors: (i) An underestimate in the SO_4-to-SO_2 ratio in the SO_x emissions; or (ii) An underestimate in the rate of conversion of SO_2 to SO_4 in the continental boundary layer. However, an analysis of our model's sensitivity to SO_4 emissions indicates that in our case the first option is not viable. Recall that we assumed in our BASE model that 2% of the total SO_x emissions are emitted as SO_4. Model calculations indicate that we would have to increase this fraction to at least 10% to remove the SO_2 and SO_4 model biases. However, observations indicate that such a large fraction of primary SO_4 emissions is not realistic (*Dietz and Wieser, 1983; Hass et al., 1993*). It therefore appears that the most likely explanation for the systematic errors in the simulated SO_2 and SO_4 concentration fields arise from a deficiency in the model's treatment of the chemistry of SO_2 to SO_4 conversion, either within the atmospheric boundary layer in general and/or within SO_x source plumes as they mix with and disperse into the background atmosphere. In this section we will examine whether a variety of adjustments to model's chemical algorithms can in fact eliminate the systematic errors without degrading the relatively good simulations of the distribution and rate of sulfate wet deposition that were obtained with the BASE model.

Gas-phase oxidation

One simple way to increase the SO_2 oxidation rate is to increase the specified OH concentration. To test the sensitivity of our results to OH, we conducted a calculation in which the OH concentrations were uniformly increased by a factor of 1.5. We refer to this model as the HIGH-OH model. The results from this model (not illustrated here) indicate only modest

improvements in the SO_2 and SO_4 fields in summer, minimal improvements in winter over North America, and no improvement over Europe. Since it is unlikely that the specified OH has a systematic error of more than a factor of 1.5, we conclude that an underestimate in the gas phase SO_2 oxidation rate is not the cause of our systematic model discrepancies. More generally, the results suggest that it is unlikely that an enhancement in a photochemically-driven mechanism can correct the model's systematic errors since these errors appear in both summer and winter, and tend to be most severe in winter.

Oxidant limitation to in-cloud oxidation

A key facet in our treatment of in-cloud oxidation is the assumption of oxidant limitation by H_2O_2. However, in-cloud oxidation of SO_2 may not always be H_2O_2-limited due to the occurrence of other reactions such as metal-catalyzed reaction with O_2 (*e.g., Clarke and Radojevic, 1987; Ibusuki and Takeuchi, 1987*), and it is also possible that the H_2O_2 fields we have specified are too low. To test the sensitivity of our results to the assumption of H_2O_2-limitation and the concentration of H_2O_2, we have carried out a simulation in which we removed all H_2O_2 limitation from the SO_2 aqueous-phase oxidation and precipitation scavenging processes. We refer to this model as the NO-H2O2LIM model. Results illustrated in Figures 7 and 8 for North America and Europe, respectively, show that while the overestimates in SO_2 are substantially corrected by the NO-H2O2LIM model, the underestimates in surface SO_4 concentrations are not. The lack of improvement in SO_4 arises from two factors: (i) Aqueous-phase production of SO_4 only occurs in the model above 940 mb (the assumed "cloud base"), and thus an increase in the in-cloud SO_2 oxidation rate has a minimal impact on boundary layer SO_4; and (ii) The enhanced

removal of surface SO_2 by non-oxidant limited washout leads to less SO_4 production within the boundary layer via gas-phase oxidation. Finally note that the NO-H2O2LIM model produces a systematic and significant overestimate in sulfate wet deposition fluxes over both North America and Europe, especially during winter.

In-cloud oxidation of boundary layer air

Another key facet of our algorithm for aqueous-phase oxidation is the assumption that boundary layer air below the "cloud base" never undergoes any in-cloud aqueous-phase chemical processing. However, it is possible that turbulent and convective mixing effectively causes some cloud-processing of sub-cloud air. We have therefore examined the sensitivity of our results to the possible presence of sub-cloud aqueous-phase chemical processing by performing a simulation which is identical to the BASE model simulation except for the fact that air in the "sub-cloud" model levels (at 940 and 990 mb) is allowed to undergo aqueous-phase SO_x chemistry and precipitation scavenging of SO_4 (in addition to washout of SO_2). We will refer to this model as the BL-AQCHEM model.

The results from this simulation are compared to the EMEFS and EMEP surface measurements in Figures 9 and 10, respectively. Focussing first on SO_2 and SO_4 over North America, Figure 9 shows that there is a significant improvement in the simulated surface SO_4 mixing ratios at the cleaner background EMEFS locations during winter. There is also a slight decrease in the overestimate of SO_2 concentrations in the polluted EMEFS regions during both summer and winter. However, the model now significantly underestimates SO_2 concentrations at the cleaner background EMEFS locations during summer. The overestimate of wet deposition fluxes in the eastern United States is also exacerbated, since SO_4 in the boundary-layer is now

assumed to undergo precipitation scavenging as well.

Similar effects are seen over Europe (Figure 10). There is a significant improvement in the simulated SO_4 concentrations during both summer and winter. However, the highest wintertime SO_4 concentrations are still significantly underestimated. In addition, the overestimation of the highest wet deposition fluxes and the underestimation of the lowest SO_2 concentrations during summer are now significantly magnified.

As a further test of the BL-AQCHEM model approach, an additional simulation was performed with a reduced precipitation scavenging efficiency of 0.5. This, in effect, reduces the "rainy cloud fraction" calculated for each model grid box by half at each time-step, without altering the calculated "non-precipitating cloudy fraction". However, there was no significant improvement in the overall quality of the simulation. This suggests that factors other than the precipitation intensity (e.g, the precipitation frequency) are important in determining the net rate of precipitation scavenging in the model.

Boundary-layer heterogeneous SO_2 oxidation

The previous two sub-sections demonstrate that increasing the effective rate of in-cloud oxidation has some specific limitations, the most significant of which is the deterioration in the simulation of wet deposition fluxes. Moreover, the results from the HIGH-OH model suggest that an enhancement in the photochemically-driven gas-phase oxidation rate of SO_2 does not eliminate model discrepancies in winter. We are therefore left with one alternative explanation for the hypothesized underestimate in the boundary-layer SO_2 to SO_4 conversion rate: namely, the existence of a heretofore neglected, non-photochemical and therefore, most likely, heterogeneous pathway for converting SO_2 to SO_4 in the boundary-layer. To investigate the viability of this

explanation for the BASE model's systematic errors, we have performed a simulation in which an additional pathway for converting SO_2 to SO_4 in the bottom two levels of the model was added to the chemical mechanism. We will refer to this model as the BL-HETCHEM model.

In principal the heterogeneous conversion of SO_2 to SO_4 could occur ubiquitously throughout the boundary layer on atmospheric aerosols or more rapidly within specialized air masses such as SO_x-rich plumes from power plants as they disperse into the background atmosphere. However, it is beyond the scope of this study to attempt to distinguish between these two types of processes and, we simply treat this additional oxidation pathway in the BL-HETCHEM model as a first-order reaction whose rate is proportional to the concentration of SO_2 within each grid box and a spatially constant rate constant. Model simulations were performed using various values for this first-order reaction rate constant, and it was found that relatively good results could be obtained using values of $1 \times 10^{-6} \, s^{-1}$ for winter and $2 \times 10^{-6} \, s^{-1}$ for summer, and these are the values used to obtain the results for the BL-HETCHEM model reported here. Before discussing the results from this model, it is interesting to note that a rate constant of the magnitude used here is not unreasonable for a heterogeneous reaction involving of SO_2 and particulate matter in the continental boundary layer. In the first place, there is some evidence to suggest that there can be significant conversion of SO_2 to SO_4 in the boundary-layer via heterogeneous reactions on wet and deliquescent aerosols, and in fog droplets (*e.g., Chang et al., 1981; Hoffman and Jacob, 1984; Ruprecht and Sigg, 1990; Chameides and Stelson, 1992*). Furthermore, for typical continental boundary-layer aerosol surface areas of 100-200 $\mu m^2/cm^3$ and mean radii of 0.01 to 0.1 μm, an effective uptake coefficient of only 10^{-5} to 10^{-4} is needed to yield a first-order rate of $1\text{-}2 \times 10^{-6} \, s^{-1}$.

Figures 11 and 12 compare modeled SO_x concentrations and wet deposition fluxes from the BL-HETCHEM model with the EMEFS and EMEP observations, respectively. The improvement in the model results is most pronounced in wintertime, when for both the EMEFS and EMEP regions, the systematic underestimates of surface SO_4 concentrations are largely eliminated and the SO_2 overestimates are decreased, while the simulated wet deposition fluxes remain essentially unchanged. As expected, the additional heterogeneous oxidation pathway has a smaller effect in summer, when the photochemically driven gas- and aqueous-phase conversion processes are relatively fast, but still produces significant improvements in the model simulation. Despite the significant overall improvements, some details in the observations are not captured by the BL-HETCHEM model. For example, during winter, the model does not reproduce the relatively weak SO_4 gradient between the polluted and clean sites in the EMEFS region, and overestimates the surface SO_4 at the relatively clean Scandinavian sites in Europe.

Statistical summary of sensitivity calculations

The overall and relative performances of each of the models described above can be objectively assessed by evaluating the individual model biases for each parameter (SO_2 and SO_4 mixing ratios and sulfate wet deposition flux) for each season. One measure of the overall model bias is the average fractional difference defined as:

$$f_r = \frac{(V_{model} + V_{obs})}{(V_{model} - V_{obs})},$$

where, V_{model} and V_{obs} represent the modeled and measured value of a particular parameter (e.g, the SO_2 concentration), respectively. Another perspective on model performance can be obtained

by evaluating the percentage of comparison points where all three model-calculated parameters (i.e., SO_2 and SO_4 mixing ratios and sulfate wet deposition flux) are within a factor of 2 of the corresponding measurements. We will refer to this percentage as P_2.

Tables 1 and 2 show calculated values of f_r and P_2 during summer and winter for the EMEFS and EMEP regions, respectively, for the various models considered in this study. It is readily evident that the BASE model has a strong negative bias in surface SO_4 over North America and Europe, especially during winter, with f_r = -0.36 and -0.56, respectively. Furthermore, P_2 is less than 50% for all cases except North America during summer. Moreover, inspection of the tables reveals significant problems in the HIGH-OH, NO-H2O2LIM, and BL-AQCHEM models. In the case of the HIGH-OH and the NO-H2O2LIM models, we find that SO_4 biases in winter are still quite large. In addition, a large positive wet deposition flux bias is produced in the NO-H2O2LIM model in winter. The SO_4 bias over North America during winter is relatively small in the BL-AQCHEM model (f_r = -0.04), but remains high over Europe during winter (f_r = -0.34). In addition, the biases in the wet deposition fluxes in the BL-AQCHEM model are at least a factor of 3 larger than the biases in the BASE model over both North America and Europe during winter.

The BL-HETCHEM model clearly produces the best overall simulation. It is the only one which reduces the absolute magnitude of both SO_2 and SO_4 biases in all cases, without significantly increasing the magnitude of the wet deposition flux biases. Furthermore, it is the only one in which the average absolute bias is of the order of 0.2 or less for all three parameters, and yields the largest values for P_2 in both North America and Europe for both seasons. These results, while by no means conclusive, would appear to suggest that an additional heterogeneous

oxidation pathway for SO_2 exists in the continental boundary layer and that this pathway is having

a significant impact on the aerosol sulfate concentrations over North America and Europe.

5. SEASONAL VARIATIONS IN THE ANTHROPOGENIC SULFATE BURDEN

As noted in the Introduction, it is important to characterize the seasonal variation in the

distribution of anthropogenic sulfate aerosols in order to reliably estimate their radiative effect. In

this section, we further examine our ability to correctly predict the summer-to-winter variation in

surface SO_x concentrations and wet deposition fluxes over North America and Europe, where the

radiative effect of anthropogenic sulfate aerosols is expected to be largest. We also use the model

to provide a picture of the large-scale column burden of anthropogenic sulfate, and to quantify the

individual contributions of various processes to the seasonality in the column burden in the large

source regions of North America, Europe, and Asia.

5.1 Seasonal Differences in Surface SO_4 between North America and Europe

As noted in section 3, the most striking difference between the EMEFS measurements

over North America and the EMEP measurements over Europe is in the seasonal cycle of surface

SO_4 concentrations. This is further illustrated in Figure 13 which shows the ratio of the mean

summertime to wintertime SO_4 concentrations measured over North America and Europe. Over

North America, there is a clear seasonality in surface SO_4 mixing ratios, with the summertime

values being about 2-4 times higher than wintertime values at most locations. However, over

Europe the observed summer to winter SO_4 ratio is less than or close to unity at most locations.

Figure 13 also shows the corresponding calculated summer to winter amplitudes from the

BASE and BL-HETCHEM models. Over North America, the BASE model reproduces the ratio

of summer to winter surface SO_4 concentrations quite well at most locations south of ~50N. However, this result is largely fortuitous since the BASE model significantly underestimates surface SO_4 in each season. The BL-HETCHEM model, on the other hand, which is significantly superior to the BASE model in terms of its SO_4 simulation in each season, systematically underestimates the seasonal variation in surface SO_4 south of 50N. This underestimate in the BL-HETCHEM model is caused by the model's tendency to overestimate wintertime SO_4 and underestimate summertime SO_4 in this region (see Figure 11). While both biases by themselves are relatively small, together they cause an average bias in the seasonal amplitude of about a factor of 2.

Comparison with the data from the EMEP region indicates reasonably good agreement between observed model-calculated seasonal amplitude in SO_4 over the relatively clean sites in northern Europe and Scandinavia for both the BASE and BL-HETCHEM Models. However, over the more polluted source regions western and central Europe, the seasonal amplitude in surface SO_4 in the BASE model is 4-6 times higher than the observed seasonal amplitude. The BL-HETCHEM model reduces this bias by about a factor of 2, though the calculated summer-to-winter variation is still too large. This may be at least partly be due to an underestimate of the summertime northward flux of SO_x in this region (see discussion in Section 4.2). Although not illustrated here, we also find that both models tend to capture the seasonal amplitude of the wet deposition flux over the large source regions of North America reasonably well, but overestimate it over corresponding regions in Europe by a factor of 1.5-2.

Thus, neither the BASE nor the BL-HETCHEM model is able to simulate the observed difference between the large source regions of North America and Europe relative to the seasonal

cycle of surface SO_4. While not explicitly stated, a similar discrepancy has been noted in other model studies as well. *Feichter et al.* (1996) found that there was a pronounced underestimate of surface sulfate over central Europe in the ECHAM global model (with a horizontal resolution of $5.625°$), when H_2O_2 oxidant-limitation was considered. *Pham et al.* (1995) found that the IMAGES global model (with a horizontal resolution of $5°$) underpredicted surface SO_4 at most EMEP sites during winter, while overpredicting the measurements during summer. *Hass et al.* (1993) modeled a 3 week episode during February/March 1982 using the EURAD regional model (with a horizontal resolution of 63.5 km). Again, their model systematically underestimated surface SO_4 concentrations in the EMEP region.

Our current inability to accurately model the seasonal variations in surface SO_4 over both North America and Europe, simultaneously, points to a gap in our understanding of the anthropogenic sulfur cycle in precisely those regions where the radiative forcing of sulfate aerosols is calculated to be largest. In this context, further studies, preferably with higher-resolution regional models, are needed to bridge the gap between observations and results from current generation GCTMs.

5.2 Seasonal Variations in the Simulated Large-Scale Column SO_4 Distribution

Our study has focussed thus far on a detailed evaluation of simulated surface mixing ratio and wet deposition fields. In this section, we discuss the seasonal behavior of the simulated large-scale column sulfate distribution. Since the BL-HETCHEM model gives the best overall performance of the various models considered in this study, we restrict our analysis to results from this model.

Figure 14 shows the calculated June-July-August and December-January-February mean

tropospheric column sulfate loadings from the BL-HETCHEM model. As expected, the peak loadings are found to occur in the anthropogenic source regions of eastern North America, western and central Europe, and eastern Asia (i.e., the world's three Continental-Scale Metro-Agro-Plexes; see *Chameides et al., 1994*). The summertime maxima range from 20 to 30 mg SO_4/m^2, with corresponding wintertime maxima lower by factors of 2 to 3 in the NH mid-latitudes. In terms of the absolute differences, the calculated summertime loadings in the NH mid-latitude source regions are therefore 10-20 mg SO_4/m^2 larger than corresponding wintertime loadings. Away from the source regions, the anthropogenic sulfate loading decreases rapidly owing to the relatively short lifetime of both SO_4 and its precursor, SO_2. In fact, owing to faster transport and a longer photochemical lifetime for SO_2 in winter relative to summer, the calculated anthropogenic sulfate loadings over the NH mid-latitude oceans are comparable in the two seasons. Other transport related differences can also be noted. For example, an elongated tongue of elevated column sulfate extends from the source regions of Europe in a west-northwest direction during winter, but not during summer.

Preliminary comparisons of the calculated seasonal column SO_4 burdens with results from other models show some similarities, but also some noteworthy differences. The column burdens over North America and Europe from the BL-HETCHEM model are similar to those calculated by *Feichter et al.* (1996) using the ECHAM model, in both summer and winter. Over Asia, the SO_4 burden in the BL-HETCHEM model is 1.5-2 times smaller than in the ECHAM model. Over all three source regions, the BL-HETCHEM and ECHAM models produce column SO_4 burdens that are 2-3 times larger than those calculated by *Taylor and Penner* (1994) during winter. These differences reflect the range of uncertainty that is prevalent in the current generation of global

models for SO_4. The degree to which such differences in the calculated SO_4 burden cause differences in the estimated magnitude of regional radiative forcings remains to be assessed.

5.3 Seasonal Variations in Regional Column SO_4 Budgets

Given the relatively large magnitude of the SO_4 column loadings in the NH source regions, it is interesting to examine the factors responsible for the seasonal variability of column sulfate in these region. Figure 15 shows the seasonal variation of the integrated column burden of SO_4 simulated in each of 3 continental regions (only model land boxes are considered): eastern North America, between 25N-50N and 60W-100W; western and central Europe, between 40N-60N and 10W-40E; and, eastern Asia, between 15N-45N, and 105E-140E. Also shown in Figure 15, are the model-calculated, areally-integrated wet and dry deposition fluxes, chemical production rates, and direct emissions of SO_4 in each region over the course of a season, as well as the diagnosed net transport flux out of each region during that season. In the rest of this discussion, we will use the terms North America, Europe, and eastern Asia, only to refer to these specific sub-regions.

Over North America and Europe, model-calculated SO_4 burdens are similar in magnitude during the summer (~15 mg SO_4/m^2). However, the wintertime column SO_4 burden over Europe (9.3 mg SO_4/m^2) is almost a factor of 2 larger than that over North America (5.3 mg SO_4/m^2). Thus, the model-calculated seasonal amplitude in column SO_4 is larger over North America than over Europe. In terms of the vertical distribution (not shown here), the amount of SO_4 in the bottom 1 km is approximately equal to the amount above 1 km, with the balance shifting slightly between seasons. In winter, a larger fraction tends to occur in the boundary layer, while in

summer there is a larger contribution from the free troposphere.

It is also evident from Figure 15 that the major source of SO_4 in each of these regions is aqueous-phase chemical production, with smaller, but nevertheless significant contributions from the hypothesized boundary-layer heterogeneous conversion pathway as well as summertime gas-phase photochemistry. It can be seen that there is significantly more production of SO_4 by aqueous-phase and boundary-layer heterogeneous chemistry in winter over Europe than over North America. This difference is due to the fact that there is a significant seasonal cycle in SO_x emissions over Europe, but not over North America. Regional SO_x emissions range from 5-6 mg $S/m^2/day$ over Europe in summer, and over North America in summer and winter, while wintertime SO_x emissions over Europe are about a factor of 1.7 larger. It is this difference in the seasonality of SO_x emissions between North America and Europe that results in the lower seasonal amplitude in column SO_4 over Europe relative to that over North America.

Over eastern Asia, summertime and wintertime column SO_4 burdens are comparable and are of the order of 10 mg SO_4/m^2. This lack of a seasonal difference is due to the fact that wintertime SO_x emissions are about 25% larger than summertime emissions in this region, and also due to the smaller seasonal variation in photochemically-driven processes relative to that in the higher latitude regions of North America and Europe. In all three regions, the production of SO_4 is largely balanced by the wet deposition within the region, and to a lesser extent by export from the region.

It is also interesting to note that the SO_4 production by our hypothesized boundary-layer heterogeneous chemical pathway makes about a 15-40% contribution to the total SO_4 production within each region. If this hypothesized process were to largely occur on coarse particles, which

make a minimal contribution to climate forcing (Boucher and Anderson, 1995), one would have to reduce the calculated column SO_4 burden by this fraction when evaluating the radiative forcing of anthropogenic sulfate aerosols.

6. SUMMARY

We have investigated the seasonal variation in the tropospheric cycle of anthropogenic sulfur using a three-dimensional GCTM. This model is typical of the current generation of GCTMs, the results from which are being used to characterize the radiative forcing of natural and anthropogenic sulfate aerosols. One emphasis of this study has been on a detailed evaluation of model results in regions where the radiative forcing of anthropogenic SO_4 aerosols is believed to be largest. In this context, simultaneous measurements of SO_2 and SO_4 concentrations and wet deposition fluxes from the EMEFS and EMEP measurements provide a rigorous test of model performance.

The comparisons with the EMEFS and EMEP measurements suggest that boundary-layer conversion of SO_2 to SO_4 by a pathway other than gas-phase OH-driven oxidation may be of some significance. We estimate that the pseudo-first order reaction rate coefficient for this process is of the order $1\text{-}2 \times 10^{-6}$ s^{-1}, which is comparable to the corresponding summertime gas-phase SO_2 oxidation rate in NH mid-latitudes. A likely candidate for this process is heterogeneous oxidation of SO_2 on the surfaces of atmospheric aerosols. Given aerosol loadings typical of the continental boundary layer, an effective accommodation coefficient of only 10^{-5} to 10^{-4} would be required to yield a pseudo first-order rate constant of 10^{-6} s^{-1}. If such a process does indeed exist,

it has the potential to alter the size distribution of sulfate aerosols within the continental boundary layer and thus the radiative effects of these aerosols.

When we include this hypothesized heterogeneous conversion pathway in the model, simulated surface SO_2 and SO_4 concentration fields and wet deposition fluxes agree well with observations from the EMEFS and EMEP datasets. At most of the comparison points, the agreement is within a factor of 2. When all three parameters are considered simultaneously, the simulations are within a factor of 2 of the measurements at 55-70% of the comparison points in North America, and at about 45% of the comparison points in Europe. One major discrepancy, however, is the inability to simulate the difference between the industrialized regions of North America and Europe, in terms of the seasonal amplitude of surface SO_4, and it appears that this is a shortcoming common to other GCTMs as well.

The simulated column SO_4 is largest over the industrialized regions of eastern North America, western and central Europe, and eastern Asia, ranging from 5 to 15 mg SO_4/m^2. Over eastern North America, the simulated burden varies from ~6 mg SO_4/m^2 in winter to ~15 mg $SO_4/$ m^2 in summer. This seasonal variation is driven by the seasonal variations in gas- and aqueous-phase chemical production rates of SO_4. Over western and central Europe, the simulated seasonal amplitude in the column SO_4 burden is smaller due to the fact that the seasonal variation in photochemistry is partially compensated for by an opposite seasonal variation in SO_x emissions. In fact since our model overestimates the seasonal amplitude in surface SO_4 over western and central Europe, and underestimates it in eastern North America, it is possible that the difference in the seasonal amplitude in column sulfate over these two regions may be even larger. On the other hand, since the simulated summertime column SO_4 burdens over North American and Europe are

comparable, our model would likely predict similar cooling rates from sulfate aerosols over the two regions.

Our study suggests a number of potentially important areas of uncertainty in our understanding of, and ability to, simulate the cycle of anthropogenic sulfur and its impact on the climate. These uncertainties include the possible role of previously neglected heterogeneous oxidation pathways for SO_2, complex and largely unexplained regional differences in the seasonal cycle of sulfate, and indications of significant regional differences in column sulfate loadings predicted by different GCTMs. In order to increase our confidence in GCTM simulations of atmospheric sulfur species, these uncertainties need to be addressed though more detailed and comprehensive datasets. Long-term measurements of column sulfate loadings over North America, Europe, and eastern Asia would be most valuable in this regard. In addition, the rapid growth in sulfur emissions projected for eastern Asia suggests that a regional measurement program similar to EMEFS and EMEP should be a high priority.

REFERENCES

Benkovitz, C. M., C. M. Berkovitz, R. C. Easter, S. Nemesure, R. Wagener, and S. E. Schwartz, Sulfate over the North Atlantic and adjacent continental regions: Evaluation for October and November 1986 using a three-dimensional model driven by observation-derived meteorology, *J. Geophys. Res.*, *99*, 20725-20756, 1994.

Benkovitz, C. M., M. T. Scholtz, J. Pacyna, L. Tarrason, J. Dignon, E. C. Voldner, P. A. Spiro, J. A. Logan, and T. E. Graedel, Global gridded inventories of anthropogenic emissions of sulfur and nitrogen, *submitted to J. Geophys. Res.*, 1996.

Bolin, B., and R. J. Charlson, On the role of the tropospheric sulfur cycle in the shortwave radiative climate of the earth, *Ambio, 5*, 47-54, 1976.

Boucher, O., and T. L. Anderson, General circulation model assessment of the sensitivity of direct climate forcing by anthropogenic sulfate aerosols to aerosol size and chemistry, *J. Geophys. Res., 100*, 26117-26134, 1995.

Chameides, W. L., The photochemistry of remote marine stratiform cloud, *J. Geophys. Res., 89*, 4739-4755, 1984.

Chameides, W. L., and A. W. Stelson, Aqueous-phase chemical processes in deliquescent sea-salt aerosols: A mechanism that couples the atmospheric cycles of S and sea salt, *J. Geophys. Res., 97*, 20565-20580, 1992.

Chameides, W. L., P. S. Kasibhatla, J. Yienger, and H. Levy II, Growth of continental-scale metro-agro-plexes, regional ozone pollution, and world food production, *Science, 264*, 74-77, 1994.

Clarke, A. G., and M. Radojevic, Oxidation of SO_2 in rainwater and its role in acid rain chemistry, *Atmos. Environ., 21*, 1115-1123, 1987.

Chang, S. G., R. Toosi, and T. Novakov, The importance of soot particles and nitric acid in

oxidizing SO_x in atmospheric aqueous droplets, *Atmos. Environ.*, *15*, 1287-1292, 1981.

Charlson, R. J., J. E. Lovelock, M. O., Andreae, and S. G. Warren, Oceanic phytoplankton, atmospheric sulfur, cloud albedo and climate, *Nature, 326*, 655-661, 1987.

Charlson, R. J., J. Langner, H. Rodhe, C. B. Leovy, and S. G. Warren, Perturbation of the northern hemisphere radiative balance by backscattering from anthropogenic aerosols, *Tellus, 43AB*, 152-163, 1991.

Charlson, R. J., S. E. Schwartz, J. M. Hales, R. D. Cess, J. A. Coakley, Jr., J. E. Hansen, and D. J. Hoffman, Climate forcing by anthropogenic aerosols, *Science, 255*, 423-430, 1992.

Chin, M., D. F. Jacob, G. M. gardner, M. Forman-Fowler, P. A. Spiro, and D. L. Savoie, A global three-dimensional model of tropospheric sulfate, *submitted to J. Geophys. Res.*, 1996.

DeMore, W. B., S. P. Sander, D. M. Golden, R. F. Hampson, M. J. Kurylo, C. J. Howard, A. R. Ravishankara, C. E. Kolb, and M. J. Molina, Chemical Kinetics and Photochemical Data for Use in Stratospheric Modeling, *JPL Publication 94-26*, Pasadena, CA, 1994.

Dietz, R. N., and R. F. Wieser, Sulfate formation in oil-fired power plant plumes. Vol. 1, Parameters affecting primary sulfate emissions and a model for predicting emissions and plume opacity, *Rep. EPRI EA-3231*, Elec. Power. Res. Inst., Palo Alto, CA, 1983.

Eliassen, A., The OECD study of long range transport of air pollutants: Long range transport modeling, *Atmos. Environ., 12*, 479-487, 1978.

Feichter, J., E. Kjellstrom, H. Rodhe, F. Dentener, J. Lelieveld, and G. -J. Roelofs, Simulation of the tropospheric sulfur cycle in a global climate model, *Atmos. Environ, in press*, 1996.

Galloway, J. N., H. Levy II, and P. S. Kasibhatla, Year 2020: Consequences of population growth and development on deposition of oxidized nitrogen, *Ambio, 23*, 120-123, 1994.

Hass, H., A. Ebel, H. Feldmann, H. J. Jakobs, and M. Memmesheimer, Evaluation studies with a

regional chemical transport model (EURAD) using air quality data from the EMEP monitoring network, *Atmos. Environ., 27A*, 867-887, 1993.

Haywood, J. M., and K. P. Shine, The effect of anthropogenic sulfate and soot aerosol on the clear sky planetary radiation budget, *Geophys. Res. Lett., 22*, 603-606, 1995.

Hoffman, M. R., and D. Jacob, Kinetics and mechanisms of the catalytic oxidation of dissolved sulfur dioxide in aqueous solution: An application to nighttime fog chemistry, in SO_2, *NO, and NO_x Oxidation Mechanisms: Atmospheric Considerations*, pp. 101-172, edited by J. G. Calvert, Butterworth, Boston, MA, 1984.

Ibusuki, T., and Takeuchi, K., Sulfur dioxide oxidation by oxygen catalyzed by mixtures of manganese (II) and iron (III) in aqueous solutions at environmental reaction conditions, *Atmos. Environ., 21*, 1555-1560, 1987.

Kasibhatla, P. S., H. Levy II, W. J. Moxim, and W. L. Chameides, The relative impact of stratospheric photochemical production on tropospheric NO_y levels: A model study, *J. Geophys. Res., 96*, 18631-18646, 1991.

Kasibhatla, P. S., H. Levy II, and W. J. Moxim, Global NO_x, HNO_3, PAN, and NO_y distributions from fossil fuel combustion emissions: A model study, *J. Geophys. Res., 98*, 7165-7180, 1993.

Kasibhatla, P. S., NO_y from sub-sonic aircraft emissions: A global three-dimensional model study, *Geophys. Res. Lett.*, 1707-1710, 1993.

Kasibhatla, P., H. Levy II, A. Klonecki, and W. L. Chameides, A three-dimensional view of the large-scale tropospheric ozone distribution over the North Atlantic Ocean during summer, *J. Geophys. Res., in press*, 1996.

Kiehl, J. T., and B. P. Briegleb, The relative roles of sulfate aerosols and greenhouse gases in climate forcing, *Science, 260*, 311-314, 1993.

Langner, J., and H. Rodhe, A global three-dimensional model of the tropospheric sulfur cycle, J. *Atmos. Chem.*, *13*, 225-263, 1991.

Lelieveld, J., The role of clouds in tropospheric photochemistry, Ph.D. thesis, State Univ. Utrecht, The Netherlands, 1990.

Levy II, H., J. D. Mahlman, and W. J. Moxim, Tropospheric N_2O variability, *J. Geophys. Res.*, *87*, 3061-3080, 1982.

Levy II, H., J. D. Mahlman, W. J. Moxim, and S. C. Liu, Tropospheric ozone: The role of transport, *J. Geophys. Res.*, *90*, 3753-3772, 1985.

Levy, II, H., and W. J. Moxim, Simulated global distribution and deposition of reactive nitrogen emitted by fossil fuel combustion, *Tellus*, *41*, 256-271, 1989.

Levy II, H., W. J. Moxim, P. S. Kasibhatla, and J. A. Logan, The global impact of biomass burning on tropospheric reactive nitrogen, in *Global Biomass Burning: Atmospheric, Climatic, and Biospheric Implications*, pp. 363-369, edited by J. S. Levine, The MIT Press, Cambridge, MA, 1991.

Levy II, H., W. J. Moxim, and P. S. Kasibhatla, Impact of global NO_x sources on the northern latitudes, in *NATO ASI Series, Vol. 17: The Tropospheric Chemistry of Ozone in Polar Regions*, pp. 77-88, edited by H. Niki and K. H. Becker, Springer-Verlag, Berlin-Heidelberg, 1993.

Levy II, H., W. J. Moxim, and P. S. Kasibhatla, A global 3-dimensional time-dependent lightning source of tropospheric NO_x, *submitted to J. Geophys. Res.*, 1996.

Mahlman, J. D., and W. J. Moxim, Tracer simulations using a global general circulation model: Results from a midlatitude instantaneous source experiment, *J. Atmos. Sci.*, *35*, 1340-1374, 1978.

Mahlman, J. D., H. Levy II, and W. J. Moxim, Three-dimensional tracer structure and behavior as

simulated in two ozone precursor experiments, *J. Atmos. Sci., 37*, 655-685, 1980.

Manabe S., D. G. Hahn, and J. L. Holloway, Jr., The seasonal variation of the tropical circulation

as simulated by a global model of the atmosphere, *J. Atmos. Sci., 31*, 43-83, 1974.

Manabe S., and J. L. Holloway, Jr., The seasonal variation of the hydrologic cycle as simulated by

a global model of the atmosphere, *J. Geophys. Res., 80*, 1617-1649, 1975.

Mathews, E., Global vegetation and land use: new high-resolution data bases for climate studies,

J. Clim. Appl. Meteorol., 22, 474-487, 1983.

McNaughton, D. J., and R. J. Vet, Eulerian model evaluation field study (EMEFS): A summary of

surface network measurements and data quality, *Atmos. Environ., 30*, 227-238, 1996.

Moxim, W. J., Simulated transport of NO_y to Hawaii during August: A synoptic study, *J.

Geophys. Res., 95*, 5717-5729, 1990.

Moxim, W. J., H. Levy II, and P. S. Kasibhatla, Simulated global tropospheric PAN: Its transport

and impact on NO_x, *J. Geophys. Res., in press*,1996.

National Acid Precipitation Assessment Program (NAPAP), *Acidic Deposition: State of Science

and Technology*, National Acid Precipitation Assessment Program, Washington, D.C., 1990.

Organization for Economic Cooperation and Development (OECD), *The OECD Program on

Long Range Transport of Pollutants, Summ. Rep.*, Org. for Econom. Coop. and Dev., Paris,

1977.

Penner, J. E., C. S. Atherton, and T. A. Graedel, Global emissions and models of photochemically

active compounds, in Global Atmospheric-Biospheric Chemistry, pp. 223-247, edited by R.

G. Prinn, Plenum Press, New York, 1994.

Pham, M., J. -F. Muller, G. P. Brasseur, C. Granier, and G. Megie, A three-dimensional study of

the tropospheric sulfur cycle, *J. Geophys. Res., 100*, 26061-26092, 1995.

Ruprecht, H., and Sigg, L., Interactions of aerosols (ammonium sulfate, ammonium nitrate, and ammonium chloride) and of gases (HCl, HNO$_3$) with fogwater, *Atmos. Environ., 24A*, 573-584, 1990.

Ryaboshapko, A. G., The atmospheric sulfur cycle, in The Global Biogeochemical Sulphur Cycle, pp. 203-296, edited by M. V. Ivanov and J. R. Freney, Scientific Committee on Problems of the Environment (SCOPE), 1983.

Schaug, J., J. E. Hansen, K. Nodop, B. Ottar, and J. M. Pacyna, Summary report from the chemical co-ordinating center for the third phase of EMEP, EMEP/CC-report 3/87, 160 pp., The Norwegian Institute for Air Research, Lillestrom, Norway, 1987.

Shaw, R. W., Jr., and R. J. Paur, Measurements of sulfur in gases and particles during sixteen months in the Ohio river valley, *Atmos. Environ., 17*, 1431-1438, 1983.

Spivakovsky, C. M., R. Yevich. J. A. Logan, S. C. Wofsy, and M. B. McElroy, Tropospheric OH in a three-dimensional chemical tracer model: An assessment based on observations of CH$_3$CCl$_3$, *J. Geophys. Res., 95*, 18441-18471, 1990.

Taylor, K. E., and J. E. Penner, Response of the climate system to atmospheric aerosols and greenhouse gases, *Nature, 369*, 734-737, 1994.

Twomey, S. A., M. Piepgrass, and T. L. Wolfe, An assessment of the impact of pollution on global cloud albedo, *Tellus, 36B, 356-366*, 1984.

Voldner, E. C., M. T. Scholtz, K. A. Davidson, Y. -F. Li, and C. M. Benkovitz, 1 degree x 1 degree global SO$_x$ and NO$_x$ two-level emissions inventories resolved seasonally into emission sectors and point and area sources, *in preparation*, 1996.

Wesely, M. L., Parameterization of surface resistances to gaseous dry deposition in regional-scale

numerical models, *Atmos. Environ.*, *23*, 1293-1304, 1989.

Wesely, M. L., and B. B. Hicks, Some factors that affect the deposition rates of sulfur dioxide and similar gases on vegetation, *J. Air Pollut. Control Assoc.*, *27*, 110-1116, 1977.

TABLE 1

Statistical Summary of Comparison of Model Results with Surface Measurements in
North America

WINTER

Model	$f_r^{(a)}$			$P_2^{(b)}$
	SO_2	SO_4	Wet Dep.	(%)
BASE	0.23	-0.36	0.08	21
HIGH-OH	0.22	-0.27	0.09	31
NO-H2O2LIM	0.04	-0.44	0.53	10
BL-AQCHEM	0.11	-0.04	0.32	40
BL-HETCHEM	0.18	0.08	0.11	55

SUMMER

Model	$f_r^{(a)}$			$P_2^{(b)}$
	SO_2	SO_4	Wet Dep.	(%)
BASE	0.11	-0.26	0.03	52
HIGH-OH	0.08	-0.17	0.04	62
NO-H2O2LIM	0.04	-0.31	0.08	29
BL-AQCHEM	-0.15	-0.12	0.11	50
BL-HETCHEM	0.05	-0.12	0.04	69

(a) f_r is the fractional difference between model results and measurements (see definition in Section 4.3).

(b) P_2 is the percentage of the 42 comparison points where parameters are within a factor of 2 of the measurements.

40

TABLE 2

Statistical Summary of Comparison of Model Results with Surface Measurements in Europe

WINTER

Model	$f_r^{(a)}$			$P_2^{(b)}$
	SO_2	SO_4	Wet Dep.	(%)
BASE	0.20	-0.56	-0.06	0
HIGH-OH	0.20	-0.53	-0.04	0
NO-H2O2LIM	-0.20	-0.63	0.41	3
BL-AQCHEM	0.11	-0.34	0.17	17
BL-HETCHEM	0.13	0.03	-0.01	43

SUMMER

Model	$f_r^{(a)}$			$P_2^{(b)}$
	SO_2	SO_4	Wet Dep.	(%)
BASE	0.02	-0.22	-0.05	40
HIGH-OH	0.04	0.09	-0.02	47
NO-H2O2LIM	-0.13	-0.33	-0.01	23
BL-AQCHEM	-0.35	-0.01	0.04	30
BL-HETCHEM	-0.04	0.03	-0.04	47

(a) f_r is the fractional difference between model results and measurements (see definition in Section 4.3).

(b) P_2 is the percentage of the 30 comparison points where parameters are within a factor of 2 of the measurements.

41

FIGURE CAPTIONS

1. Gridded SO_2 and SO_4 mean concentrations and sulfate wet deposition fluxes during winter (December-January-February) and summer (June-July-August) derived from the EMEFS network in North America. The dashed line represents the boundary of the region (referred to as the "large source region" in the text) within which measured SO_2 concentrations are greater than or equal to 1.5 ppbv in both summer and winter.

2. Gridded SO_2 and SO_4 mean concentrations and sulfate wet deposition fluxes during winter (December-January-February) and summer (June-July-August) derived from the EMEP network in Europe. The dashed line represents the boundary of the region within which measured SO_2 concentrations are greater than or equal to 1.5 ppbv in both summer and winter.

3. Comparisons of simulated mean SO_2 and SO_4 concentrations and wet deposition fluxes from the BASE model with measurements for North America during summer. Left panels show scatter plots of modeled versus measured variables, and right panels show the ratio of the modeled to the measured variable at individual grid box locations. In the scatter plots, the 1:1 line (solid) and the 1:2 and 2:1 lines (dashed) are shown for reference. In the spatial maps, the dashed line represents the boundary of the region within which measured SO_2 concentrations are greater than or equal to 1.5 ppbv in both summer and winter.

4. Same as Figure 3, but for North America during summer.

5. Same as Figure 3, but for Europe during winter.

6. Same as Figure 3, but for Europe during summer.

7. Scatter plots of simulated mean SO_2 and SO_4 concentrations and wet deposition fluxes from the NO-H2O2LIM model (unfilled circles) with wintertime and summertime measurements

for North America. Also shown are comparisons with the BASE model results (filled circles). The 1:1 line (solid) and the 1:2 and 2:1 lines (dashed) are shown for reference.

8. Same as Figure 7, but for Europe.

9. Scatter plots of simulated mean SO_2 and SO_4 concentrations and wet deposition fluxes from the BL-AQCHEM model (unfilled circles) with wintertime and summertime measurements for North America. Also shown are comparisons with the BASE model results (filled circles). The 1:1 line (solid) and the 1:2 and 2:1 lines (dashed) are shown for reference.

10. Same as Figure 9, but for Europe.

11. Scatter plots of simulated mean SO_2 and SO_4 concentrations and wet deposition fluxes from the BL-HETCHEM model (unfilled circles) with wintertime and summertime measurements for North America. Also shown are comparisons with the BASE model results (filled circles). The 1:1 line (solid) and the 1:2 and 2:1 lines (dashed) are shown for reference.

12. Same as Figure 11, but for Europe.

13. Ratio of summertime to wintertime mean surface SO_4 concentrations in North America and Europe. The top panel shows ratios derived from measurements, the middle panel shows ratios derived from the BASE model, and the bottom panel shows results derived from the BL-HETCHEM model. The dashed line represents the boundary of the region within which measured SO_2 concentrations are greater than or equal to 1.5 ppbv in both summer and winter.

14. Simulated mean tropospheric column burden of SO_4 during December-January-February (top panel) and June-July-August (bottom panel) in the BL-HETCHEM model.

15. Seasonal budgets of regional column SO_4 over eastern North America (25N-60N, 60W-100W), western and central Europe (40N-60N, 10W-40E), and eastern Asia (15N-45N, 105E-140E) in the BL-HETCHEM model. The column SO_4 burden is in units of mg SO_4/m^2; other

quantities are in units of mg SO_4/m^2/day. Note that the column SO_4 burden is scaled down by
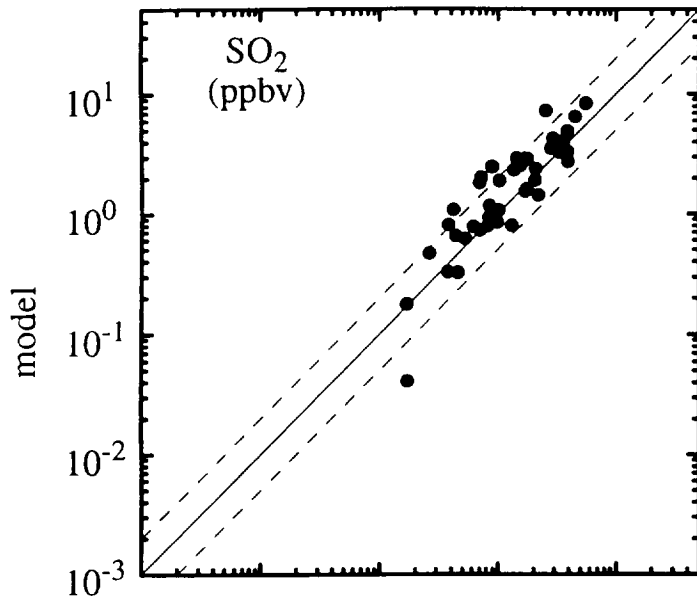
a factor of 2 to facilitate presentation.

(1)

NORTH AMERICA

WINTER   SUMMER
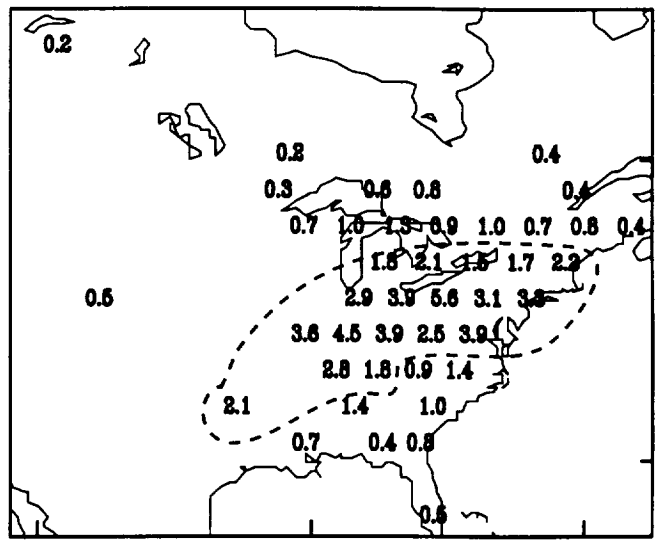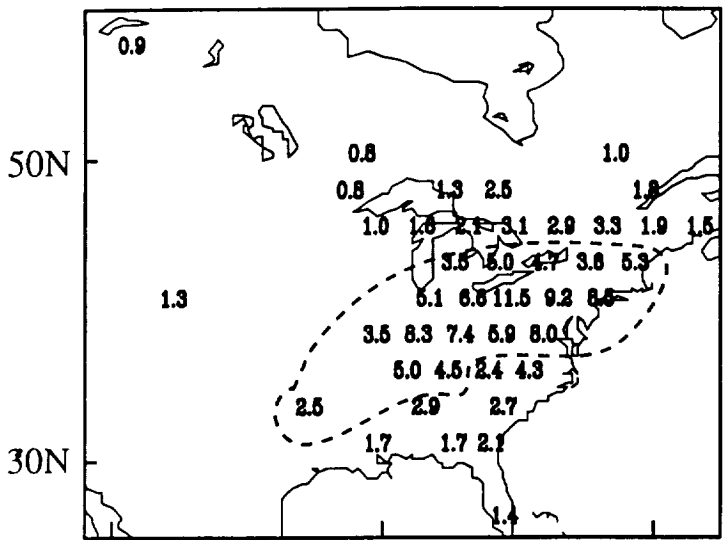
SO₂ (ppbv)
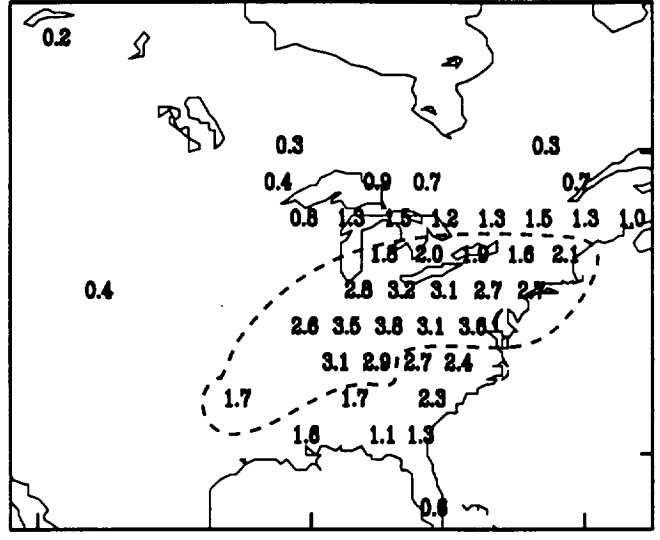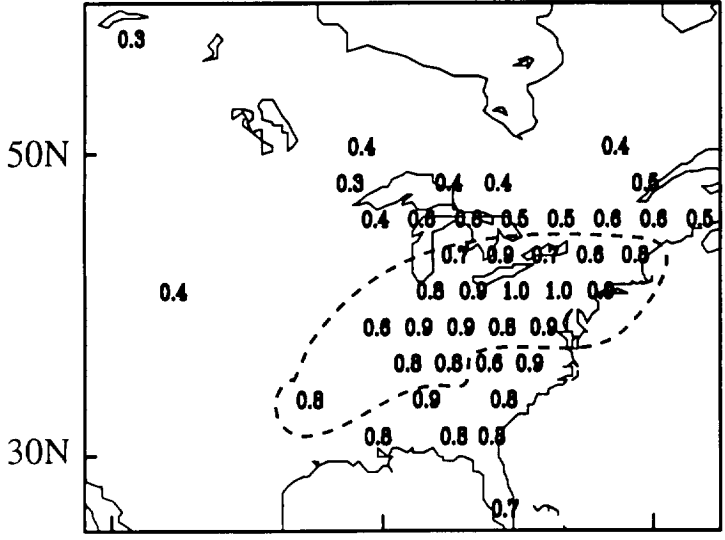
SO₄ (ppbv)
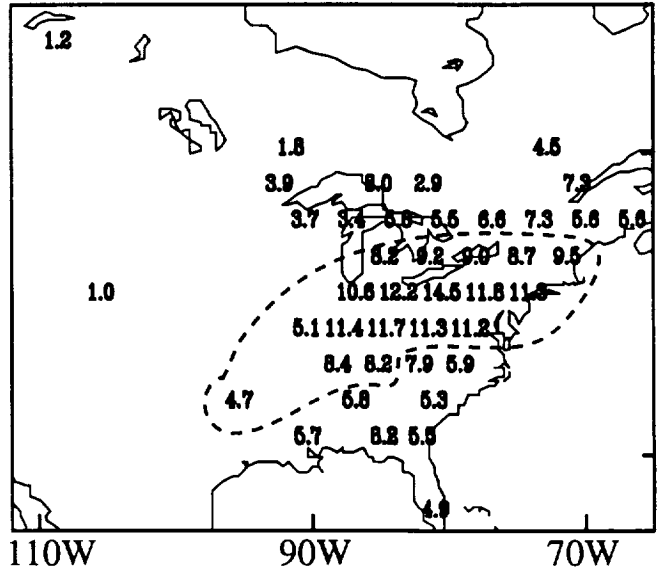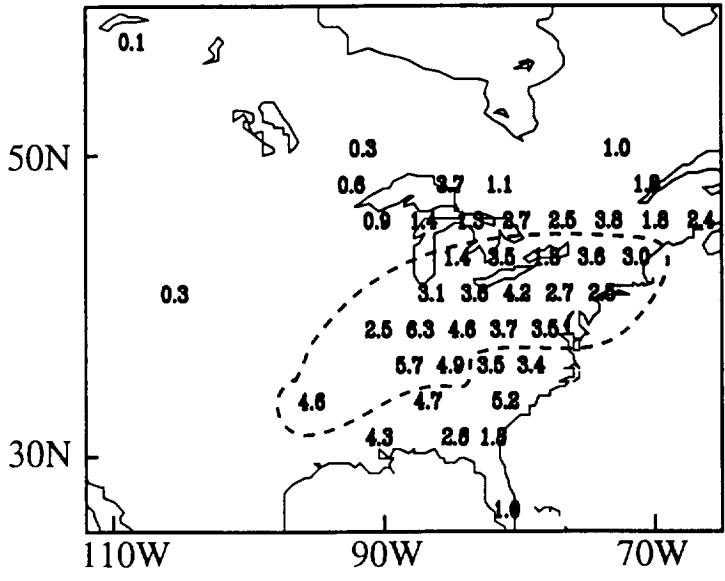
Wet Dep. (mMole S/m²)

110W   90W   70W   110W   90W   70W

EUROPE

WINTER **SUMMER**

SO$_2$ (ppbv)

WINTER (SO$_2$):
70N, 1.4
0.8
0.5 0.9 2.5
0.6 2.8 6.1
1.3 0.6 2.9 2.4 2.7
0.7 1.8 5.6 3.4 4.5
4.8 6.5 10.6
2.2 3.1 2.1 6.3 8.3
50N
10.9
4.1 5.4

SUMMER (SO$_2$):
70N, 0.4
0.1
0.1 0.4 0.6
0.2 1.3 1.4
0.8 0.3 1.0 0.8 0.8
0.8 0.9 2.6 0.6 1.3
2.9 2.5 1.8
1.1 1.3 1.0 2.2 1.9
50N
3.6
0.8 1.4

SO$_4$ (ppbv)

WINTER (SO$_4$):
70N, 0.5
0.3
0.2 0.3 0.7
0.3 0.9 1.4
0.6 0.5 1.0 0.7 0.8
0.6 0.7 1.0 1.1 0.9
1.3 1.6 1.7
0.6 1.4 0.9 1.2 3.5
50N
2.0
2.6 1.9

SUMMER (SO$_4$):
70N, 0.3
0.2
0.3 0.3 0.5
0.4 0.7 0.6
0.8 0.6 0.9 0.6 0.7
0.7 0.8 1.0 0.8 0.9
1.2 1.4 1.1
1.0 1.1 0.9 1.2 2.2
50N
1.1
1.6 1.7

Wet Dep. (mMole S/m^2)

WINTER (Wet Dep.):
70N, 0.2
1.9
1.4 1.2 1.5
1.3 3.8 7.2
3.0 5.4 5.0 3.2 3.7
3.0 6.6 3.6 3.7 6.3
3.8 7.7 4.0
4.6 1.5 2.7 2.6 5.8
50N
2.4
2.0 4.9

SUMMER (Wet Dep.):
70N, 1.7
1.9
2.3 3.5 4.1
3.8 4.6 6.6
3.9 6.6 6.9 5.7 5.2
3.6 6.5 7.0 6.0 6.7
6.6 8.4 7.6
3.6 4.1 2.6 6.6 10.3
50N
7.3
5.2 15.5

GM 20E GM 20E

NORTH AMERICA: WINTER
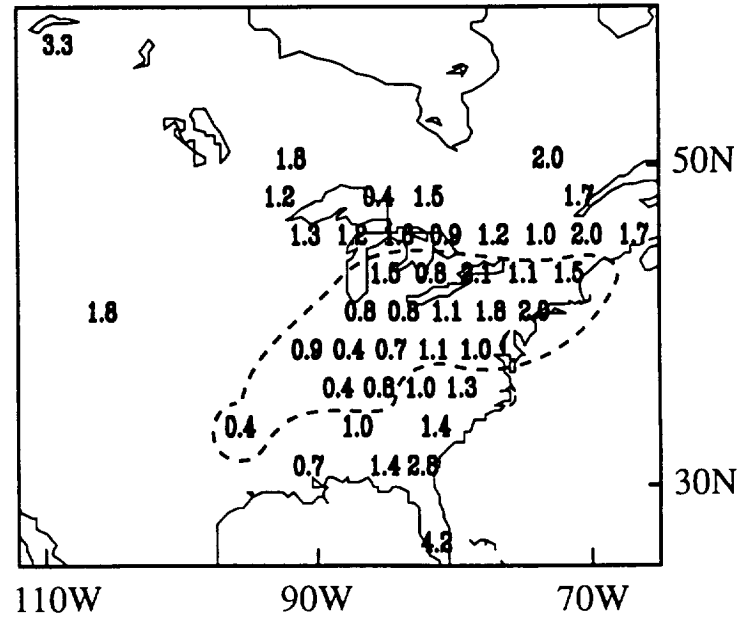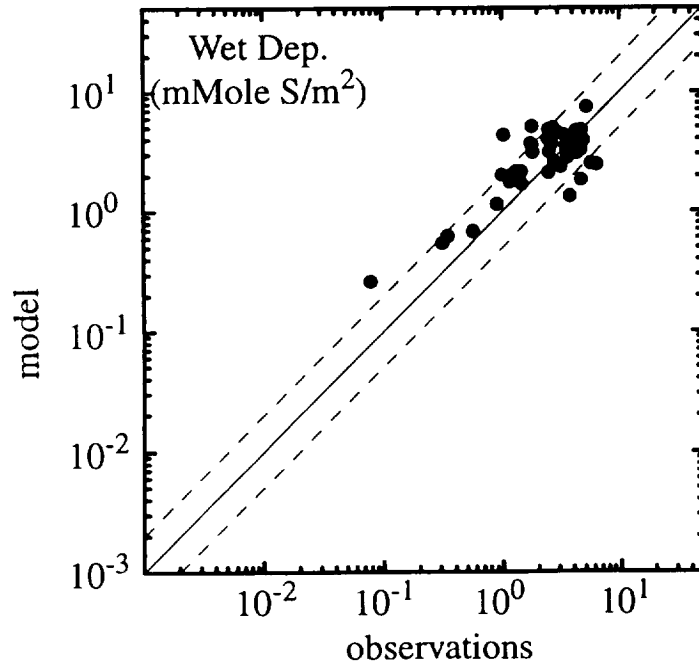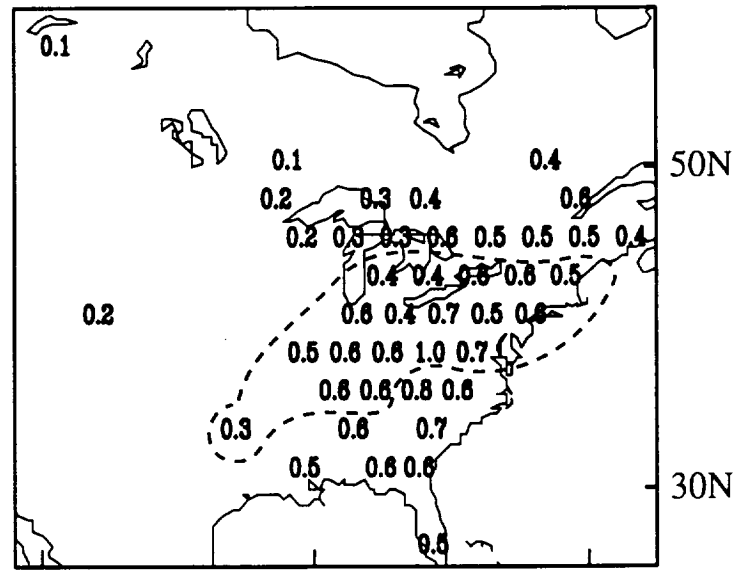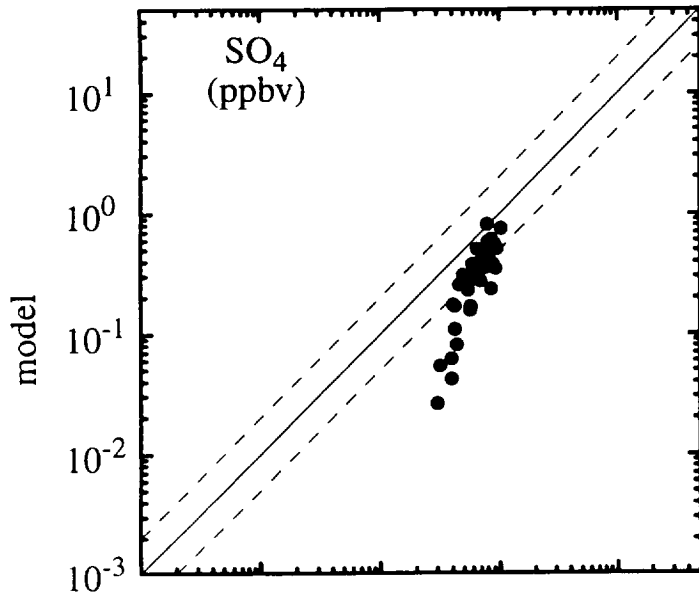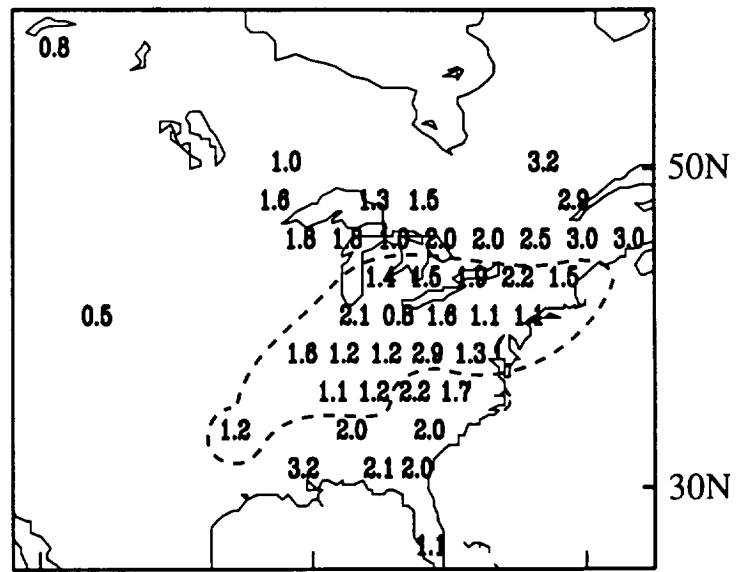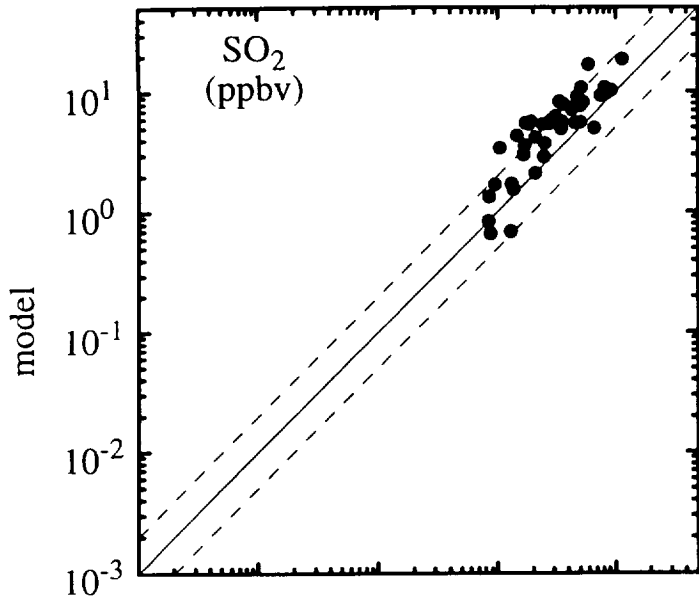
NORTH AMERICA: SUMMER
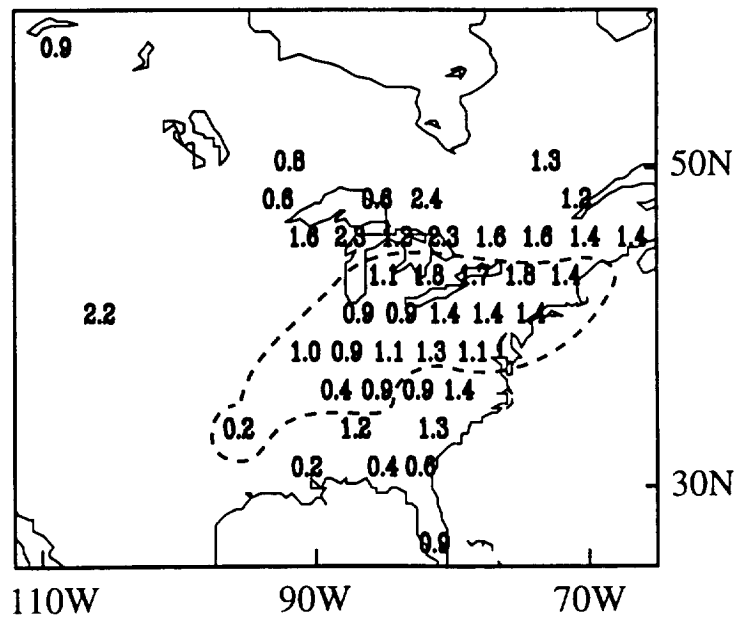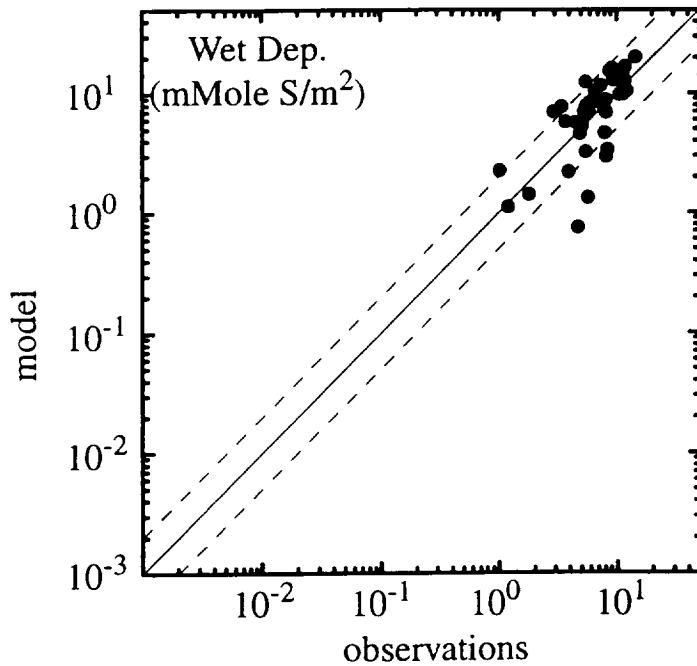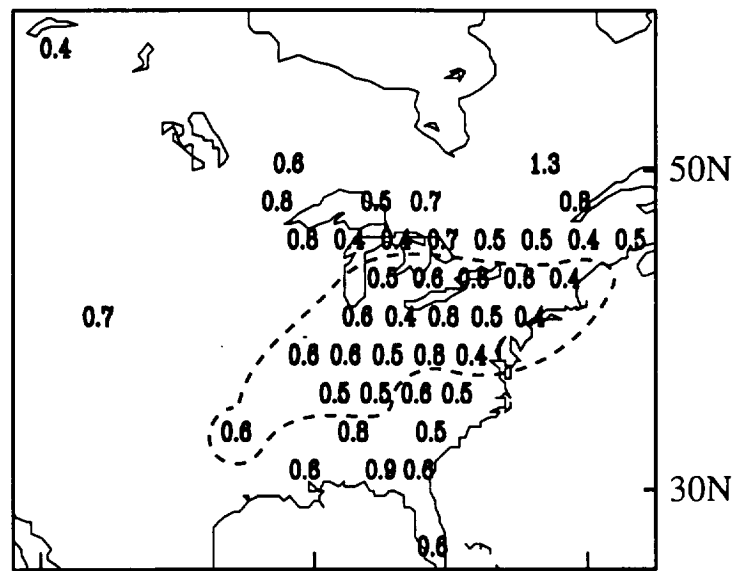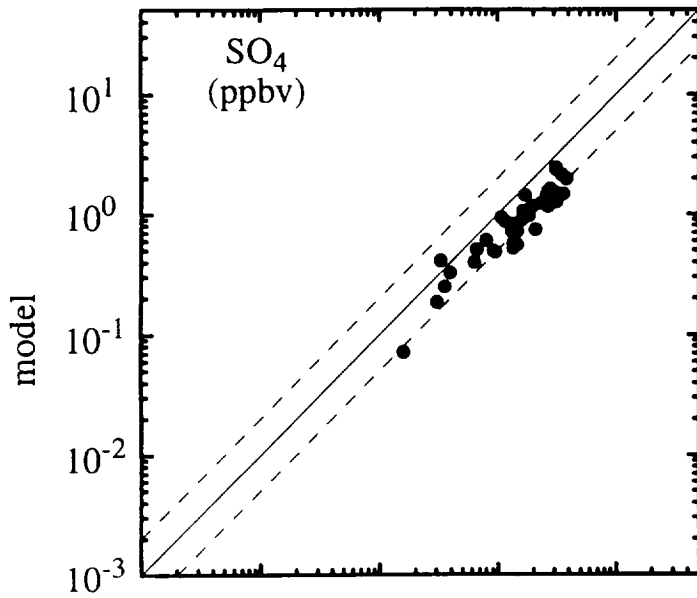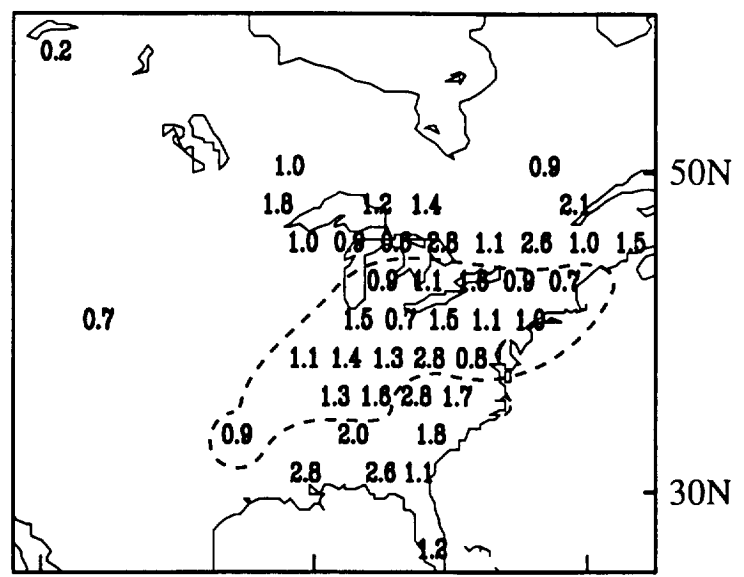
EUROPE: WINTER
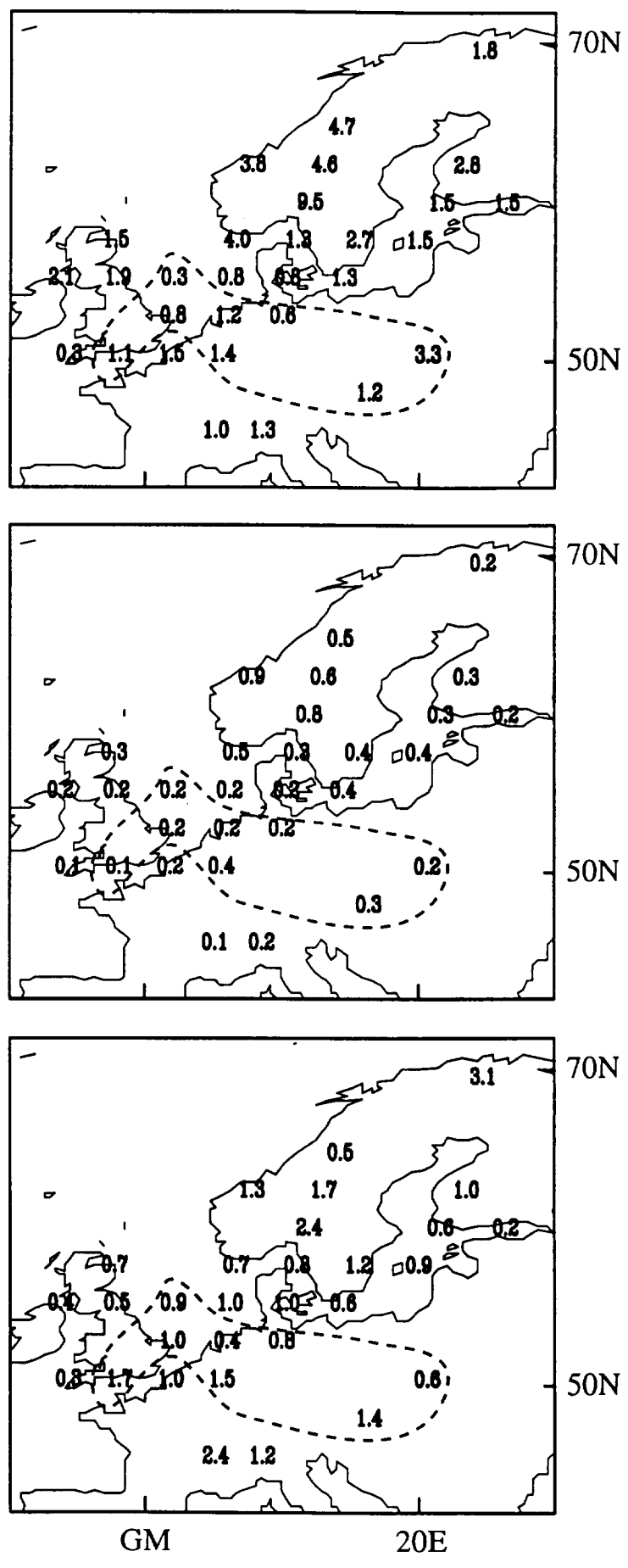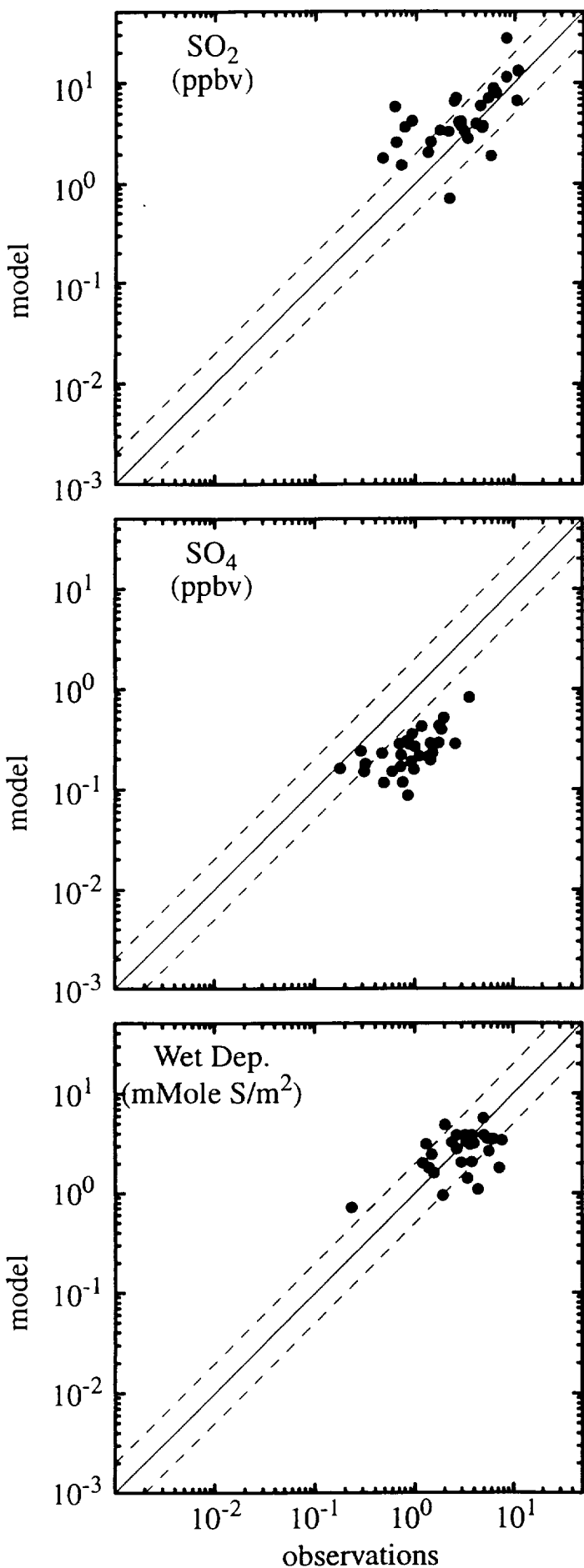
EUROPE: SUMMER
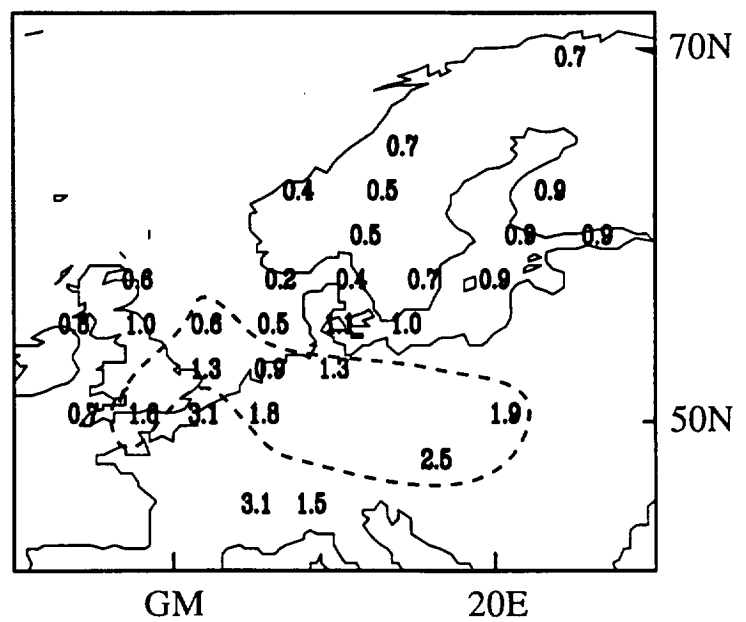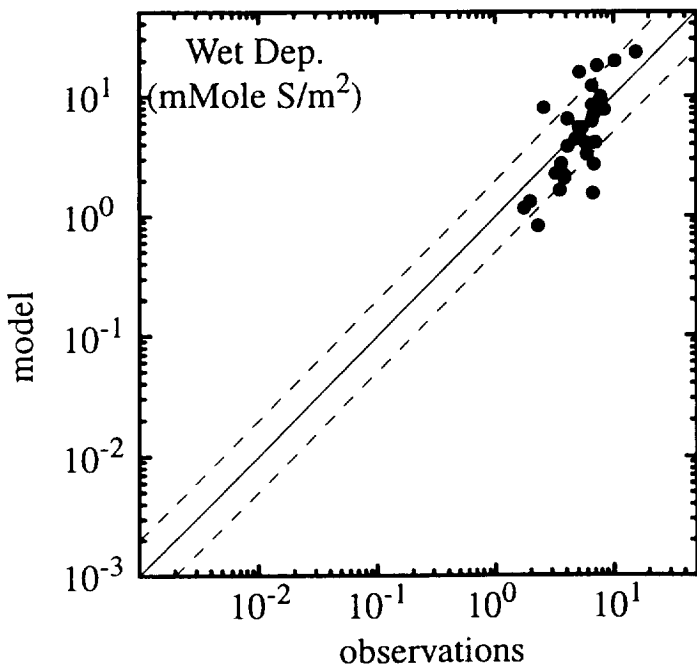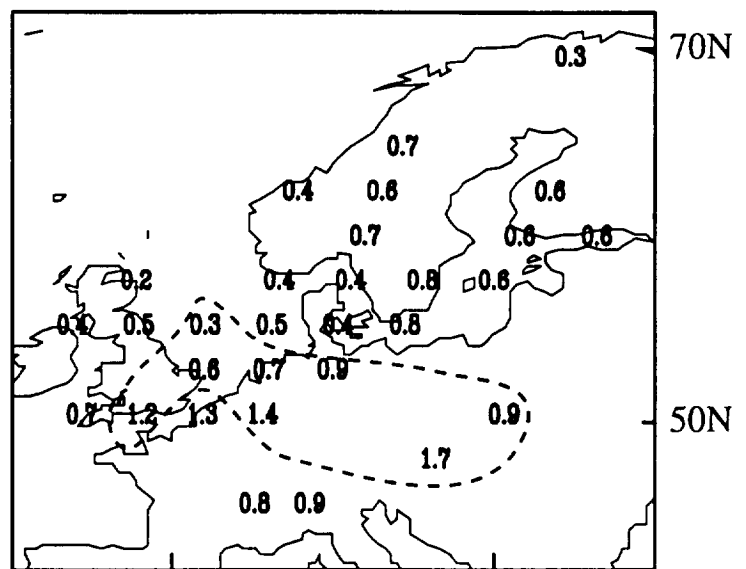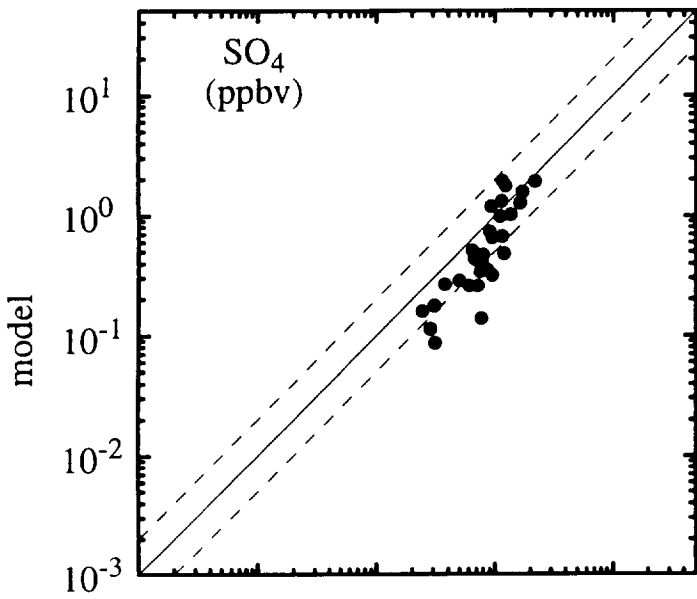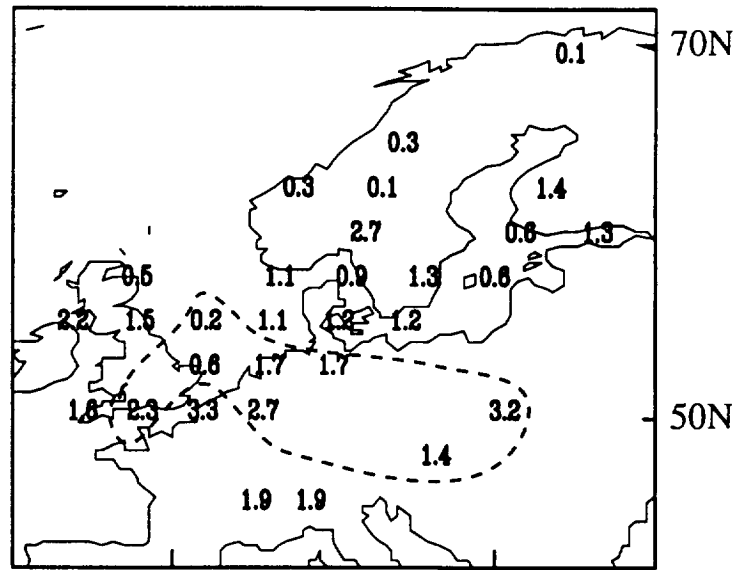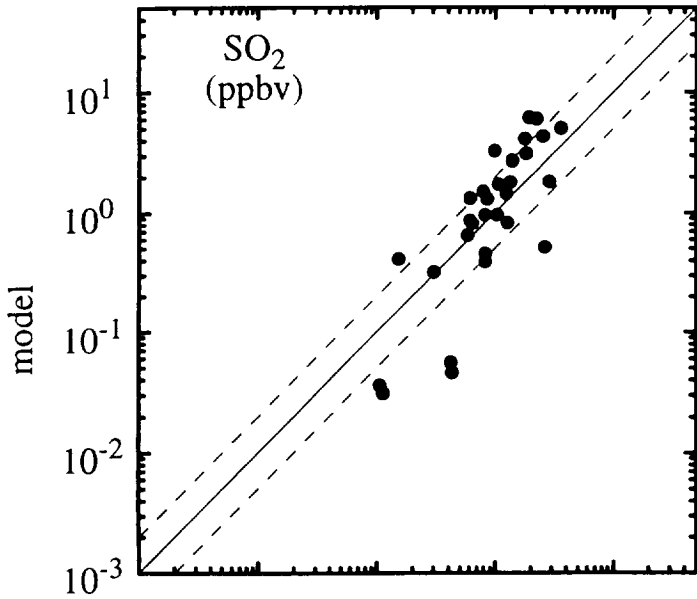
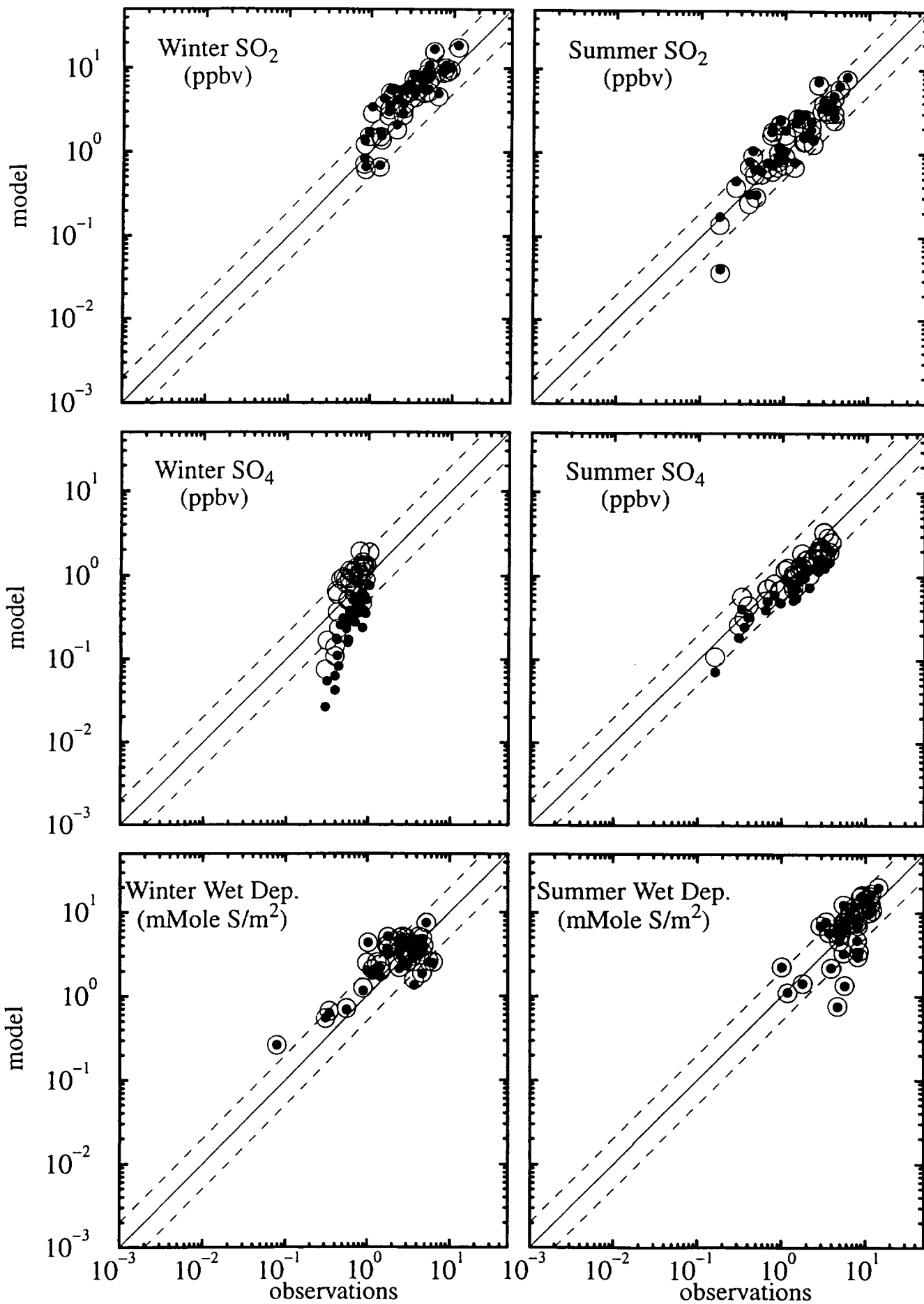NORTH AMERICA: NO-H2O2LIM MODEL
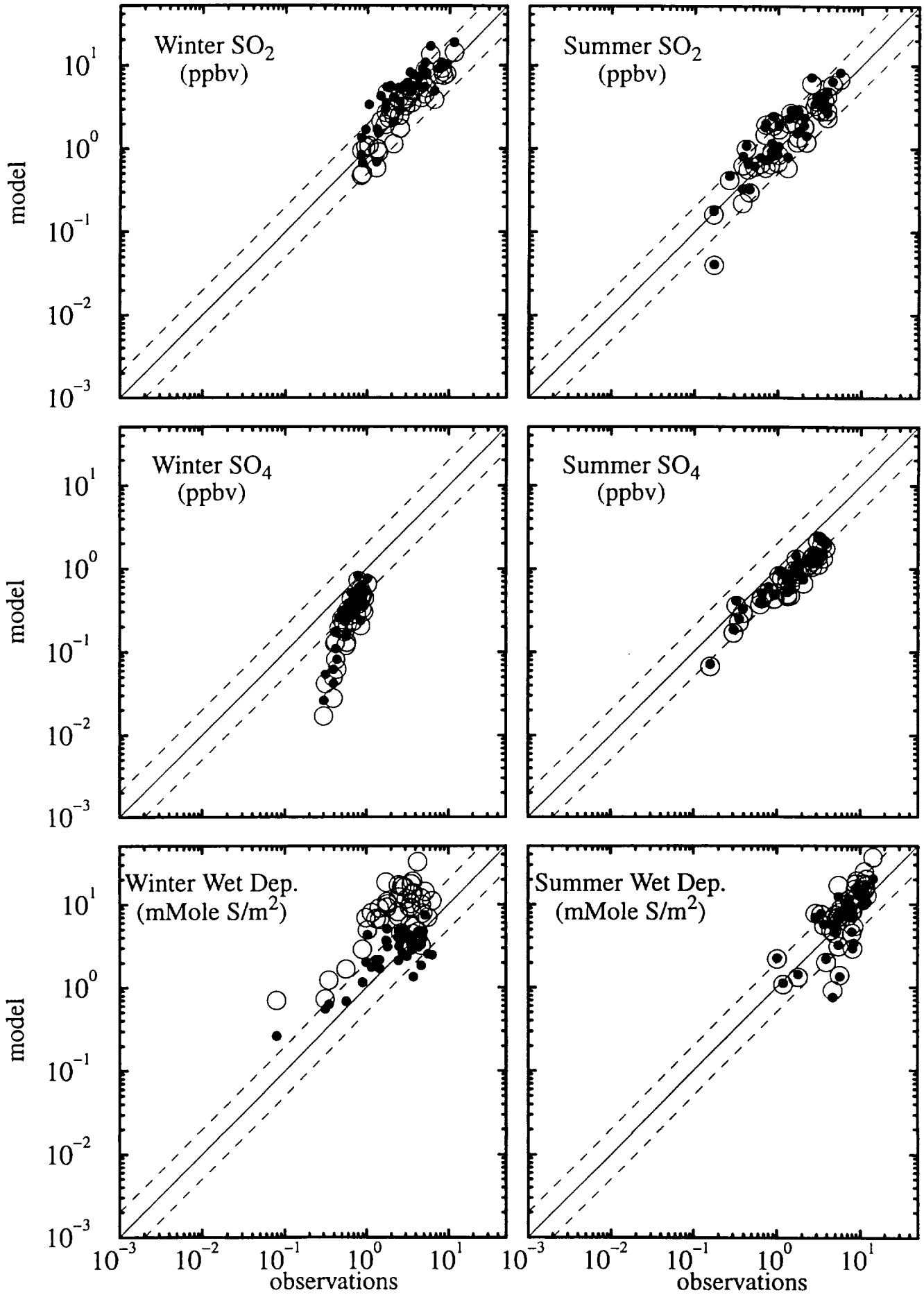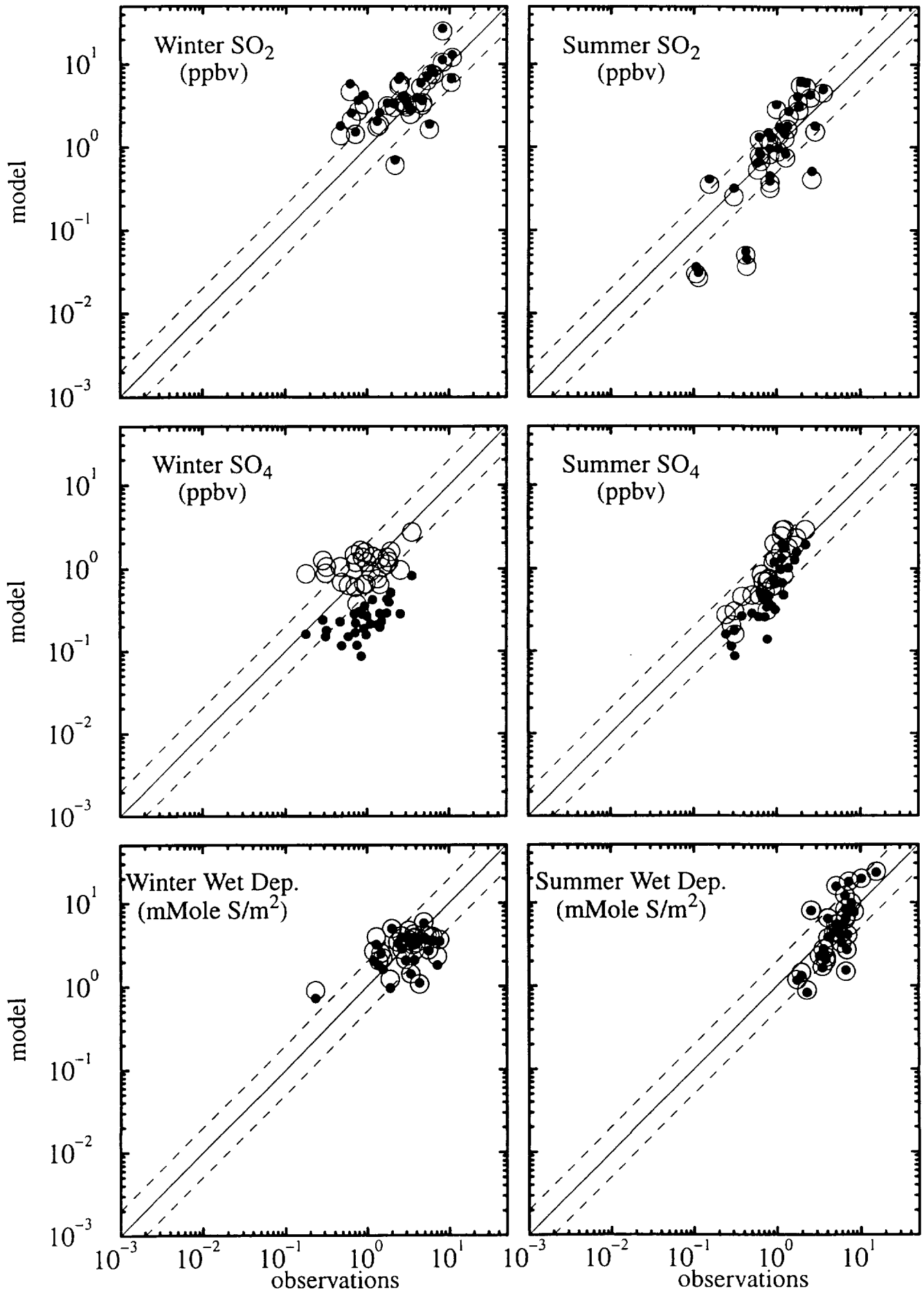
EUROPE: NO-H2O2LIM MODEL
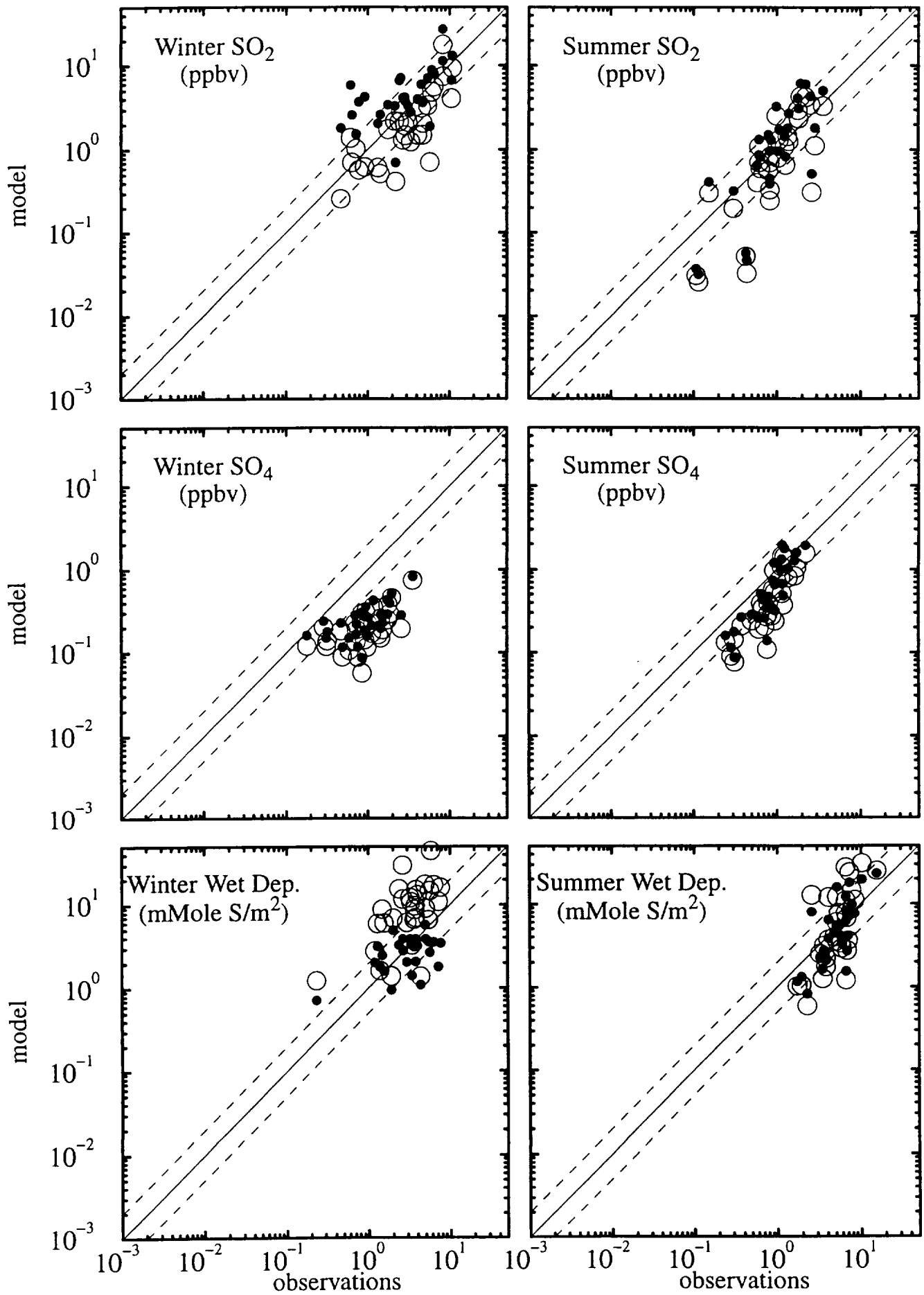
NORTH AMERICA: BL-AQCHEM MODEL

EUROPE: BL-AQCHEM MODEL

Winter SO$_2$ (ppbv)

Summer SO$_2$ (ppbv)

Winter SO$_4$ (ppbv)

Summer SO$_4$ (ppbv)

Winter Wet Dep. (mMole S/m^2)

Summer Wet Dep. (mMole S/m^2)

model
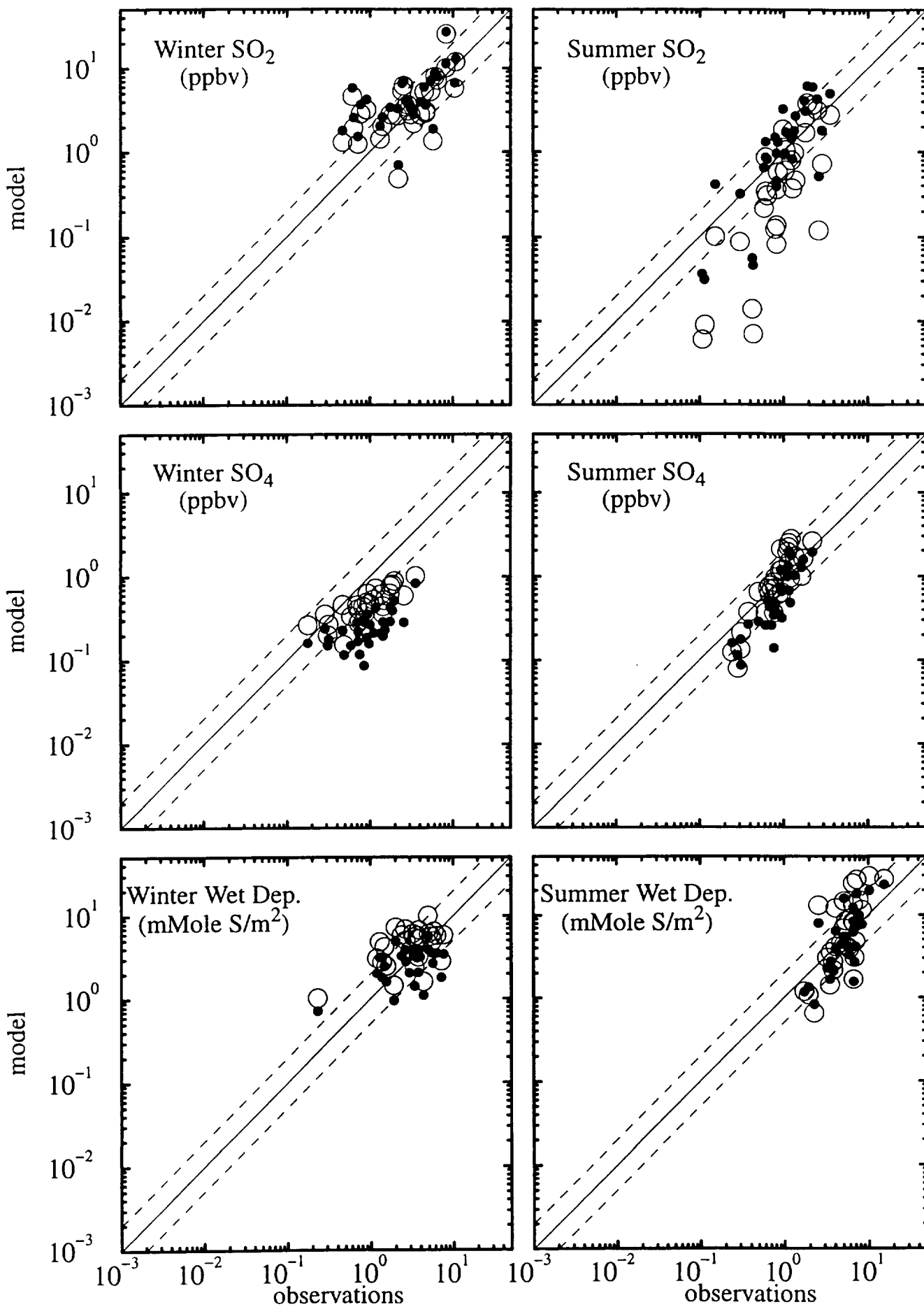
observations

NORTH AMERICA: BL-HETCHEM MODEL

Winter SO$_2$ (ppbv)

Summer SO$_2$ (ppbv)

Winter SO$_4$ (ppbv)

Summer SO$_4$ (ppbv)

Winter Wet Dep. (mMole S/m^2)

Summer Wet Dep. (mMole S/m^2)

model

observations

EUROPE: BL-HETCHEM MODEL

SURFACE SO$_4$: SUMMER/WINTER RATIO

NORTH AMERICA   EUROPE

OBSERVATIONS
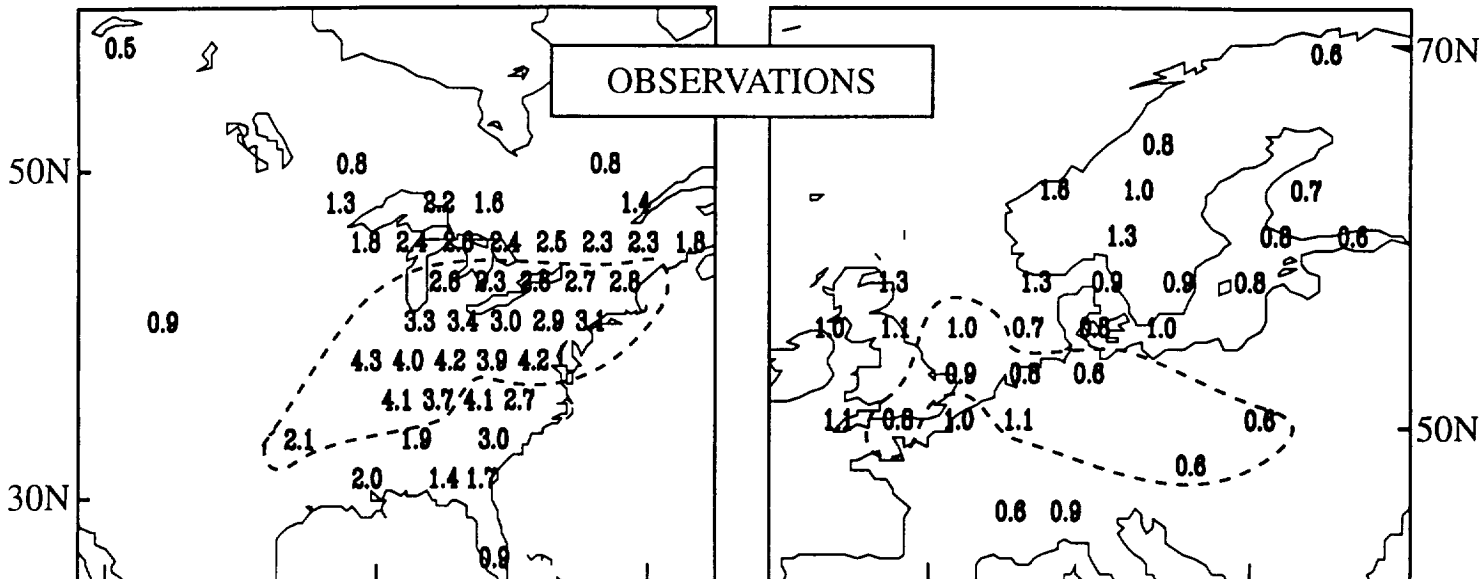
BASE MODEL

BL-HETCHEM MODEL

110W   90W   70W   GM   20E
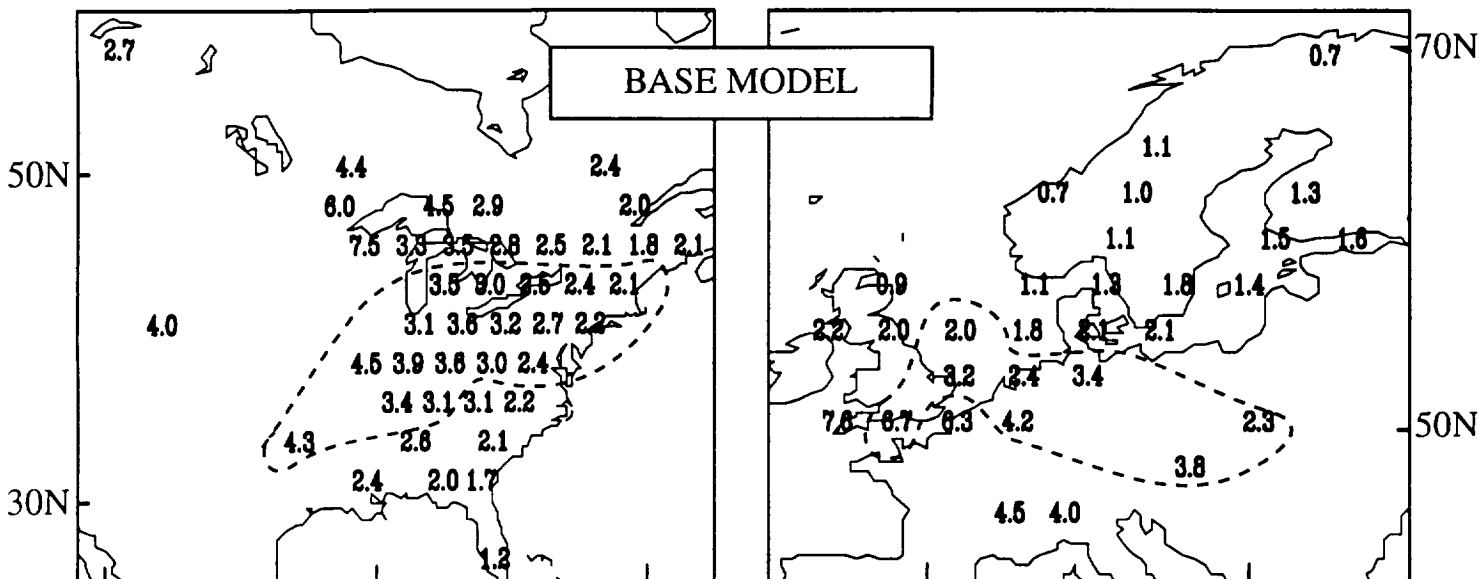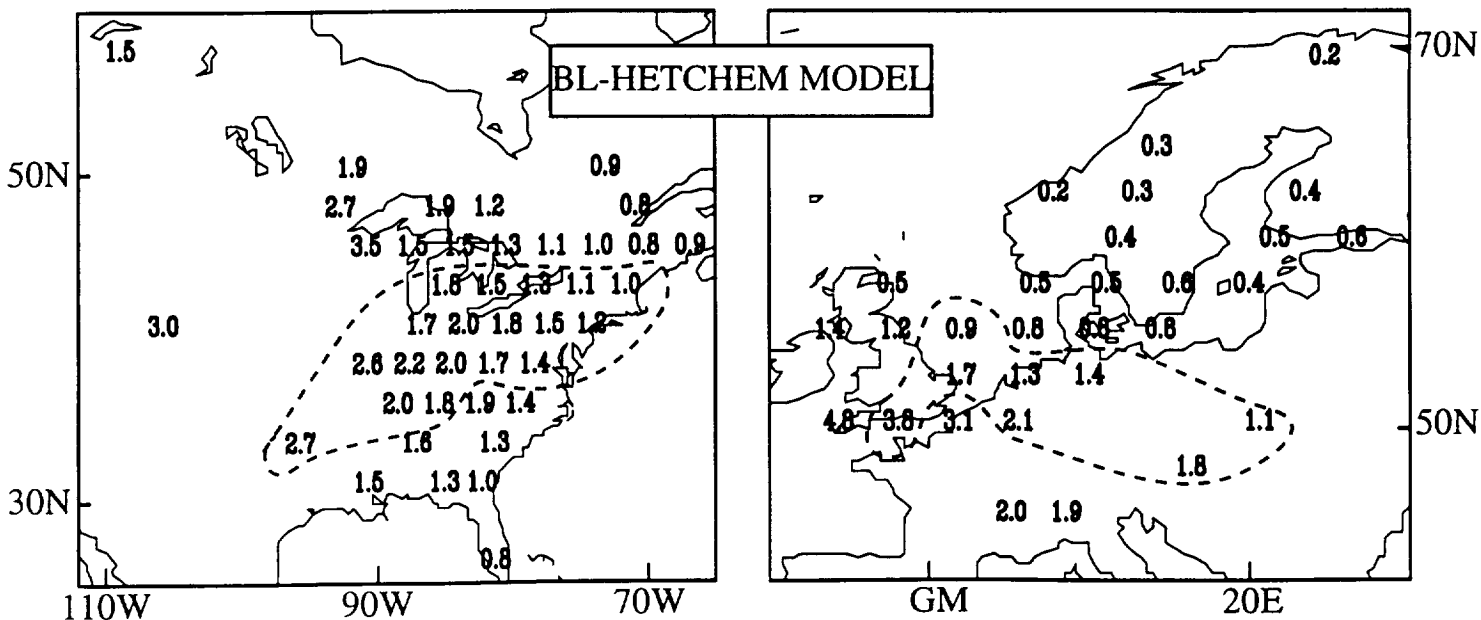
COLUMN SO$_4$ (mg SO$_4$/m^2)

Dec-Jan-Feb Mean
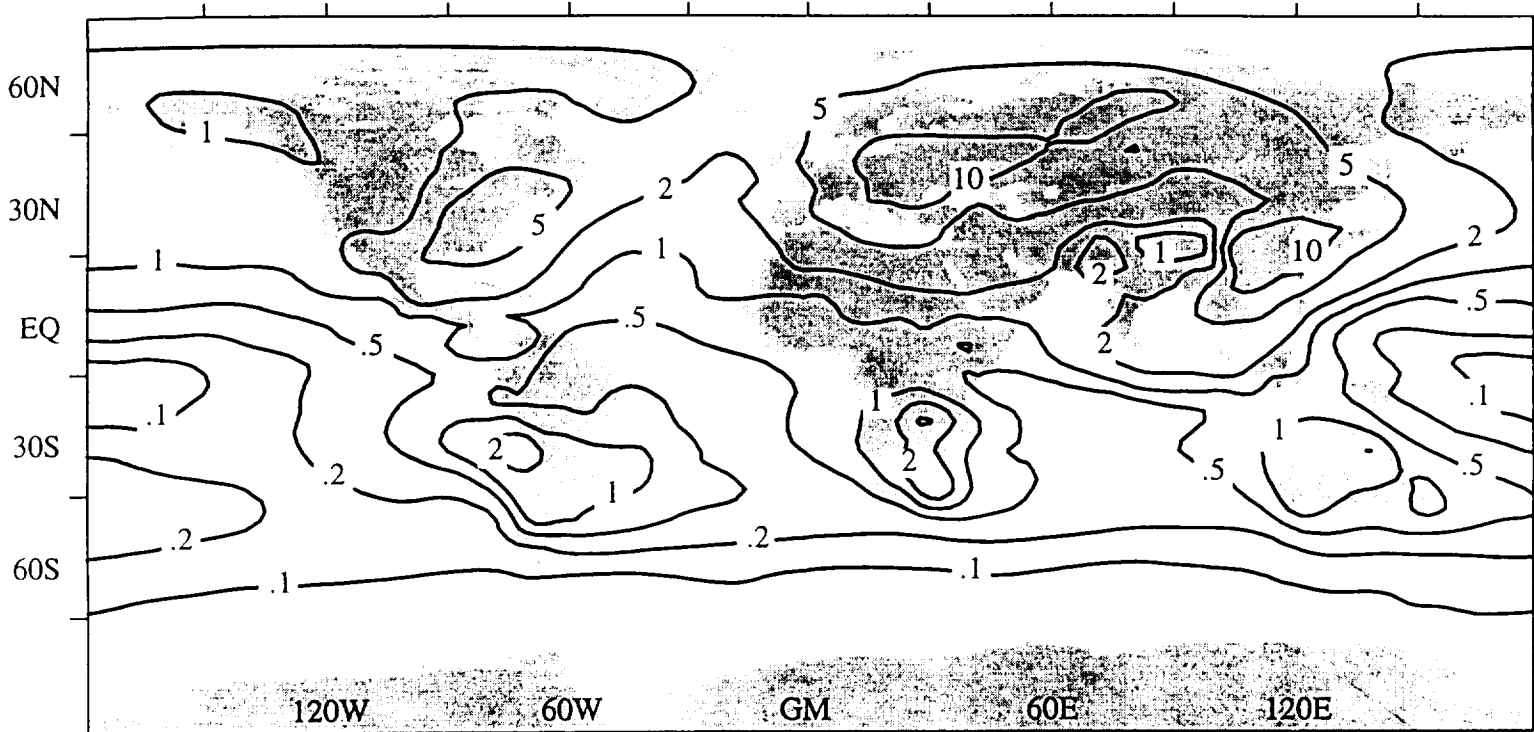
Jun-Jul-Aug Mean

Loss ← | → Production

mg SO$_4$/m^2 or mg SO$_4$/m^2/day

NORTH AMERICA
25N-50N, 60W-100W
SUMMER
WINTER

EUROPE
40N-60N, 10W-40E
SUMMER
WINTER

(Column SO$_4$)/2
Primary Emissions
Gas-phase chemical production
B. L. heterogeneous chemical production
Aqueous-phase chemical production
Dry Deposition
Wet Deposition
Export
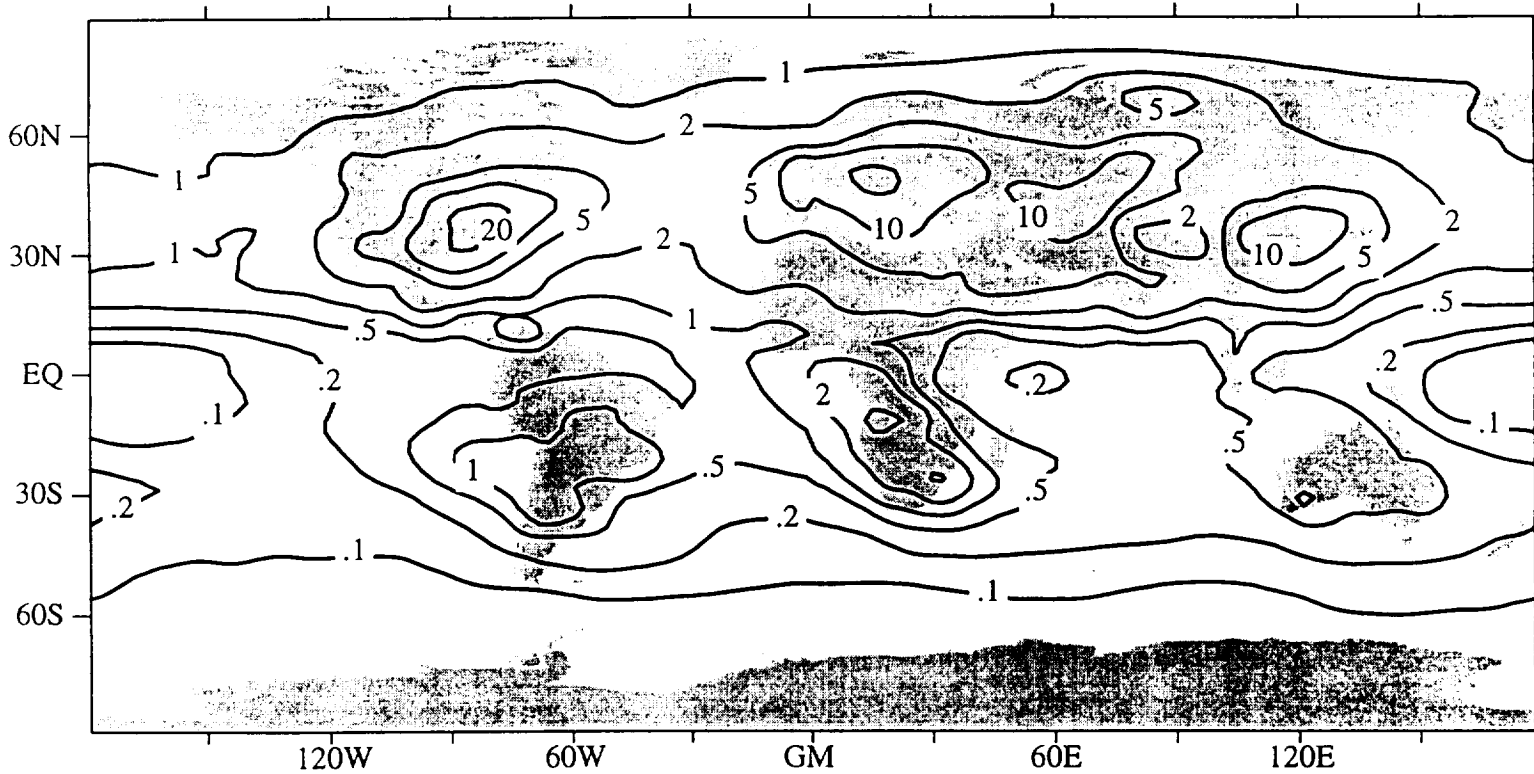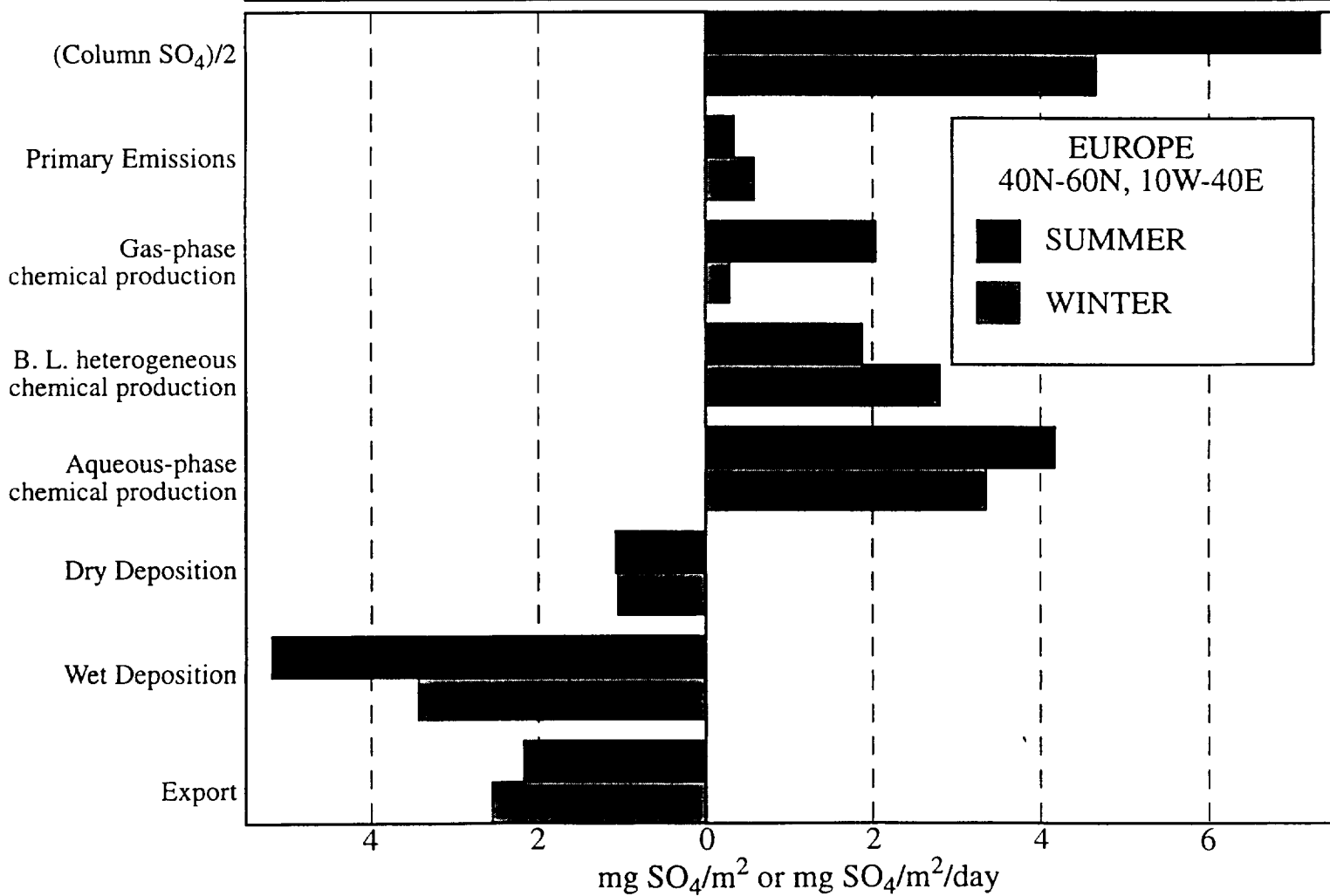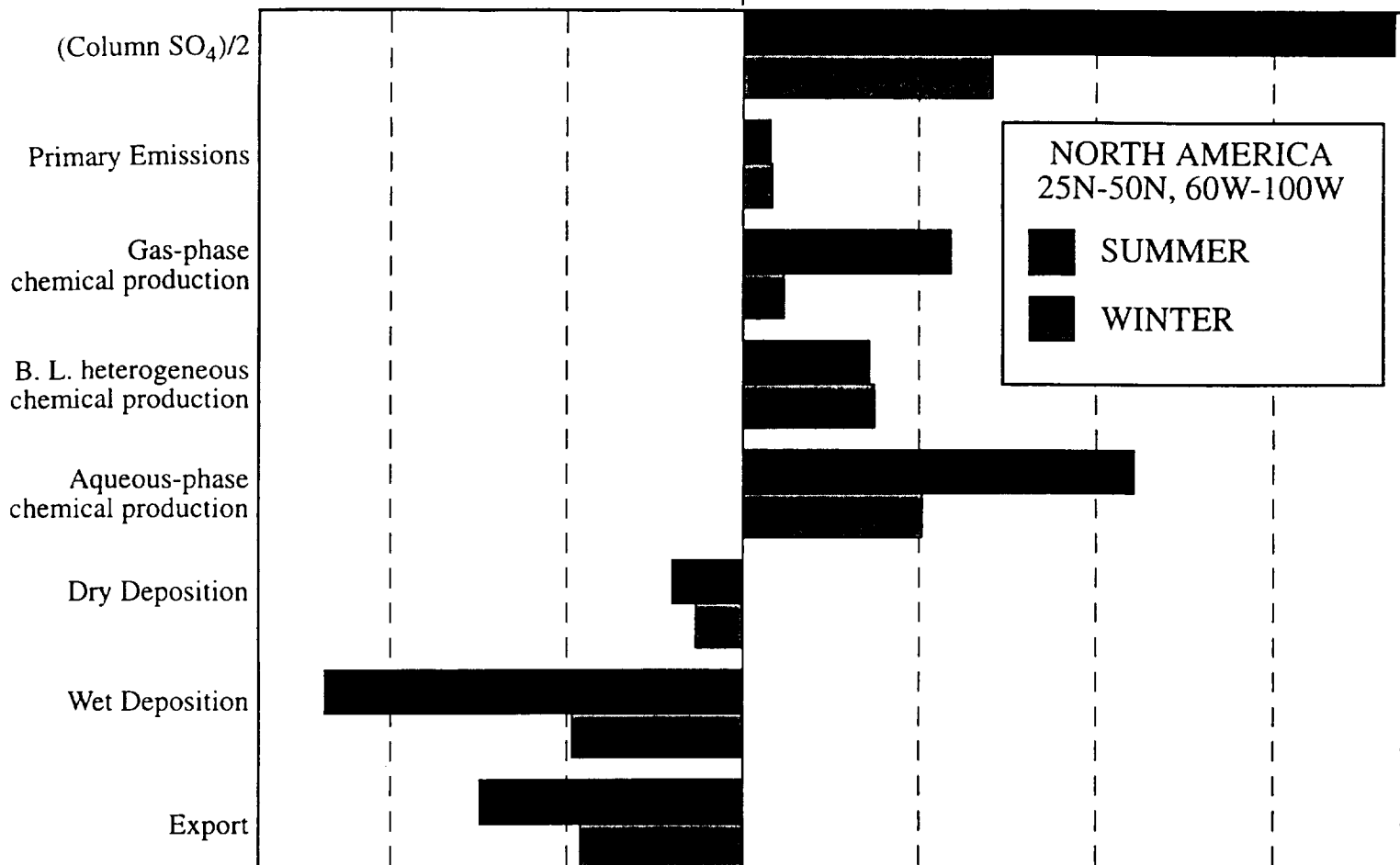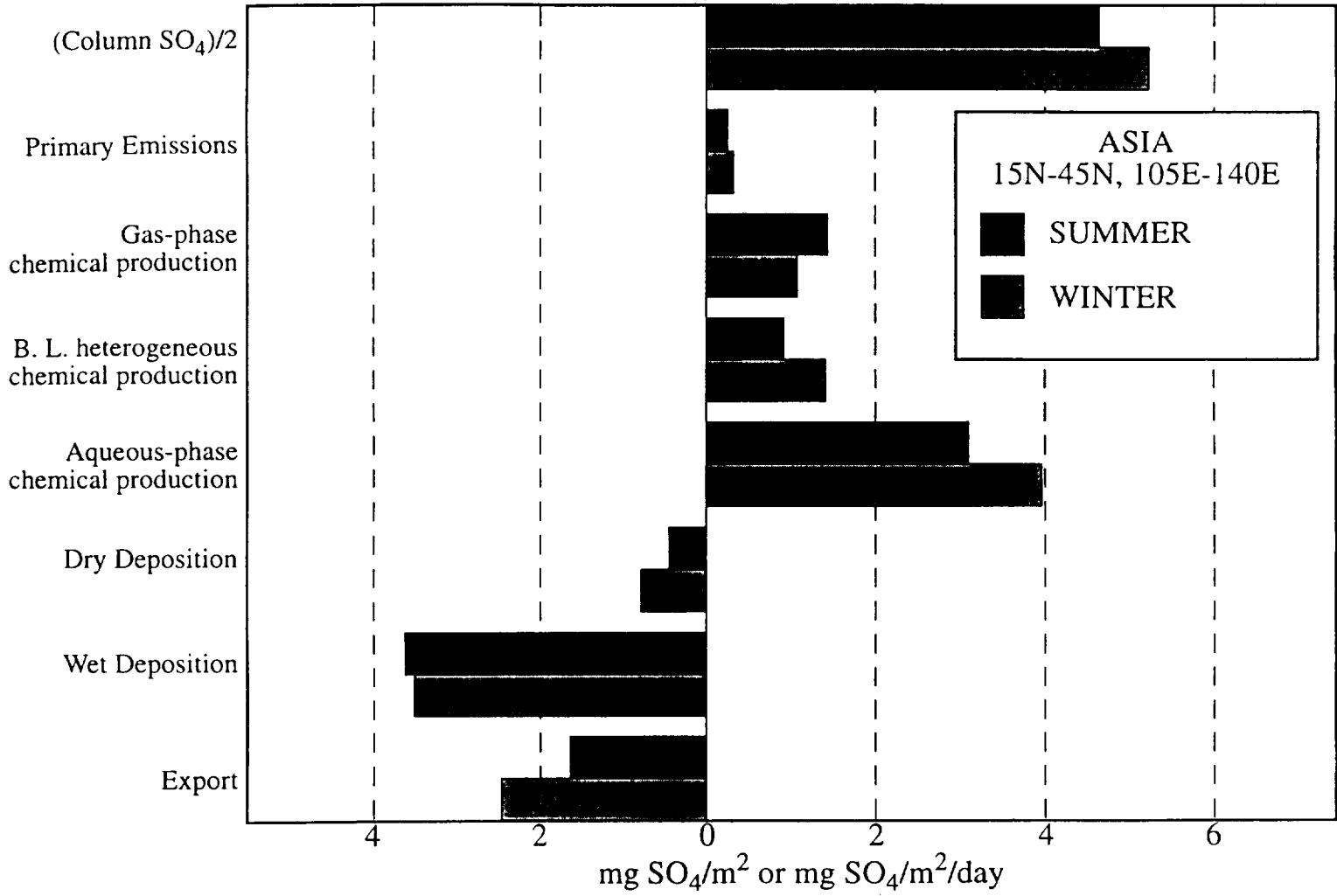
APPENDIX B

Transport-induced interannual variability of carbon monoxide
determined using a chemistry and transport model

Dale J. Allen[1]

Prasad Kasibhatla[2]

Anne M. Thompson[3]

Richard B. Rood[4]

Bruce G. Doddridge[1]

Kenneth E. Pickering[5]

Robert D. Hudson[1]

Shian-Jiann Lin[6]

[1]Department of Meteorology, University of Maryland, College Park,
MD 20742

[2]MCNC/Environmental Programs, Box 12889, Research Triangle Park,
NC 27709

[3]Laboratory for Atmospheres, NASA Goddard Space Flight Center and
Joint Center for Earth System Science, Department of Meteorology,
University of Maryland, College Park, MD 20742

[4]Laboratory for Atmospheres, NASA Goddard Space Flight Center,
Greenbelt, MD 20771

[5]Joint Center for Earth System Science, Department of
Meteorology, University of Maryland, College Park, MD 20742

[6]Laboratory for Atmospheres, NASA Goddard Space Flight Center and
General Sciences Corp., a subsidiary of Science Applications
International Corp.

ABSTRACT

Transport-induced interannual variability of carbon monoxide (CO) is studied during 1989-1993 using the Goddard chemistry and transport model (GCTM) driven by assimilated data. Seasonal changes in the latitudinal distribution of CO near the surface and at 500 hPa are captured by the model. The annual cycle of CO is reasonably well simulated at sites of widely varying character. Day to day fluctuations in CO due to synoptic waves are reproduced accurately at remote north Atlantic locations. By fixing the location and magnitude of chemical sources and sinks, the importance of transport-induced variability is investigated at CO monitoring sites. Transport-induced variability can explain the decrease in CO at Mace Head, Ireland and St. David's Head, Bermuda between the summer of 1991 and the spring of 1993. Transport-induced variability does not explain decreases in CO at southern hemisphere locations. The model calculation explains 80-90% of interannual variability in seasonal CO residuals at Mace Head, St. David's Head, and Key Biscayne, FL and at least 50% of variability in detrended seasonal residuals at Ascension Island and Guam. Upper tropospheric interannual variability in the GCTM during October is less than 10%. Exceptions occur off the western coast of South America where mixing ratios are sensitive to the strength of an upper tropospheric high and just north of Madagascar where concentrations are influenced by the strength of off shore flow from Africa.

1. INTRODUCTION

Carbon monoxide (CO) is an important trace gas for several reasons. In urban areas, high concentrations of CO pollute the air causing health problems. Globally, CO is important because its oxidation by the hydroxyl radical (OH) can be a significant source of tropospheric ozone [*Crutzen*, 1973; *Chameides*, 1978] and a major sink (or source depending on odd nitrogen (NO_x) concentrations) for OH. Reaction with OH is the primary loss mechanism of many atmospheric pollutants and gases. An increase in CO concentrations globally could lead to a decrease in OH, resulting in a decrease in the ability of the atmosphere to cleanse itself [*Sze*, 1977].

CO concentrations are being monitored at over 30 ground based stations as part of the National Oceanic and Atmospheric Administration (NOAA)/Climate Monitoring and Diagnostics Laboratory (CMDL) Cooperative Air Sampling and Atmosphere Ocean Chemistry Experiment (AEROCE) networks [*Novelli et al.*, 1992, 1994a]. CO has been measured from space by the Measurement of Air Pollution from Satellites (MAPS) [*Reichle et al.*, 1986, 1990] instrument and will be measured by the Measurements of Pollution In the Troposphere (MOPITT) [*Drummond*, 1991] instrument as part of the Earth Observing System (EOS). The distribution of CO has also been studied using chemistry and transport models (CTMs) driven by general circulation model (GCM) output [*Pinto et al.*, 1983; *Muller and Brasseur*, 1995]. The importance of convective transport to the budget of CO has been studied over the central United States

[*Thompson et al.*, 1994] and over Brazil [*Pickering et al.*, 1992, 1995].

Measurements of CO at monitoring sites show that CO concentrations vary seasonally and over longer time scales [eg. *Novelli et al.*, 1994a]. Seasonal differences are primarily due to the annual cycle of CO sources and sinks. Interannual differences are due to fluctuations and/or trends in CO emissions, sinks, and chemistry, and to changes in atmospheric circulation or temperature. Long term trends are also variable. Ground based CO concentrations increased by 0.8 to 1.4% per year between 1981 and 1987 [*Khalil and Rasmussen*, 1988] but decreased by about 2% per year between June 1990 and June 1993 [*Novelli et al.*, 1994b]. The recent decrease in CO concentrations may be due to a reduction in anthropogenic sources and biomass burning [*Novelli et al.*, 1994b; *Khalil and Rasmussen*, 1994].

Interannual variability in atmospheric circulation can also lead to uncertainties in the estimation of trends. The importance of transport to interannual variability is clear over synoptic time periods and has been studied at Mace Head, Ireland [*Doddridge et al.*, 1994b]. However, the global importance of transport-induced interannual variability could not be directly calculated until the advent of CTMs driven by assimilated data. A six year (1988-1993) CO calculation has been run using the Goddard CTM (GCTM) driven by assimilated data from the Goddard Earth Observing System data assimilation system (GEOS-1 DAS) [*Schubert et al.*, 1993]. In this calculation, by maintaining a fixed annual cycle of CO sources and

sinks, transport-induced CO variability is evaluated. Assimilated data from GEOS-1 DAS is ideal for studying interannual variability because the analysis system was held constant throughout the assimilation [*Molod et al.*, 1996]. This ensures that model-calculated interannual variability is not due to changes in the analysis system. An understanding of transport-induced interannual variability assists in the interpretation of the CMDL and AEROCE CO monitoring networks.

The model is discussed in section 2. Model-calculated CO distributions are compared to NOAA/CMDL measurements and MAPS data in section 3. Transport-induced interannual variability in the boundary layer and in the upper troposphere are investigated in section 4. Results are summarized in section 5.

2. SOLUTION OF CONSTITUENT CONTINUITY EQUATION

The constituent continuity equation is solved using a 2° in latitude by 2.5° in longitude (2° x 2.5°) version of the GCTM [*Lin et al.*, 1994, *Allen et al.*, 1996b]. This model has 20 sigma levels, (about 13 in the troposphere) chosen to match the vertical levels of the GEOS-1 atmospheric general circulation model (GEOS-1 AGCM) [*Takacs et al.*, 1994].

Output from the multi-year GEOS-1 DAS is used to drive the CTM in an off-line mode. The GEOS-1 DAS fields used to solve the continuity equation for CO are the u and v components of the wind, the surface pressure, the temperature at 0, 6, 12, and 18 Universal

Time (UT), the three-hour averaged planetary boundary layer (PBL) depth, and the six-hour averaged convective mass flux. A twelve minute time step is used with fields interpolated to the appropriate transport time before using.

2.1 The model

The mixing ratio change due to advection is solved using a multi-dimensional and semi-Lagrangian extension of the piecewise parabolic method (PPM) [*Lin and Rood*, 1995; *Lin et al.*, 1994]. The horizontal wind components poleward of 70° are filtered with a Fast Fourier Transform before using to remove noise.

The algorithm used to calculate the mixing ratio change due to turbulent mixing is described in *Allen et al.* [1996b]. Turbulent mixing in the GCTM is confined to the PBL. During a CTM time step, a fraction ($\alpha=0.125$) of material in each model layer within the PBL is mixed uniformly throughout the PBL.

The algorithm used to parameterize convective mixing is described in the appendix. Briefly, GCTM convection is parameterized using cloud mass flux information from the Relaxed Arakawa-Schubert (RAS) algorithm [*Moorthi and Suarez*, 1992; *Arakawa and Schubert*, 1974] that was used to parameterize convection in the GEOS-1 AGCM. The mixing ratio change due to convection is determined by solving iteratively a coupled linear system that defines the mass flux due to convection across the edges of model layers.

2.2 Specification of CO sources and sinks

Four major global sources of CO have been identified: fossil fuel combustion, biomass burning, oxidation of nonmethane hydrocarbons (NMHCs), and oxidation of methane (CH_4).

A global CO inventory is not yet available; therefore, CO emission due to fossil fuel combustion is assumed to be proportional to anthropogenic NO_x emissions. NO_x emissions were obtained from the 1985 Global Emissions Inventory Activity (GEIA) data base [Benkovitz et al., 1996]. It is assumed that 7.9 moles of CO are emitted per mole of NO_x emitted from fossil-fuel combustion, based on EPA estimates for the United States for 1985 [EPA, 1993]. The actual CO/NO_x emission ratio is greater for mobile sources (eg. automobiles) than for point sources (eg. heavy industry) [Buhr et al., 1992]. Therefore, the assumption of a uniform emission ratio is clearly a simplification. Measured values of the CO/NO_x emission factor are given in Lonneman et al. [1986], Pierson et al. [1990], and Buhr et al. [1992]. Emissions by fossil fuel combustion are assumed to be constant with time and are put into the lowest model layer.

CO emission from biomass burning is calculated assuming a CO/CO_2 volume ratio of 0.08 in biomass burning [Andreae et al., 1988]. Estimated emission ratios for savanna fires in Brazil, Ivory Coast, and Australia are between 0.053 and 0.113 [Hurst et al., 1994; see also Crutzen and Andreae, 1990]. Carbon emissions due to deforestation and savanna fires in tropical America, Africa, and Asia were obtained on a 5° x 5° grid from Hao et al. [1990].

Emissions are apportioned throughout the year using information on climatology, cultural practices, and vegetation types in 15 tropical regions [*Richardson*, 1994]. *Hao et al.* [1990] did not include Australian emissions. In this calculation, Australian CO emissions are assumed to be constant with time and equal to 8% of total tropical emissions [*Hao et al.*, 1990].

NMHC oxidation also releases CO. Isoprene (C_5H_8) and monoterpene ($C_{10}H_{16}$) emissions were obtained for each month from the 1985 GEIA inventory. Oxidation of one mole of isoprene is assumed to yield 2.5 moles of CO. *Miyoshi et al.* [1994] found that oxidation of one mole of isoprene under NO_x-rich (NO_x-free) conditions yields 2.75 (0.55) moles of CO and estimated the global yield to be 1.5 moles of CO per mole of isoprene. Therefore, model-calculated CO production from isoprene oxidation is overestimated in regions such as the southern hemisphere (SH) where NO_x concentrations are usually low. Oxidation of a mole of monoterpene is assumed to produce 0.8 moles of CO [*R. Saylor*, personal communication, 1995].

The final source of CO considered is oxidation of methane (CH_4). CO is an end product of

$$CH_4 + OH \;\rightarrow\rightarrow\rightarrow\; OTP \;\rightarrow\rightarrow\rightarrow\; CO \qquad\qquad (1),$$

where OTP = other products. The reaction rate constant (k) equals $2.65 \times 10^{-12} \exp(-1800/T)$ where T is temperature [*DeMore et al.,*, 1994]. CH_4 is assumed to be uniform in height and longitude, and its latitudinal gradient is taken from Fig. 6 of *Steele et al.* [1987]. In order to focus on transport variability, the CH_4 mixing ratio

is held fixed throughout the simulation at the values shown in Table 1. The OH distribution was obtained by monthly averaging and interpolating the OH distribution from the Harvard CTM [*Spivakovsky et al.*, 1990]. Harvard OH is based on a calculation of OH as a function of temperature, ultraviolet irradiance, water vapor (H_2O), CO, ozone (O_3), CH_4, and total odd nitrogen (see *Spivakovsky et al.*, [1990] for their definition). The use of an equilibrium amount of OH simplifies the calculation but does not allow for feedback between CO and OH. The CO-OH feedback is not crucial for this calculation since the effect of chemical perturbations on multi-year trends is not being calculated. Additionally, halocarbon-based estimates of OH concentrations have shown little change from 1978 to 1994 [*Prinn et al.*, 1995].

The geographical distributions of annually averaged CO emissions due to fossil fuel combustion, NMHC oxidation, and biomass burning are shown in Figs. 1a-c, respectively. Fossil fuel combustion is the dominant northern hemisphere (NH) source and is largest in highly populated regions. Biomass burning is an important CO source in portions of South America and Africa. NMHC oxidation is important in the tropics and in the summer hemisphere. Model-calculated global CO sources are compared to estimates by *Logan et al.* [1981], *Seiler and Conrad* [1987], and *Pacyna and Graedel* [1995] in Table 2 [see also *WMO*, 1992]. The total global CO source in the GCTM is lower than tabulated estimates because of a lower estimate of the biomass burning and fossil fuel sources and the neglect of CO emission from vegetation and oceans. The biomass

burning source is considerably less than the tabulated estimates because a relatively low CO/CO_2 emission factor was used, emissions due to burning of agricultural wastes, fuel wood, and charcoal were neglected, and because extratropical emissions were neglected. The addition of emissions due to agricultural wastes, fuel wood, and charcoal increase total tropical CO_2 emissions by about 20% [*Andreae*, 1991]. The neglect of CO emission due to extratropical burning may also be important. An analysis of Arctic Boundary Layer Expedition (ABLE 3A) chemical measurements and wind trajectories showed that summertime boreal fires are a significant high latitude source of CO [*Wofsy et al.*, 1992; *Shipham et al.*, 1992; *Harriss et al.*, 1992].

CO is destroyed through the reaction

CO + OH --> products   (2),
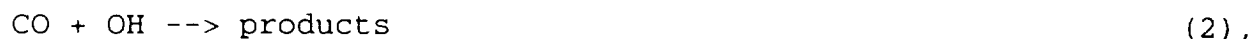
where k equals $1.5 \times 10^{-13} * (1+0.6 \times P)$ and P is pressure in atmospheres [*DeMore et al.*, 1994]. CO loss due to consumption by biological processes is not included. Its magnitude is believed to be less than 10% of the magnitude of loss due to reaction with OH [*Logan et al.*, 1981]

3. MODEL CLIMATOLOGY

The CO calculation was initialized on January 1, 1988 with CO set to zero at all grid points. The calculation was run through October 31, 1993 with CO amounts from each source saved separately every six hours.

3.1 Global distribution

The latitudinal distributions of model-calculated and measured CO are compared for the December-February, March-May, June-August, and September-November seasons in Figs. 2a-d, respectively. The "CMDL" average for each season was constructed by averaging July 1988 to June 1993 NOAA/CMDL measurements with unique time stamps taken during each season. Measurements flagged as being non-background are excluded from the average. The sites used in the latitudinal averages are listed in Table 3. Only NOAA/CMDL sites at which CO data has been released through an anonymous ftp server to the general science community are used in the average. The "Model CMDL" average was calculated using surface layer (the lowest layer of the model, ≈12 hPa deep) output at the grid volume containing the measurement site. The "Model (all)" average was calculated using zonally averaged surface layer model output for the appropriate season. The model was sampled as close to the measurement time as possible for both the "Model (all)" and "Model CMDl" averages.

The main features of the distribution of CO are reproduced by the model. Lowest concentrations are found in the SH during December-February and highest concentrations are found in the northern hemisphere (NH) during the same months. The slopes of the distributions are also similar. During December -May, measured and model-calculated CO amounts increase rapidly between 60°S and 30°N. The increase is smaller during June-August when biomass burning causes a peak between 30°S and the equator. The large

peak in NOAA/CMDL CO at 36°N is caused by extremely polluted air in the Qinghai Province of China. Model-calculated concentrations at this location are at least 50 ppbv less. During most seasons, model-calculated concentrations are 5-25% higher than CMDL concentrations in the SH and about the same percentage lower at mid and high latitudes of the NH. The low bias in the NH is believed to be due to the neglect of CO emission by boreal fires. The high bias in the SH is primarily due to an overestimation of the SH CO source from NMHC oxidation. CO concentrations constructed using model output at CMDL stations are lower than CO concentrations calculated by zonally averaging model output because most NOAA/CMDL sites are placed at marine locations.

The mean 1989-1993 latitudinal distributions of 500 hPa CO during April and October are compared to April 9-19, 1994 and September 30-October 11, 1994 MAPS measurements in Figs. 3a-b. The MAPS instrument is designed to measure CO concentrations in the middle troposphere and values from it are believed to be most representative of 490 hPa [*V. Connors*, personal communication, 1995]. Model-calculated concentrations are within a standard deviation of measured concentrations at nearly all latitudes during both seasons although significant differences do exist between the shapes of the distributions. During April, measured CO concentrations are nearly constant between 60°S and 30°S while model-calculated concentrations increase gradually from 60°S to 30°S. In addition, the rapid increase in CO with latitude between 10°S and 10°N is underestimated by the model. Larger differences

11

are seen during October. Model-calculated CO concentrations between 10°S and 25°S are about 30 ppbv less than mean CO concentrations from MAPS. Model-calculated concentrations are less because biomass burning was underestimated especially in Asia, and because the moist convective algorithm in the GCTM tends to move too much material from the PBL to the upper troposphere directly leading to an underestimation of concentrations in the mid-troposphere [*Allen et al.*, 1996b; *Allen*, 1996a]. Concentrations at high northern latitudes are also underestimated presumably due to the neglect of CO emission by boreal fires.

The mean model-calculated (1989-1993) distributions of CO at 500 hPa during April and October are compared in Figs. 4a-b. During April, model-calculated concentrations exceed 105 ppbv north of 40° to 50°N and also over Colombia and the Gulf of Guinea. During October, model-calculated concentrations are largest in a region extending from northern South America to western and southern Africa. The model calculation did not reproduce a region of high CO concentrations seen by MAPS during October 1994 near Indonesia [*V. Connors*, personal communication, 1995].

The contributions of fossil fuel combustion, oxidation of NMHCs, biomass burning, and oxidation of CH_4 to the mean 500 hPa model-calculated CO distribution during October are shown in Figs. 5a-d, respectively. The contribution from methane oxidation is nearly uniform with latitude. CO amounts from this source range from 29 ppbv at high southern latitudes to 33 ppbv at equatorial locations. CO from fossil fuel combustion has a strong latitudinal

gradient in the NH. CO amounts from fossil fuel combustion are greater than 35 ppbv at high northern latitudes, fall off rapidly through the mid-latitudes, and are as small as 5 ppbv in the SH. Large amounts of CO from biomass burning [see *Watson et al.*, 1990] and NMHC oxidation are evident in the tropics over continents. Biomass burning during August and September is much larger in the SH than in the NH. By October, model-calculated CO mixing ratios due to biomass burning exceed 60 ppbv in southern Africa but are less than 10 ppbv in most of the NH. NMHC oxidation contributes 20-30 ppbv over most of the globe but more than 70 ppbv in northwestern South America.

The mean model-calculated CO distribution for October 1989-1993 in the boundary layer (assumed to be the lowest 3 layers of the model; approximately 90 hPa in depth) is shown in Fig. 6a. Boundary layer concentrations exceed 500 ppbv in portions of South America and Africa where biomass burning is extensive. Monthly average measured concentrations in a region of burning near Cuiabá, Brazil exceeded 650 ppbv [*Kirchhoff et al.*, 1989]. Another feature of the boundary layer distribution is tongues of elevated CO extending eastward from source regions in Europe and westward from source regions in equatorial South America and Africa.

Locations where interannual CO variability is large were identified by calculating standard deviations of residuals from the 1989-1993 October means. The relative importance of interannual variability is shown in Fig. 6b which shows the normalized standard deviations as a function of longitude and latitude. Model-

calculated interannual variability is less than 3% at locations where CO is nearly uniform but more than 12% at locations such as the eastern north Atlantic, the southern tip of South Africa, and western India, where CO gradients are large. Interannual variability in the eastern north Atlantic (Mace Head, Ireland) was studied as part of AEROCE.

3.2 Atmospheric variability

As part of AEROCE, CO was measured almost continuously between September 1992 and September 1993 at Heimaey, Iceland (63°N, 20°W) and between August 1991 and January 1993 at Mace Head, Ireland (53° N, 10° W). The experimental technique and sampling protocol are discussed in *Doddridge et al.* [1994a, 1994b]. Descriptions of the Mace Head and Heimaey measurement sites are given in *Jennings et al.* [1991, 1993] and *Prospero et al.* [1995], respectively. Surface layer model output is compared to daily average AEROCE measurements in Figs. 7a-b. A seasonal cycle is evident at both locations and is captured by the model although model-calculated summertime concentrations are lower than measurements at Heimaey. The most striking feature of the CO distributions at Mace Head and Heimaey are the abrupt increases that occur when polluted European air reaches these sites [*Jennings et al.*, 1993, 1995; *Doddridge et al.*, 1994b]. The amplitude, length, and timing of most of these events is captured by the model with only a few spring events missed. A major strength of the GCTM is its ability to resolve the transport of pollutants to island sites in the northern Atlantic

[eg. *Allen et al.*, 1996b].

Fall (September-November) CO measurements are available at Mace Head, Ireland during 1991 and 1992. Statistics from the AEROCE measurements [*Doddridge et al.*, 1994b] and from the model for the fall seasons are shown in Table 4. Flow from Europe was more common during 1991 resulting in larger concentrations and a larger standard deviation. Model-calculated means were slightly lower than observed means, but interannual variability in mean CO concentrations and in CO variability was well captured by the model. Measured (model-calculated) 1991 means exceed 1992 means by 42 (34) ppbv. Standard deviations calculated from 1991 measurements and 1991 model output exceed 1992 standard deviations by a factor of 3.5. Interannual variability is especially large at Mace Head due to its proximity to large CO sources in Europe. The ability of the GCTM to simulate variability at other locations where measurements are less frequent and CO gradients are smaller is examined by comparing model output with NOAA/CMDL measurements.

3.3 Annual cycle at NOAA sites

Because of the approximations used in specifying chemical sources and sinks, the investigation of interannual variability will be limited to the marine and coastal locations shown in Fig. 8. Longitudes and latitudes of these sites are listed in Table 3. Model-calculated and observed monthly average means at these sites are compared in Figs. 9a-k. Model-calculated means were obtained

by averaging daytime surface layer model output for each day of the month. Measured means were calculated by *Novelli et al.* [1991, 1994a] using a curve fitting technique. Measured means are likely to be biased low, since measurements are usually taken during periods when "background " air is expected. Measurements were taken 2-4 times per month, and the date of the first measurement at each site is listed in Table 3.

The observed annual cycle of CO is reproduced reasonably well at all locations except Christmas Island where it is completely missed. Measured CO concentrations at Christmas Island show a strong peak during the late NH winter and a much smaller peak during the late NH summer. Model-calculated CO concentrations show a strong peak during the late NH summer and fall. The amplitude of the annual cycle is overestimated at Ascension Island possibly due to an overestimation of CO emission in southern Africa due to savanna fires [*Scholes et al.*, 1995]. The seasonal cycle is also overestimated at Cape Grim and underestimated at Seychelles. In general, model-calculated concentrations are too low in the NH and too high in the SH.

4. INTERANNUAL VARIABILITY

4.1 NOAA/CMDL sites

The importance of transport-induced interannual variability at NOAA/CMDL sites is assessed by evaluating how well a model without interannual chemical variability and interannual variability in CO

emissions reproduces interannual fluctuations in seasonal CO concentrations.

Since the lifetime of CO is long compared to the lifetime of synoptic systems, CO concentrations away from source regions are determined to a large extent by atmospheric flow patterns. Flow patterns are variable due to barotropic and baroclinic instabilities. Mean CO concentrations vary from year to year as the location, strength, and timing of disturbances caused by instabilities change. Causes of interannual variability in atmospheric flow patterns are varied. *Doddridge et al.* [1994b] speculate that interannual variations in flow to Mace Head during the fall are caused by changes in external forcing from the tropics. Interannual variability in mean NOAA/CMDL CO concentrations may be especially large because measurements are taken infrequently, allowing fluctuations in CO concentrations due to synoptic systems to remain.

Seasonal means at NOAA/CMDL stations are constructed by averaging measurements with unique sampling times from each season. Seasonal means are calculated because too few measurements exist to accurately determine monthly means. Measurements flagged by NOAA as non-background or erroneous are not included in the average. In order to lessen possible sampling biases, measurements taken before the beginning of the first full season and after the end of the last full season are not included. For example, although measurements at Barrow, AK began July 1988 and ended June 1993, seasonal means were calculated using output between September 1988

and May 1993. Seasonal means are available for as few as 7 seasons at Key Biscayne, FL to as many as 19 seasons at Barrow, AK and American Samoa. The number of complete seasons at each site (N) is listed in Table 5. In order to lessen sampling biases, seasonal means from the model are calculated by sampling the surface layer of the model at the same time the observations were taken.

The average seasonal means from measurements and model output are calculated by averaging seasonal means from each year. Residuals from the average seasonal mean are calculated by subtracting the average seasonal mean from the actual seasonal mean. A quadratic function is then fitted to each residual time series in order to determine the change in residuals during the N seasons. Annually averaged model-calculated and observation-calculated changes in CO residuals at each site are listed in Table 5. Residuals calculated from NOAA/CMDL measurements decrease at all locations but Key Biscayne. Model and observation-calculated 1991-1993 changes at Mace Head, Ireland; St. David's Head, Bermuda; and Key Biscayne, FL are nearly the same suggesting that transport alone is responsible for the summer 1991 to spring 1993 decrease in CO at these locations. In addition, model and observation-calculated residual time series at these three sites are highly correlated with $r^{\cdot} \approx 0.9$ at each location (see Table 5). Model-calculated CO concentrations also decrease at most SH locations; however, the magnitudes of decreases are much less than the magnitudes of observation-calculated decreases (see Table 5). Transport-induced variability is responsible for only a small

portion (or quite possibly none) of SH decreases. Changes in model-calculated CO concentrations at NOAA/CMDL sites are not caused by changes in the total amount of CO in the model. The global surface layer CO burden in the model varies by less than 1% per year between 1989 and 1993. Global trends in CO during the late 1980s and early 1990s are discussed in *Novelli et al.* [1994b] and *Khalil and Rasmussen* [1994].

In order to focus on interannual variability, the linear and quadratic trends were removed from each time series. This process removes CO variability due to "long-term trends" (i.e. changes in CO over the entire 7-19 season period) in sources, sinks and transport. Time series of detrended CO residuals at the selected NOAA/CMDL sites are shown in Figs. 10a-k. The correlation coefficient between model-calculated and NOAA/CMDL-calculated residuals (r), the percent of variance in NOAA/CMDL residuals explained by the model (r^2), and the significance of correlations at the 0.05 significance level are shown in Table 5.

The explained variance is also an estimate of the fraction of interannual variability that can be explained by transport. The estimate is accurate in locations where the GCTM is able to simulate day to day fluctuations in CO accurately but is likely to be low in regions where atmospheric variability is not captured. Transport-induced interannual variability explains more than 80% of total interannual variability at Mace Head, St. David's Head, and Key Biscayne. The model-calculation explains about 50% of variability in detrended NOAA/CMDL residuals at Ascension Island.

The importance of transport-induced variability at Ascension Island is somewhat surprising given the importance of biomass burning to its distribution. However, the amount of CO reaching Ascension Island is dependent on both the strength and location of biomass burning and atmospheric transport [*Fishman et al.*, 1991; *Novelli et al.*, 1992].

Residuals calculated from model output and measurements are negatively correlated at Christmas Island and uncorrelated at American Samoa, and Cape Kumukahi. The poor agreements are not necessarily evidence that interannual chemical variability dominates interannual transport variability at these locations. They may also indicate that meteorological variability is poorly captured at these locations.

Model-calculated and observation-calculated residuals at Guam and Cape Grim are correlated although the agreement is partly fortuitous since the magnitudes of model-calculated residuals are usually substantially smaller than the magnitudes of observation-calculated residuals. Transport appears to be responsible for about 30% of interannual variability at Seychelles although the correlation is not significant at the 0.05 significance level.

4.2 Upper tropospheric variability in GCTM

Upper tropospheric CO measurements are too scarce to evaluate interannual variability; however, processes responsible for upper tropospheric interannual variability in the GCTM can be identified.

The mean model-calculated CO distribution for October at 300

hPa is shown in Fig. 11a. The CO distribution has the most structure in the tropics where a combination of biomass burning, NMHC oxidation, and convection creates a CO peak over equatorial South America and Africa. Strong upper tropospheric winds advect a substantial portion of this CO as far east as Australia. The normalized standard deviation of 1989-1993 Octobers is shown in Fig. 11b.

Transport-induced interannual variability during October is largest in areas where the gradient of the CO distribution is largest. In these areas, small interannual changes in atmospheric circulation can lead to substantial changes in CO. Interannual variability at 300 hPa rarely exceeds 4% in the NH where horizontal CO gradients are small.

Upper tropospheric variability during October exceeds 10% to the north and east of Madagascar (15°S, 50°E) and off the western coast of South America (10°S, 80°W) [see Fig. 11b]. Most CO in the upper troposphere near Madagascar was originally emitted in eastern Africa and subsequently lofted by convection (Fig. 12c). Upper tropospheric 1993 CO concentrations to the northeast of Madagascar exceed 1990 concentrations by over 30 ppbv (Fig. 12d). The cause is strong off shore flow during 1993 (Fig. 12b) and weak off shore flow during 1990 (Fig. 12a). The situation is a bit more complicated off the western coast of South America. CO emissions are largest in eastern Brazil (Fig. 13c), but variability is largest in the eastern Pacific (Fig. 11b) where 1990 CO concentrations exceed 1993 amounts by up to 50 ppbv (Fig. 13d).

A strong anti-cyclone is located over South America during 1990 (Fig. 13a). Convectively lofted CO is transported around the high and into the Pacific where some CO is transported to the west and some to the south. The amount of CO incorporated into the upper tropospheric anticyclone is likely to be overestimated because tropical forcing is overestimated by the RAS convective algorithm [*Schubert et al.*, 1995; *Molod et al.*, 1996]. The strength of the southward component of the anti-cyclonic circulation is especially variable from year to year. CO concentrations off the western coast of South America are larger during 1990 because the anti-cyclonic circulation is much stronger in 1990 than 1993 (compare Figs. 11a and b). Direct transport of CO to the Atlantic is larger in 1993 when the upper tropospheric high is weaker.

5. SUMMARY

Transport-induced interannual variability of CO must be considered when calculating long-term trends of CO using data from only a few years and when evaluating the representativeness of satellite measurements taken over a few days. The fraction of interannual CO variability attributable to transport was estimated by comparing output from a GCTM calculation with a fixed annual cycle of sources and sinks to NOAA/CMDL measurements.

The latitudinal distribution of CO obtained by averaging model output at NOAA/CMDL sites was realistic during all seasons, although SH concentrations were typically 5-15 ppbv too high and NH

concentrations were 10-40 ppbv too low. Mean model-calculated CO concentrations at 500 hPa are within one standard deviation of 1994 MAPS measurements at nearly all latitudes during both April and October, although the magnitude of a SH peak due to biomass burning is underestimated.

Day to day fluctuations in trace species are well simulated by the GCTM at north Atlantic sites and these three sites are ideal for estimating the importance of transport to interannual variability. Transport-induced interannual variability explains 80-90% of total interannual variability at these sites. The estimation is less reliable at sites where day-to-day variations are not as well simulated; however, it appears that transport is responsible for more than 50% of interannual CO variability at Guam and Ascension Island. Transport-induced variability can explain a decrease in CO during 1991-1993 at Mace Head, Ireland and Bermuda and an increase in CO at Key Biscayne. Transport-induced variability is responsible for little (or possibly none) of the observed decrease in CO at SH locations.

Monthly mean model-calculated CO concentrations are most variable in regions where emissions vary strongly with location. October upper tropospheric variability is largest off the western coast of South America and off the eastern coast of Africa. The variability off the South American coast was traced to the strength of an upper tropospheric high while the variability off of Africa was traced to the strength of upper tropospheric off shore flow from Africa.

APPENDIX

Cumulus convection in the GCTM is parameterized using cumulus mass flux output from the RAS algorithm [*Moorthi and Suarez*, 1992; *Arakawa and Schubert*, 1974] used to parameterize convection in the GEOS-1 AGCM.

The conservation of mass principle is invoked in order to calculate the mixing ratio change due to convection. Consider layer k in Fig. A-1. From mass conservation it follows that the upward flux due to convection (C_k) is balanced by compensating large-scale subsidence (S_k). This circulation moves $\Delta t C_k q_c$ kgs of tracer upward and out of layer k and $\Delta t C_k q_{k-1}$ kgs of tracer downward and into layer k [Δt is the dynamic time step, q_c is the mixing ratio of tracer within the cloud (assumed to be constant), and q_k is the mixing ratio of tracer in layer k]. Similar arguments can be applied to calculate the mass flux at the lower edge of the layer. The mass of tracer in layer k after Δt is given by

$$M_k q_k^{n+1} = M_k q_k^{n} + \Delta t \{ C_{k+1} [q_c^{n+1} - q_k^{n+1}] - C_k [q_c^{n+1} - q_{k-1}^{n+1}] \} , \qquad (A1)$$

where $M_k = 100 \Delta p_k / g$ is the background air mass per unit area (kg/m^2), Δp_k is the depth of model layer k in hPa, and g is the gravitational acceleration in m/s^2. At the fixed cloud base (the top of layer NLAY-1), k=c and equation A1 reduces to

$$M_c q_c^{n+1} = M_c q_c^{n} - \Delta t C_c [q_c^{n+1} - q_{c-1}^{n+1}] . \qquad (A2)$$

The equations for each model layer from cloud base to cloud top form a coupled linear system that is similar to a discretized flux form transport equation for a time implicit differencing scheme. In the limit $\Delta t \longrightarrow 0$ and $\Delta p \longrightarrow 0$ (i.e., the continuous case), the cloud transport equation becomes

$$\frac{\partial q}{\partial t} = \frac{q}{100} \frac{\partial}{\partial p} C(q_c - q) \qquad (A3)$$

This equation is analogous to Schneider and Lindzen's equation [*Schneider and Lindzen*, 1976] for computing the "apparent momentum source" due to cloud motions. The equations for each layer (A1) form a coupled linear system that is solved iteratively using a time step of $\Delta t/ns$, where ns is the number of iterations. The equations can be written in a discretized form as

$$M_k q_k^{n+1/ns} = M_k q_k^n + \frac{\Delta t}{ns} \{ C_{k+1} [q_c^{n+1/ns} - q_k^n] - C_k [q_c^{n+1/ns} - q_{k-1}^n] \} \quad (A4),$$

where the intermediate cloud mixing ratio $q_c^{n+1/ns}$ is obtained by directly solving A2 after replacing q_{c-1}^{n+1} with q_{c-1}^n.

$$q_c^{n+1/ns} = [M_c q_c^n + \Delta t C_c q_{c-1}^n / ns] / (M_c + \Delta t C_c / ns) \qquad (A5)$$

Equations A4 and A5 are integrated from the cloud base to the cloud top ns times in order to obtain a more accurate solution. In practice, ns=3 which results in a cumulus transport step of 4 minutes for $\Delta t = 12$ minutes.

References

Allen D. J., The effects of transport and convection on the global distribution of trace species as determined by a chemistry and transport model, Ph.D. thesis, University of Maryland, In preparation, 1996a.

Allen, D. J., R. B. Rood, A. M. Thompson, and R. D. Hudson, Three-dimensional Rn-222 calculations using assimilated meteorological data and a convective mixing algorithm, *J. Geophys. Res.*, In press, 1996b.

Andreae, M. O., Biomass burning: Its history, use, and distribution, and its impact on environmental quality and global climate, In: *Proceedings from the Chapman Conference on Global Biomass Burning: Atmospheric, Climatic, and Biospheric Implications*, 19-23 March, Williamsburg, Virginia, J. Levine, ed., MIT Press, 3-21, 1991.

Andreae, M. O. et al., Biomass-burning emissions and associated haze layers over Amazonia, *J. Geophys. Res.*, 93, 1509-1527, 1988.

Arakawa, A. and W. H. Schubert, Interaction of a cumulus cloud ensemble with the large-scale environment, Part I, *J. Atmos. Sci.* 31, 674-701,1974.

Bates, T. S., K. C. Kelly, J. E. Johnson, and R. H. Gammon, Regional and seasonal variations in the flux of oceanic carbon monoxide to the atmosphere, *J. Geophys. Res.*, 100, 23093-23101, 1995.

Benkovitz, C. M., M. T. Scholtz, J. Pacyna, L. Tarrason, J. Dignon, E. C. Voldner, P. A. Spiro, J. A. Logan, and T. E. Graedel, Global gridded inventories of anthropogenic emissions of sulfur and nitrogen, *J. Geophys. Res.*, In press, 1996.

Buhr, M. P., M. Trainer, D. D. Parrish, R. E. Sievers, and F. C. Fehsenfeld, Assessment of pollutant emission inventories by principal component analysis of ambient air measurements, *Geophys. Res. Lett.*, 19, 1009-1012, 1992.

Chameides, W. L., The photochemical role of tropospheric nitrogen oxides, *Geophys. Res. Lett.*, 5, 17-20, 1978.

Crutzen, P. J., A discussion of the chemistry of some minor constituents in the stratosphere and troposphere, *Pure Appl. Geophys.*, 106-108, 1385-1399, 1973.

Crutzen, P. J. and M. O. Andreae, Biomass burning in the tropics: Impact on atmospheric chemistry and biogeochemical cycles, *Science,*

50, 1669-1679, 1990.

DeMore, W. B., D. M. Golden, R. F. Hampson, C. J. Howard, C. E. Kolb, M. J. Kurylo, M. J. Molina, A. R. Ravishankara, and S. P. Sander, Chemical kinetics and photochemical data for use in stratospheric modeling, *JPL Publ. 94-26*. Jet Propul. Lab., Pasadena, Calif., 1994.

Doddridge, B. G., R. R. Dickerson, T. G. Spain, S. J. Oltmans, and P. C. Novelli, Carbon monoxide measurements at Mace Head, Ireland, In: Ozone in the Troposphere and Stratosphere, *Proceedings of the Quadrennial Ozone Symposium 1992*, R. D. Hudson, ed., NASA Conf. Pub. 3266, pp. 134-137, 1994a.

Doddridge, B. G., P. A. Dirmeyer, J. T. Merrill, S. J. Oltmans, and R. R. Dickerson, Interannual variability over the eastern North Atlantic Ocean: Chemical and meteorological evidence for tropical influence on regional-scale transport in the extratropics, *J. Geophys. Res.*, 99, 22923-22935, 1994b.

Drummond, J. R., Measurements of pollution in the troposphere (MOPITT), In: *The use of EOS to study atmospheric physics*, J. Gille and G. Visconti (ed.), North Holland, 1991.

EPA (Environmental Protection Agency), *National air pollution emission trends*, 1900-1992, EPA-454/R-93-032, 1993.

Fishman, J., K. Fakhruzzaman, B. Cros, and D. Nganga, Identification of widespread pollution in the southern hemisphere deduced from satellite analysis, *Science*, 252, 1693-1696, 1991.

Hao, W. M., M.-H. Liu, and P. J. Crutzen, Estimates of annual and regional releases of CO_2 and other trace gases to the atmosphere from fires in the tropics, based on the FAO statistics for the period 1975-1980, In: *Fire in the Tropical Biota: Ecosystem Processes and Global Challenges*, J. G. Goldammer, ed., Springer-Verlag Berlin Heidelberg, 440-460, 1990.

Harriss, R. C., G. W. Sachse, G. F. Hill, L. Wade, K. B. Bartlett, J. E. Collins, L. P. Steele, P. C. Novelli, Carbon monoxide and methane in the North American arctic and subarctic troposphere; July-August 1988, *J. Geophys. Res.*, 97, 16589-16599, 1992.

Hurst, D. F., D. W. Griffith, G. D. Cook, Trace gas emissions from biomass burning in tropical Australian savannas, *J. Geophys. Res.*, 99, 16441-16456, 1994.

Jennings. S. G., F. M. McGovern, and W. F. Cooke, Carbon mass concentration measurements at Mace Head, on the west coast of Ireland, *Atmos. Environ.*, 27A, 1229-1239, 1993.

Jennings, S. G., C. D. O'Dowd, T. C. O'Connor, and F. M. McGovern,

Physical characteristics of the ambient aerosol at Mace Head, Atmos. Environ., 25A, 557-562, 1991.

Jennings, S. G., T. G. Spain, B. G. Doddridge, B. P. Kelly, J. T. Merrill, A. D. A. Hansen, and H. Maring, Concurrent measurements of black carbon aerosol and carbon monoxide at Mace Head, on the west coast of Ireland, J. Geophys. Res., submitted, 1995.

Khalil, M. A. K. and R. A. Rasmussen, Carbon monoxide in the earth's atmosphere: indications of a global increase, Nature, 332, 242-245, 1988.

Khalil, M. A. K. and R. A. Rasmussen, Global decrease in atmospheric carbon monoxide concentration, Nature, 370, 639-641, 1994.

Kirchhoff, V. W., A. W. Setzer, and M. C. Pereira, Biomass burning in Amazonia: Seasonal effects on atmospheric O_3 and CO, Geophys. Res. Lett.,16, 469-472, 1989.

Lin, S.-J., W. C. Chao, Y. C. Sud, and G. K. Walker, A class of the van Leer-type transport schemes and its applications to the moisture transport in a general circulation model, Mon. Wea. Rev., 122, 1575-1593, 1994.

Lin, S.-J. and R. B. Rood, Multidimensional flux form semi-Lagrangian transport schemes, Mon. Wea. Rev., submitted, 1995.

Logan, J. A., M. J. Prather, S. C. Wofsy, and M. B. McElroy, Tropospheric chemistry: A global perspective, J. Geophys. Res., 86, 7210-7254, 1981.

Lonneman, W. A., R. L. Seila, and S. A. Meeks, Non-methane organic composition in the Lincoln tunnel, Environ. Sci. Technol., 20, 790-796, 1986.

Miyoshi, A., S. Hatakeyama, and N. Washida, OH radical-initiated photooxidation of isoprene: An estimate of global CO production, J. Geophys. Res., 99, 18779-18787, 1994.

Molod, A., H. M. Helfand, and L. L. Takacs, The climatology of parameterized physical processes in the GEOS-1 GCTM and their impact on the GEOS-1 data assimilation system, J. of Climate, In press, 1996.

Moorthi S. and M. J. Suarez, Relaxed Arakawa-Schubert: A parameterization of moist convection for general circulation models, Mon. Wea. Rev., 120, 978-1002, 1992.

Muller, J.-F. and G. Brasseur, IMAGES: A three-dimensional chemical model of the global troposphere, J. Geophys. Res., 100, 16445-16490, 1995.

Novelli, P. C., J. E. Collins, Jr., R. C. Myers, G. W. Sachse, and H. E. Scheel, Reevaluation of the NOAA/CMDL carbon monoxide reference scale and comparisons with CO reference gases at NASA-Langley and the Fraunhofer Institute, *J. Geophys. Res.*, 99, 12833-12839, 1994a.

Novelli, P. C., J. W. Elkins, and L. P. Steele, The development and evaluation of a gravimetric reference scale for measurements of atmospheric carbon monoxide, *J. Geophys. Res.*, 96, 13109-13121, 1991.

Novelli, P. C., K. A. Masarie. P. P. Tans, and P. M. Lang, Recent changes in atmospheric carbon monoxide, *Science*, 263, 1587-1590, 1994b.

Novelli, P. C., L. P. Steele, and P. P. Tans, Mixing ratios of carbon monoxide in the troposphere, *J. Geophys. Res.*, 97, 20731-20750, 1992.

Pacyna, J. M. and T. E. Graedel, Atmospheric emissions inventories: Status and prospects, *Annu. Rev. Energy Environ.*, 20, 265-300, 1995.

Pickering, K. E., J. R. Scala, A. M. Thompson, W.-K. Tao, and J. Simpson, A regional estimate of convective transport of CO from biomass burning, *Geophys. Res. Lett.*, 19, 289-292, 1992.

Pickering, K. E., A. M. Thompson, Y. Wang, W.-K. Tao, D. P. McNamara, V. W. Kirchhoff, B. G. Heikes, G. W. Sachse, J. D. Bradshaw, G. L. Gregory, and D. R. Blake, Convective transport of biomass burning emissions over Brazil during TRACE-A, *J. Geophys. Res.*, submitted, 1995.

Pierson, W. R., A. W. Gertler, and R. L. Bradow, Comparison of the SCAQS tunnel study with other on-road vehicle emission data, *J. Air Waste Manage. Assoc.*, 40, 1495-1504, 1990.

Pinto, J. H., Y. L. Yung, D. Rind, G. L. Russell, J. A. Lerner, J. E. Hansen, and S. Hameed, A general circulation model study of atmospheric carbon monoxide, *J. Geophys. Res.*, 88, 3691-3702, 1983.

Prinn, R. G., R. F. Weiss, B. R. Miller, J. Huang, F. N. Alyea, D. M. Cunnold, P. J. Fraser, D. E. Hartley, and P. G. Simmonds, Atmospheric trends and lifetime of CH_3CCl_3 and global OH concentrations, *Science*, 269, 187-192, 1995.

Prospero, J. M., D. L. Savoie, R. Arimoto, H. Olafsson, and H. Hjartarson, Sources of aerosol nitrate and non-sea-salt sulfate in the Iceland region, *Sci. Total Environ.*, 160/161, 181-191, 1995.

Reichle, H. G., Jr., V. S. Connors, J. A. Holland, W. D. Hypes, H. A. Wallio, J. C. Casas, B. B. Gormsen, M. A. Saylor, and W. D.

Hesketh, Middle and upper tropospheric carbon monoxide ratios as measured by a satellite-borne remote sensor during November 1981, *J. Geophys. Res.*, 91, 10865-10887, 1986.

Reichle, H. G., Jr., V. S. Connors, J. A. Holland, R. T. Sherrill, H. A. Wallio, J. C. Casas, E. P. Condon, B. B. Gormsen, and W. Seiler, The distribution of middle tropospheric carbon monoxide during early October 1984, *J. Geophys. Res.*, 95, 9842-9856, 1990.

Richardson, J.L., An investigation of large-scale tropical biomass burning and the impact of its emissions on atmospheric composition, Ph.D. thesis, Georgia Institute of Technology, 168 pp., 1994.

Schneider, E. K. and R. S. Lindzen, A discussion of the parameterization of momentum exchange by cumulus convection, *J. Geophys. Res.*, 81, 3158-3160, 1976.

Scholes, R. J., D. Ward, and C. O. Justice, Emissions of trace gases and aerosol particles due to vegetation burning in southern-hemisphere Africa, *J. Geophy. Res.*, submitted, 1995.

Schubert, S. D., R. B. Rood, and J. Pfaendtner, An assimilated data set for earth science applications, *Bull. Amer. Meteor. Soc.*, 74, 2331-2342, 1993.

Schubert, S. D., C.-J. Park, C.-Y. Wu, W. Higgins, Y. Kondratyeva, A. Molod, L. Takacs, M. Seablom, and R. B. Rood, A multi-year assimilation with the GEOS-1 system: Overview and results, *NASA Tech. Memo.* 104606, 6, 1995.

Seiler, W. and R. Conrad, Contributions of tropical ecosystems to the global budgets of trace gases especially CH_4, H_2, CO, and N_2O. In *"Geophysiology of Amazonia"* (R. Dickinson, ed.) pp. 133-162, Wiley, New York, 1987.

Shipham, M. C., A. S. Bachmeier, D. R. Cahoon, Jr., and E. V. Browell, Meteorological overview of the Arctic Boundary Layer Experiment (ABLE 3A) Flight Series, *J. Geophys. Res.*, 97, 16395-16419, 1992.

Spivakovsky, C. M., R. Yevich, J. A. Logan, S. C. Wofsy, and M. B. McElroy, Tropospheric OH in a three-dimensional chemical tracer model: An assessment based on observations of CH_3CCl_3, *J. Geophys. Res.*, 95, 18441-18471, 1990.

Steele, L. P., P. J. Fraser, R. A. Rasmussen, M. A. K. Khalil, T. J. Conway, A. J. Crawford, R. H. Gammon, K. A. Masarie, and K. W. Thoning, The global distribution of methane in the troposphere, *J. Atmos. Chem.*, 5, 125-171, 1987.

Sze, N. D., Anthropogenic CO emissions: Implications for the

atmospheric CO-OH-CH$_4$ cycle, *Science*, 195, 673-675, 1977.

Takacs, L. L., A. Molod, and T. Wang, Documentation of the Goddard Earth Observing System (GEOS) General Circulation Model-Version 1. *NASA Tech. Memo.* No. 104606, volume 1, Goddard Space Flight Center, Greenbelt, MD 20771, 1994.

Thompson, A. M., K. E. Pickering, R. R. Dickerson, W. G. Ellis, Jr., D. J. Jacob, J. R. Scala, W.-K. Tao, D. P. McNamara, and J. Simpson, Convective transport over the central United States and its role in regional CO and ozone budgets, *J. Geophys. Res.*, 99, 18703-18711, 1994.

Watson, C. E., J. Fishman, and H. G. Reichle, Jr., The significance of biomass burning as a source of carbon monoxide and ozone in southern hemisphere tropics: A satellite analysis, *J. Geophys. Res.*, 95, 16443-16450, 1990.

Wofsy, S. C., G. W. Sachse, G. L. Gregory, D. R. Blake, J. D. Bradshaw, S. T. Sandholm, H. B. Singh, J. A. Barrick, R. C. Harriss, R. W. Talbot, M. A. Shipham, E. V. Browell, D. J. Jacob, and J. A. Logan, Atmospheric chemistry in the Arctic and Subarctic: Influence of natural fires, industrial emissions, and stratospheric input, *J. Geophys. Res.*, 97, 16731-16746, 1992.

WMO, *Scientific assessment of stratospheric ozone: 1991*, World Meteorological Organization Global Ozone Research and Monitoring Project-Report 25, Geneva, 1992.

Figure captions

1. Annually averaged model-calculated CO source (Tg / yr) due to (a) fossil fuel combustion, (b) oxidation of NMHCs, and (c) biomass burning. Shaded region shows where source is greater than 0.5 Tg / yr. Hatched region shows where source is greater than 2 Tg / yr.

2. CO (ppbv) as a function of latitude from NOAA/CMDL measurements (solid lines) and model output in lowest sigma layer [≈994 hPa] (dashed lines) for (a) December-February, (b) March-May, (c) June-August, and (d) September-November.

3. MAPS CO [Shaded range shows mean (solid line) ± 1σ] and 500 hPa model-calculated CO (dashed line) as a function of latitude for a) April and b) October. MAPS data are composite picture for April 9-19, 1994 and September 30-October 11, 1994, respectively. Model fields are 1989-1993 means for April and October. Units are ppbv.

4. Mean CO (ppbv) as a function of longitude and latitude from model at 500 hPa for (a) April 1989-1993 and for (b) October 1989-1993.

5. Mean 1989-1993 model CO at 500 hPa (ppbv) during October due to (a) fossil fuel combustion, (b) oxidation of NMHCs, (c) biomass burning, and (d) oxidation of CH_4. Contour intervals of 5 ppbv for a, 10 ppbv for b-c, and 1 ppbv for d.

6. a) Mean 1989-1993 model CO (ppbv) for October in boundary layer. Contour interval of 10 ppbv for [CO] less than 100 ppbv, 20 ppbv for [CO] between 100 and 200 ppbv, and 50 ppbv for [CO] greater than 200 ppbv. b) Normalized CO standard deviation from model for October (i.e. the standard deviation of 1989-1993 October residuals divided by the October mean). Contour interval of 3 percent.

7. Model grid point containing AEROCE and NOAA/CMDL measuring sites discussed in this paper. Note: Locations are approximate. See Table 3 for actual latitudes and longitudes of sites.

8. CO timeseries (ppbv) for a) September 1992 through September 1993 at Heimaey, Iceland and for b) August 1991 through December 1993 at Mace Head, Ireland. Measurements are shown with asterisks. Model-calculated surface layer CO at nearest grid point is shown with dashed lines.

9. Monthly averaged CO (ppbv) for 1989-1993 at a) Barrow, Alaska; b) Mace Head, Ireland c) St. David's Head, Bermuda; d) Key Biscayne, FL; e) Cape Kumukahi, HW; f) Guam, Mariana Islands; g) Christmas Island; h) Mahe Island, Seychelles; i) Ascension Island; j) Tutuila, American Samoa; and k) Cape Grim, Tasmania. CMDL measurements are shown with solid lines. Model-calculated surface

layer CO at nearest grid point is shown with dashed lines.

10. Interannual fluctuations in monthly mean CO (ppbv) after removing mean and trend over measurement period at a) Barrow, Alaska; b) Mace Head, Ireland; c) St. David's Head, Bermuda; d) Key Biscayne, FL; e) Cape Kumukahi, HW; f) Guam, Mariana Islands; g) Christmas Island; h) Mahe Island, Seychelles; i) Ascension Island; j) Tutuila, American Samoa; and k) Cape Grim, Tasmania. Residual calculated from data (model output) is shown with a solid (dashed) line.

11. a) Mean 1989-1993 model CO (ppbv) for October at 300 hPa, Contour interval of 10 ppbv. b) Normalized CO standard deviation from model for October (i.e. the standard deviation of 1989-1993 October residuals divided by the October mean). Contour interval of 3 percent.

12. For October in southern Africa: a) 300 hPa wind vectors (m/s) for 1990, b) 300 hPa wind vectors (m/s) for 1993, c) CO source (Tgs) due to fossil fuel combustion, oxidation of NMHC's, and biomass burning, and d) Difference (ppbv) between 1993 and 1990 CO at 300 hPa. Contour interval of 0.25 Tgs for c and 10 ppbv for d.

13. For October in northern South America: a) 300 hPa wind vectors (m/s) for 1990, b) 300 hPa wind vectors (m/s) for 1993, c) CO source (Tgs) due to fossil fuel combustion, oxidation of NMHC's, and biomass burning, and d) Difference (ppbv) between 1990 and 1993 CO at 300 hPa. Contour interval of 0.25 Tgs for c and 10 ppbv for d.

A1. Schematic of algorithm used to calculate mixing by moist convective processes in column with NLAY layers. Mass flux at edge of layers (C_k), mixing ratio at layer centers (q_k), mass flux due to subsidence (S_k), and mass flux at cloud base (C_c) are shown.

Table 1

Latitude	CH_4 Mixing Ratio[*]
90°N	1.90 ppbv
80°N	1.89 ppbv
70°N	1.88 ppbv
60°N	1.87 ppbv
50°N	1.87 ppbv
40°N	1.86 ppbv
30°N	1.85 ppbv
20°N	1.83 ppbv
10°N	1.79 ppbv
0°N	1.78 ppbv
10°S	1.76 ppbv
20°S	1.75 ppbv
30°S	1.75 ppbv
90°S to 30°S	1.74 ppbv

[*] CH_4 is assumed to be constant in height and longitude.

Table 2

Annual CO emissions in Tg / yr

	GCTM[1]	LPWM[2]	SC[3]	PG[4]
Technological sources (Fossil fuel combustion)	329	450	640±200	440±150
Natural NMHC oxidation	618	560	900±500	800±400
Biomass burning	370	655	1000±600	700±200
Methane oxidation	722	810	600±300	600±200
Ocean[5]	---	40	100± 90	50±40
Vegetation	---	130	75±25	75±25
Oxidation of anthropogenic HCs	---	90	---	---
Total	2039	2735	3315±1700	2700±1000

[1]Model-calculated source for model year 1989

[2]Estimate by *Logan et al.* [1981]

[3]Estimate by *Seiler and Conrad* [1987]

[4]Estimate by *Pacyna and Graedel* [1995]

[5]Oceanic emission estimated to be 13 Tg/yr with an uncertainty of a factor of two by *Bates et al.* [1995].

Table 3

CO monitoring stations discussed in paper

Site	Lat	Lon	Ht	1st CMDL obs
Barrow, Alaska*	71°N	157°W	11m	07/25/88
Heimaey, Iceland*	63°N	20°W	100m	11/16/91
Mace Head, Ireland*§	53°N	10°W	25m	06/03/91
Niwot Ridge, Colorado*	40°N	106°W	3475m	12/14/88
Tae-ahn Peninsula*	37°N	126°E	20m	01/05/91
Qinghai Province*	36°N	101°E	3810m	08/05/90
St. David's Head, Bermuda*	32°N	65°W	30m	06/11/91
Key Biscayne, Florida*	26°N	80°W	3m	08/09/91
Cape Kumukahi, Hawaii*	20°N	155°W	3m	07/04/89
Guam, Mariana Islands*	13°N	145°E	2m	10/10/89
Christmas Island*	02°N	157°W	3m	12/25/89
Mahe Island, Seychelles*	04°S	55°E	3m	11/16/90
Ascension Island*	08°S	14°W	54m	02/02/89
Tutuila, American Samoa*	14°S	171°W	42m	09/23/88
Cape Grim, Tasmania*	41°S	145°E	94m	06/14/91

*Sampling site included in latitudinal average (Fig. 2)

§Mace Head: AEROCE data are used for Fig. 7. NOAA/CMDL data are used for remainder of study.

%Heimaey: AEROCE data are used for Fig. 7, although NOAA/CMDL measurements began November 16, 1991.

Table 4

Mace Head, Ireland CO for fall 1991 and fall 1992

	1991		1992	
	Measurements	Model	Measurements	Model
Minimum	65	78	68	71
25th Percentile	118	99	101	93
Median	127	114	111	103
75th Percentile	157	145	122	112
Maximum	447	474	193	193
Mean	156	140	114	106
±one sigma	64	71	18	21

Table 5

Residual information

	N	r	r^2	.05	Trend CMDL	Model	r^*
Barrow, AK	19	.59	.35	yes	-3.3	+0.1	.27
Macehead, Ireland	8	.90	.81	no	-2.8	-3.1	.86
Bermuda	8	.92	.85	no	-3.5	-4.2	.91
Key Biscayne, FL	7	.97	.94	no	+6.2	+4.6	.91
Cape Kumukahi, HW	15	-.01	xx	no	-3.5	+0.3	.02
Guam, Mariana Isl.	14	.83	.68	yes	-4.1	-0.7	.66
Christmas Island	14	-.50	xx	no	-0.8	-1.6	-.49
Mahe Isl., Seychelles	10	.57	.32	no	-2.7	-0.5	.66
Ascension Island	17	.72	.52	yes	-2.4	+0.4	.48
American Samoa	19	-.11	xx	no	-3.7	-0.7	.25
Cape Grim	8	.55	.31	no	-6.7	-0.4	.03

N: Seasons where measurements are available throughout
    19: fall   1988 to spring 1993
    15: fall   1989 to spring 1993
    11: fall   1990 to spring 1993
     7: fall   1991 to spring 1993

r (r^*) Linear correlation coefficient between model-calculated and measured time series after (before) removing linear and quadratic trends

r^2:   Variance explained by linear correlation

.05:   Significance calculated using t test with N-8 degrees of freedom

Trend: Mean percent change per year in residuals calculated from NOAA/CMDL measurements (CMDL) and model output (Model). Percent change is calculated using fields from N seasons.

CO source due to fossil fuels
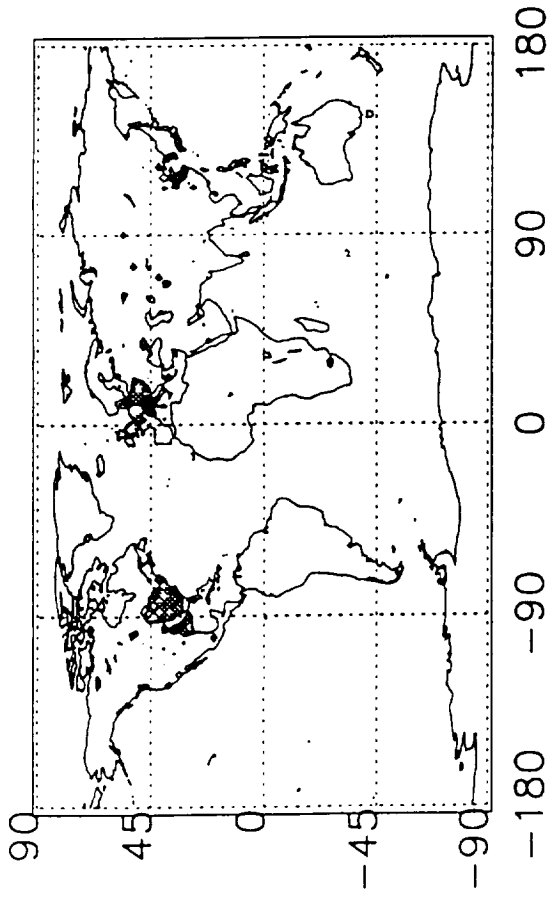
CO source due to NMHCs

CO source due to burning

1a-c

2a-d

April CO as a function of latitude

MAPS data (——)
Model at 500 hPa (— — —)

October CO as a function of latitude

MAPS data (——)
Model at 500 hPa (— — —)

3a+b
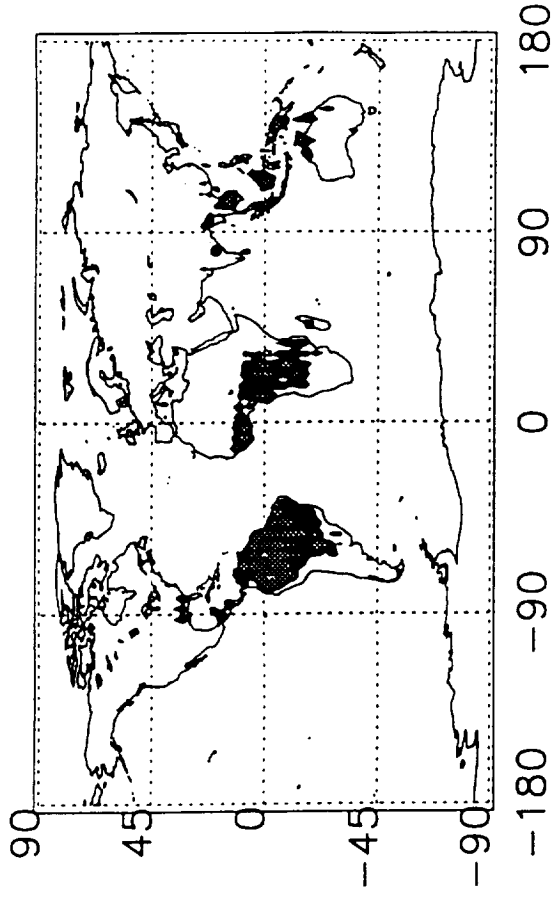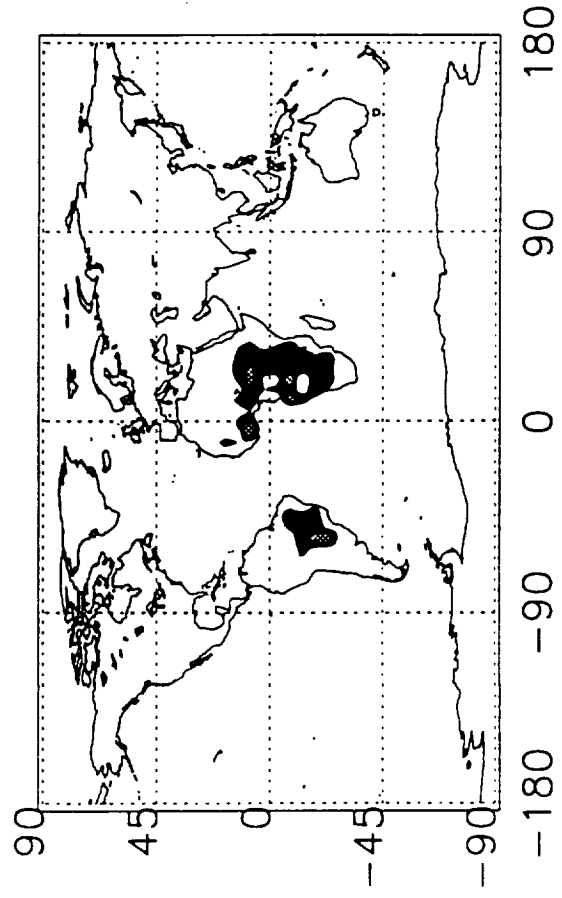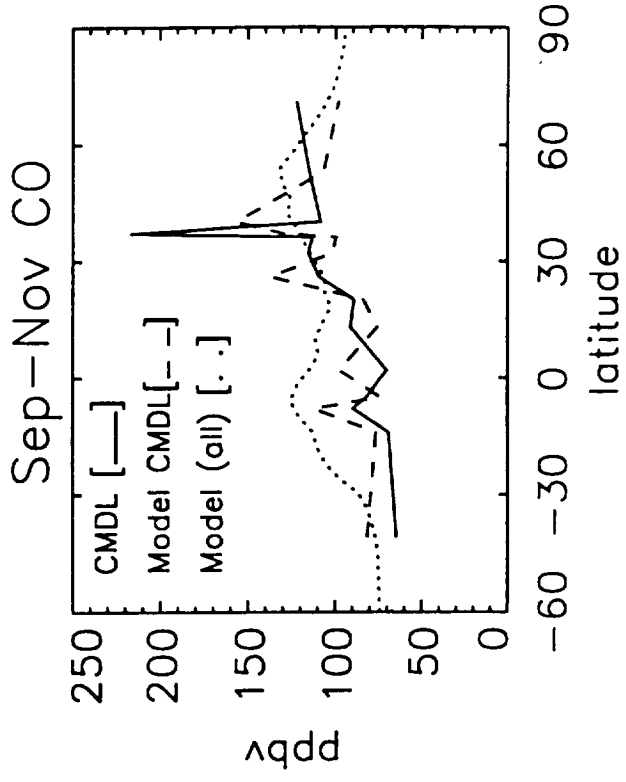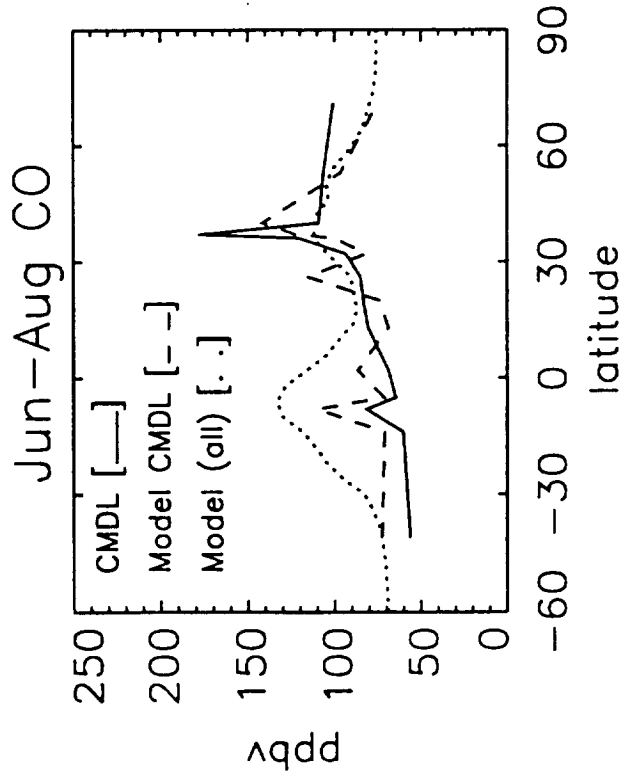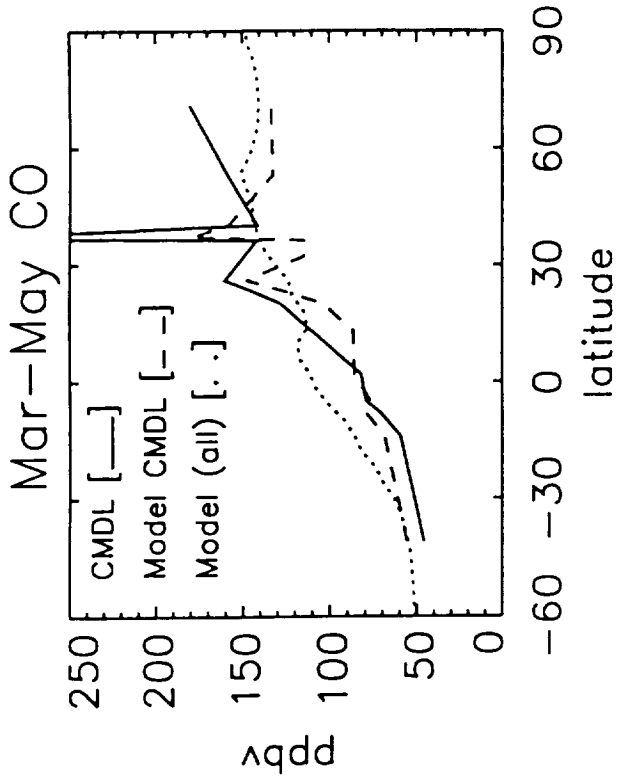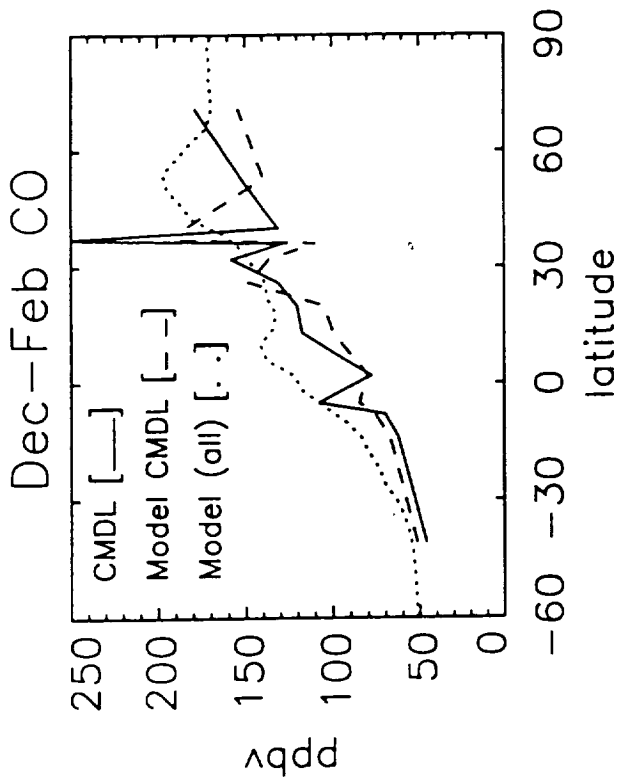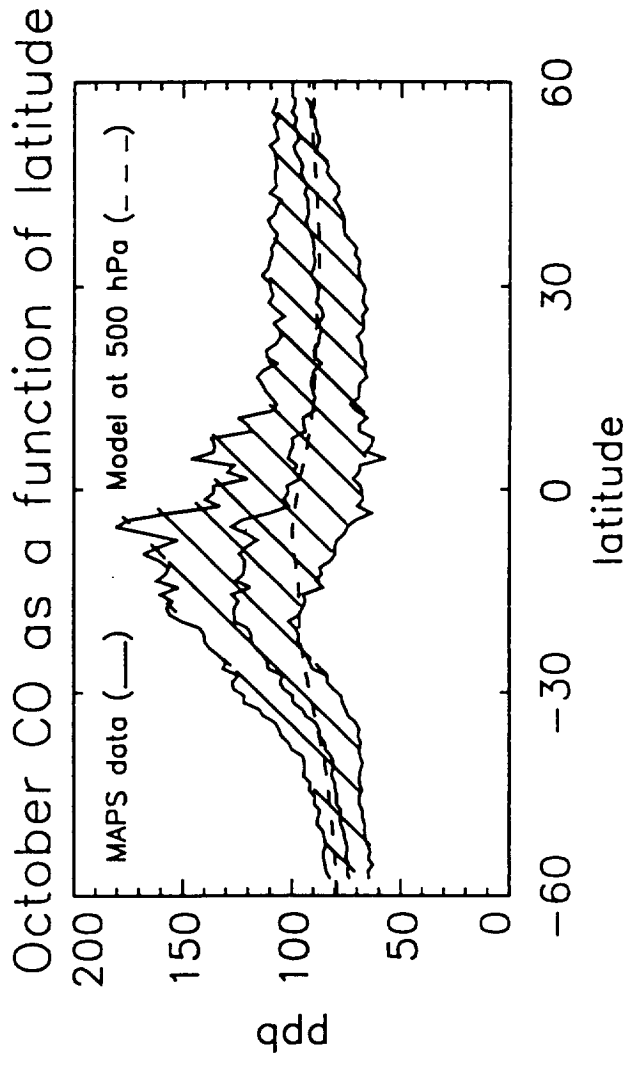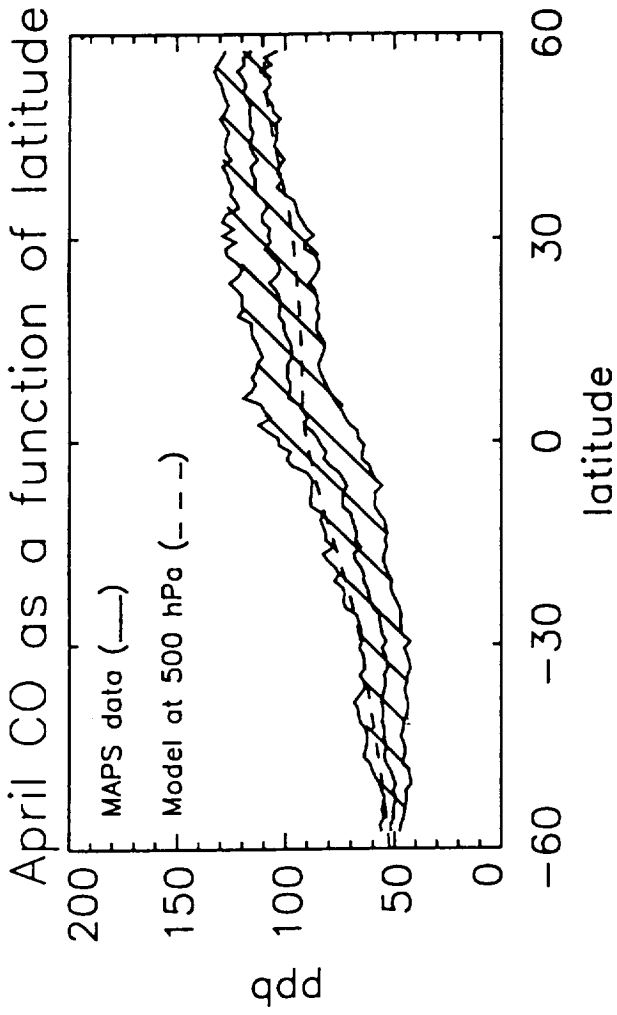
Mean 500 hPa CO during April
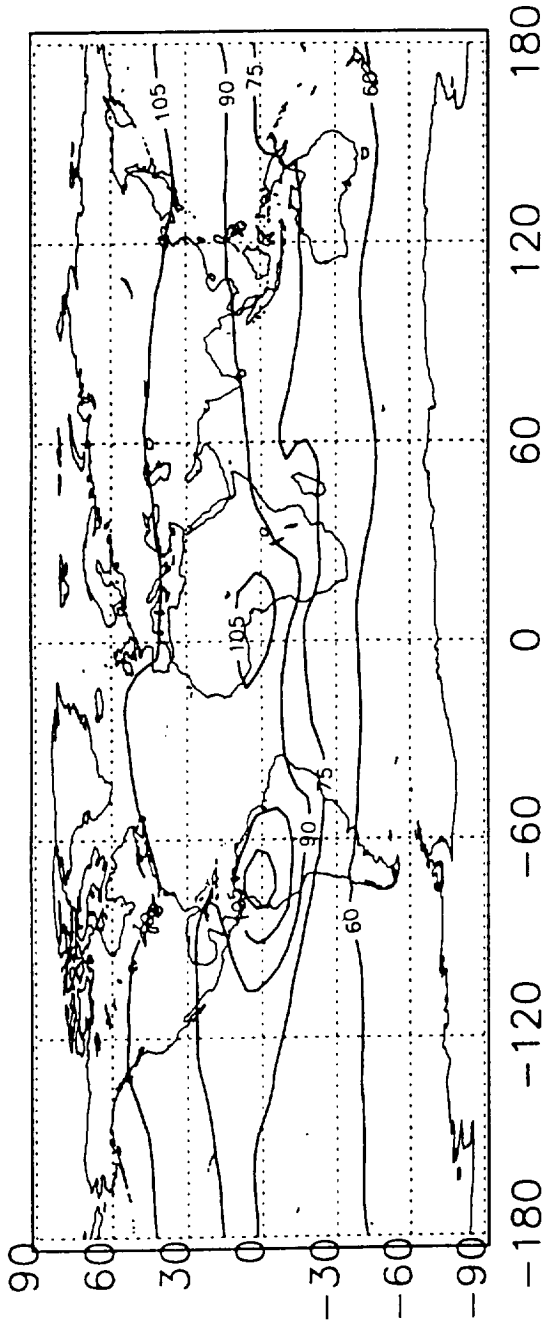
Mean 500 hPa CO during October

4 a - b
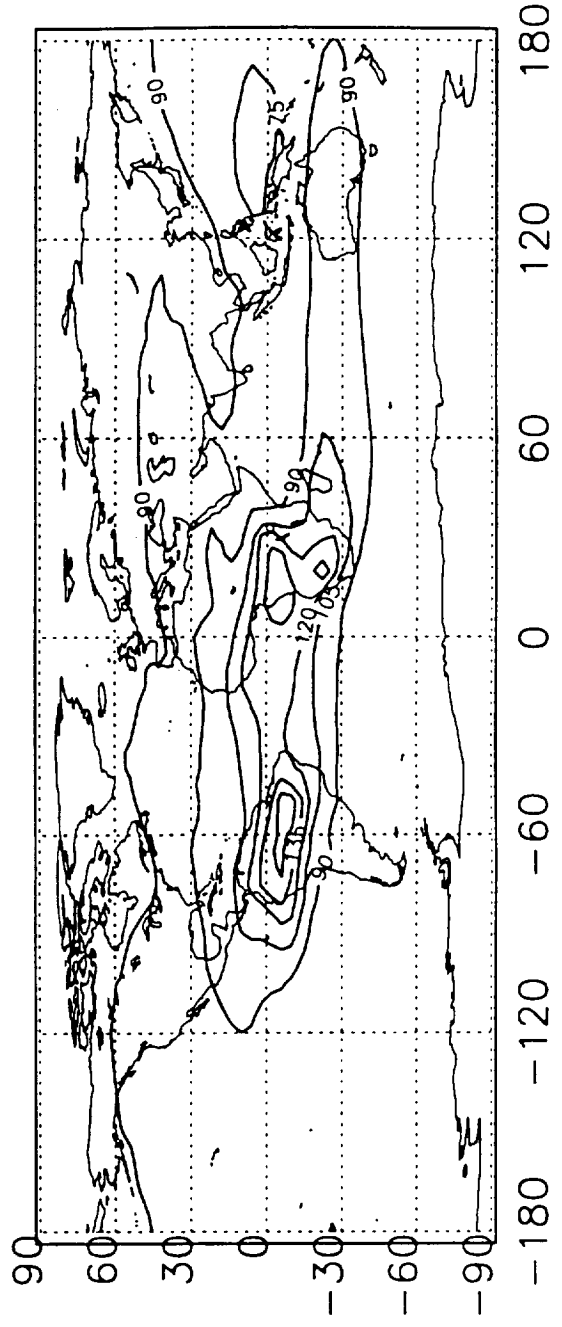
Oct CO (fossil fuels) at 500 hPa
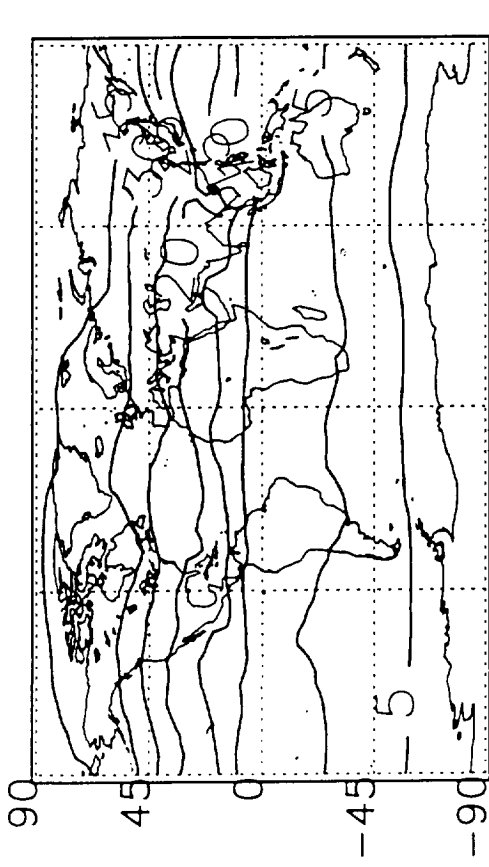
Oct CO (NMHC oxidation) at 500 hPa
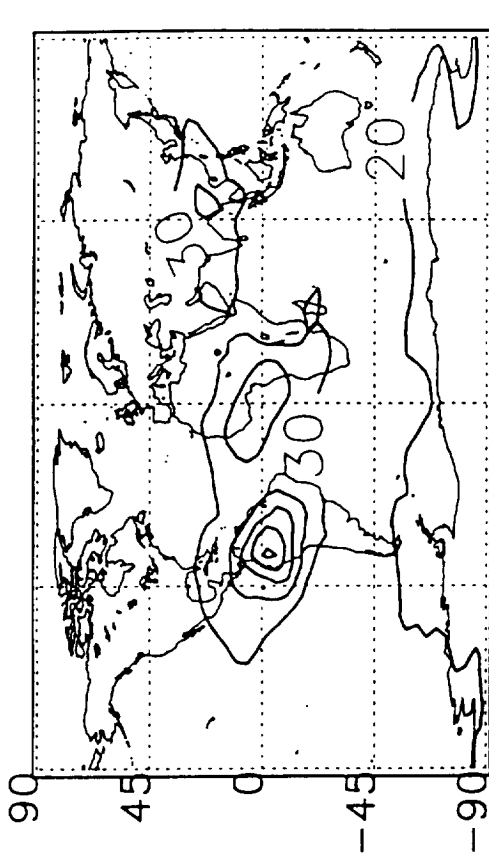
Oct CO (biomass burning) at 500 hPa
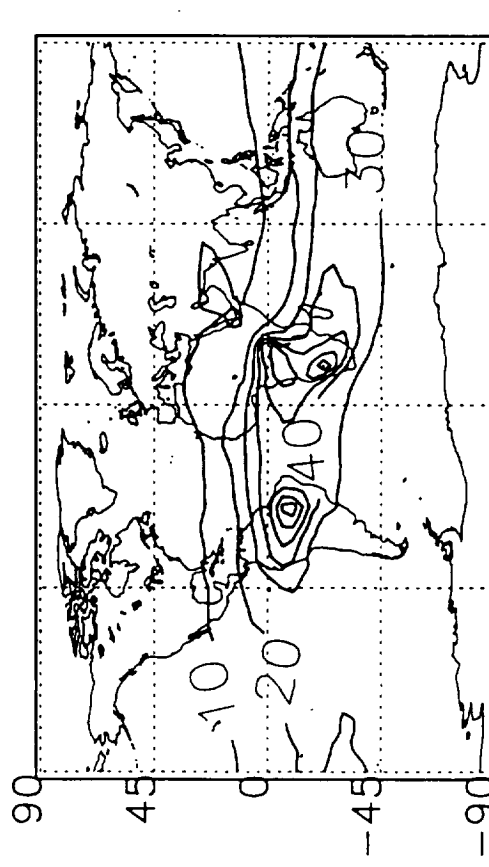
Oct CO (CH4 oxidation) at 500 hPa
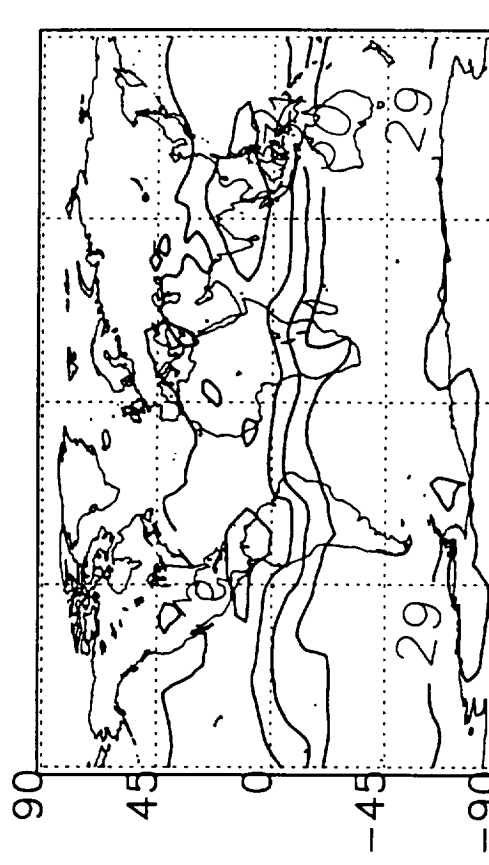
Mean CO in surface layer during October
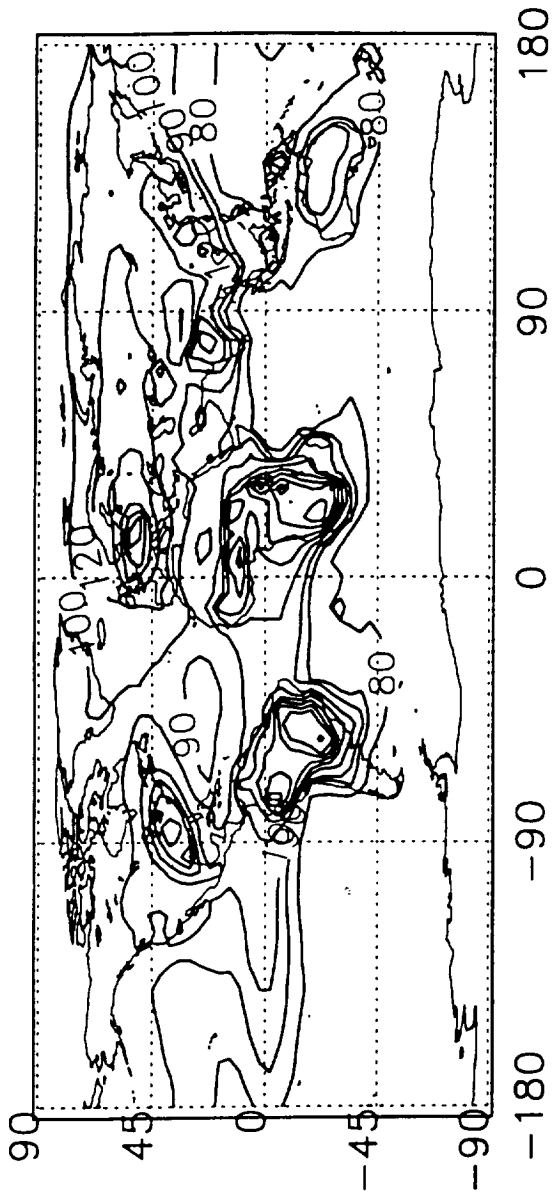
Variability in boundary layer during October

6a-b

CO at Heimaey, Iceland

Model (———)

Measurements (*)

CO at Mace Head, Ireland

Model (———)

Measurements (*)
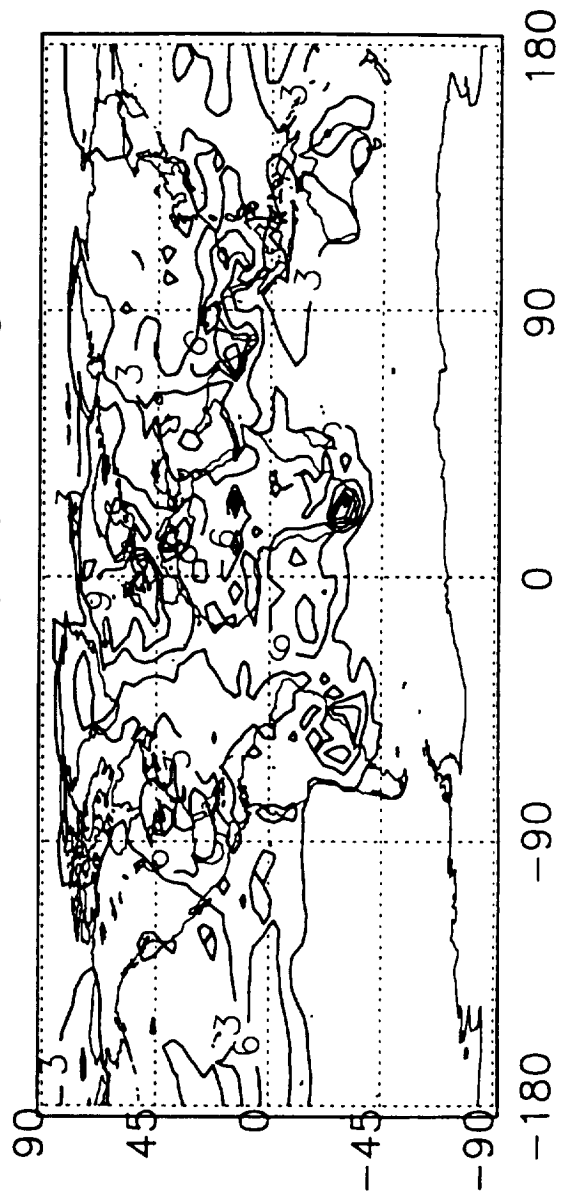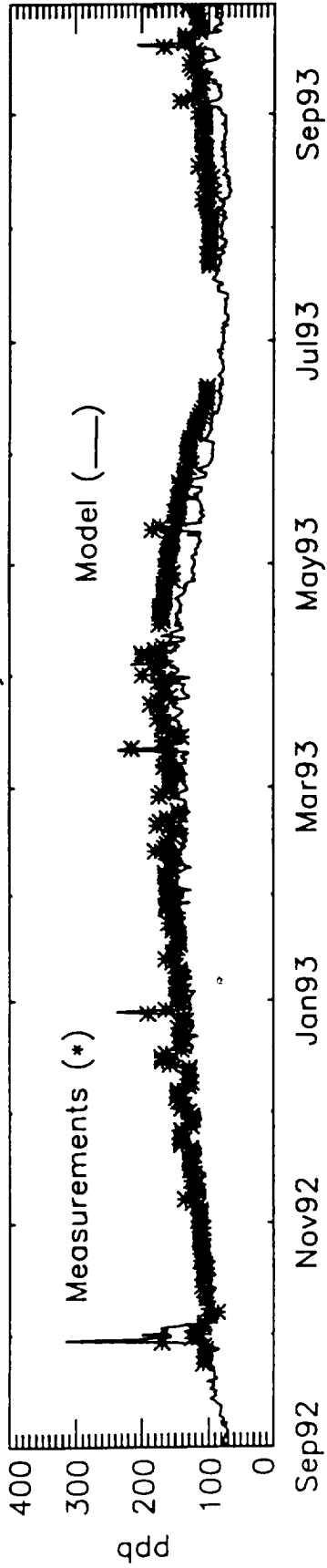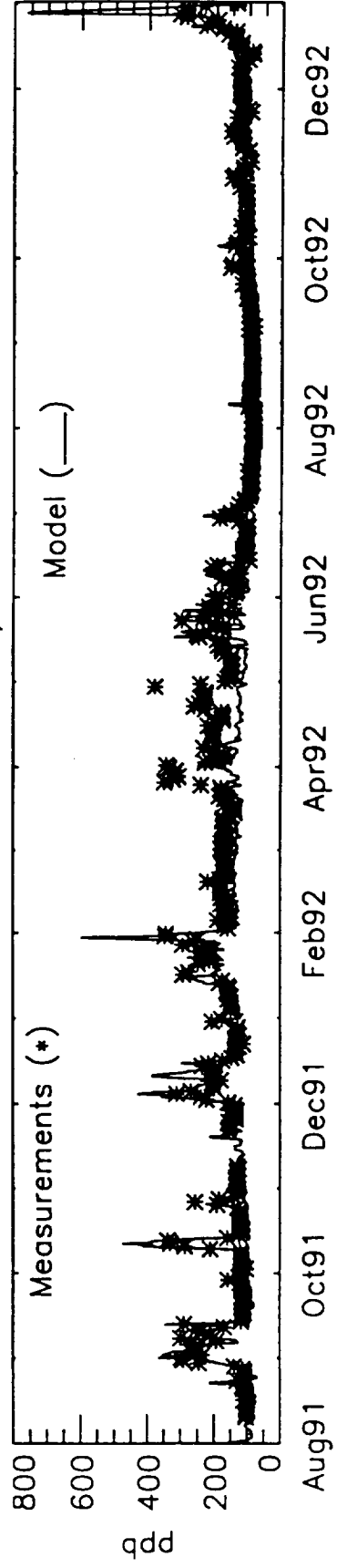
7a-b

Locations of selected sites in NOAA/CMDL Network

8

CO at Mace Head

CO at Key Biscayne

CO at Guam

CO at Barrow

CO at Bermuda

CO at Cape Kumukahi

CO at Seychelles

CO at Samoa

CO at Christmas Island

CO at Ascension Island

CO at Cape Grim

Data [___]   Model [- - -]

ppbv

$o_3 - k$

Mace Head, Ireland residuals

Data [——] Model(s)[— — —]

Key Biscayne, Fl residuals

Data [——] Model(s)[— — —]

Guam, Mariana Islands residuals

Data [——] Model(s)[— — —]

Barrow, Alaska residuals

Data [——] Model(s)[— — —]

Bermuda residuals

Data [——] Model(s)[— — —]

Cape Kumukahi, HW residuals

Data [——] Model(s)[— — —]

10a

Seychelles residuals

Data [——]   Model(s) [— — —]

ppbv
15
10
5
0
−5
−10

1988 1989 1990 1991 1992 1993

American Samoa residuals

Data [——]   Model(s) [— — —]

ppbv
15
10
5
0
−5
−10

1988 1989 1990 1991 1992 1993

Christmas Island residuals

Data [——]   Model(s) [— — —]

ppbv
15
10
5
0
−5
−10
−15

1988 1989 1990 1991 1992 1993

Ascension Island residuals

Data [——]   Model(s) [— — —]

ppbv
30
20
10
0
−10
−20

1988 1989 1990 1991 1992 1993

Cape Grim residuals

Data [——]   Model(s) [— — —]

ppbv
6
4
2
0
−2
−4

1988 1989 1990 1991 1992 1993

Mean CO at 300 hPa during October
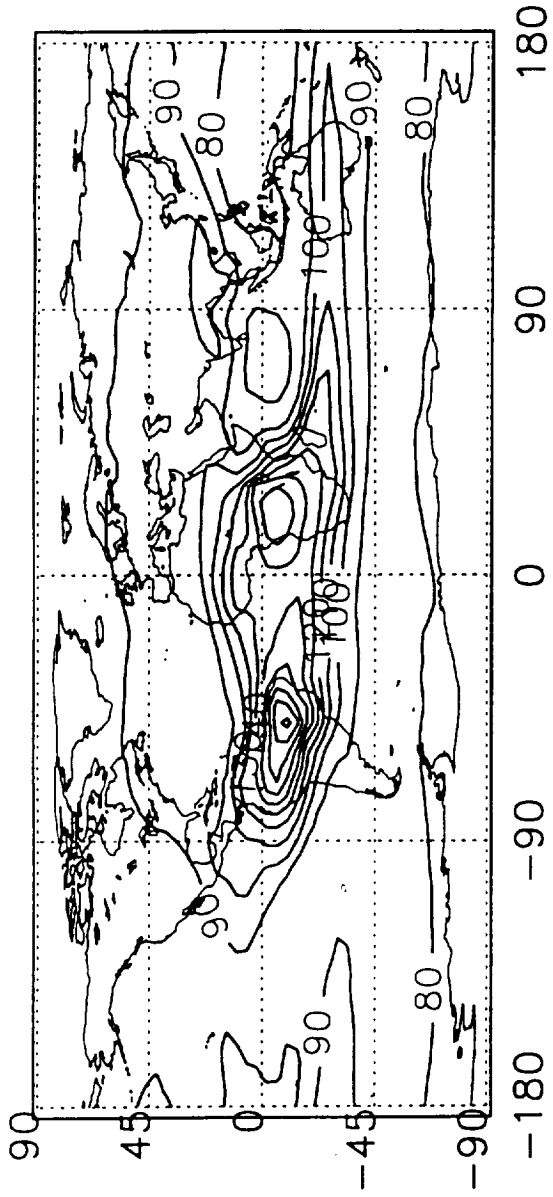
Variability at 300 hPa during October

300 hPa wind during Oct 1990

300 hPa wind during Oct 1993

Max wind = 11.0873 m/s

Max wind = 12.7669 m/s

0   −10   −20   −30

0   −10   −20   −30

0   20   40   60

0   20   40   60
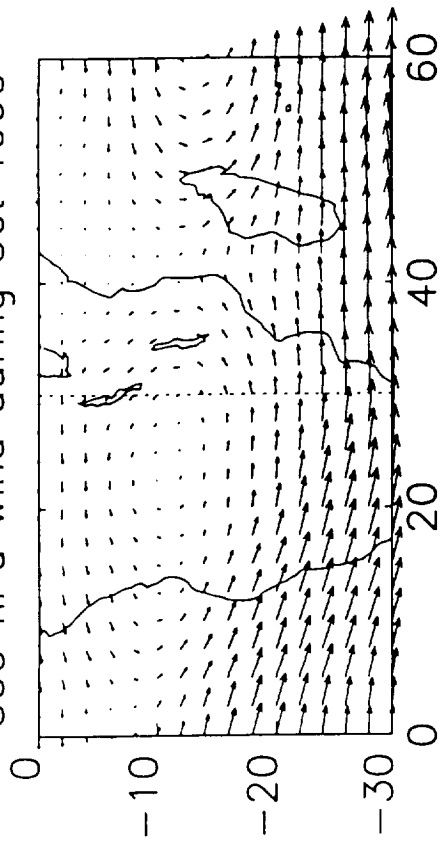
CO source October

Oct 93−Oct 90 CO at 300 hPa

0   −10   −20   −30

0   −10   −20   −30

0   20   40   60

0   20   40   60

−30   −20   −10   0   10

F-121
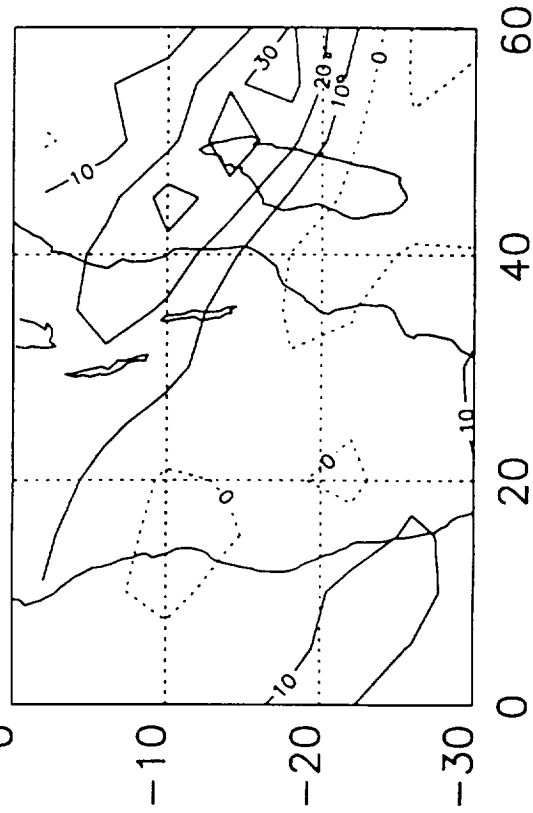
300 hPa wind during Oct 1990
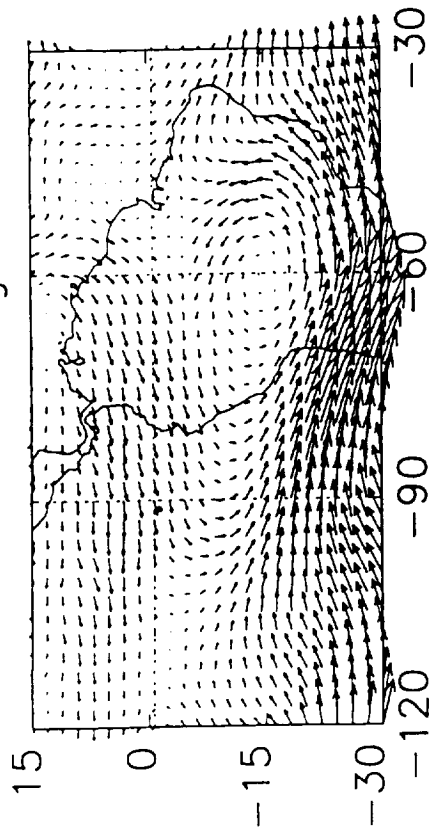
Max wind = 19.9074 m/s

300 hPa wind during Oct 1993
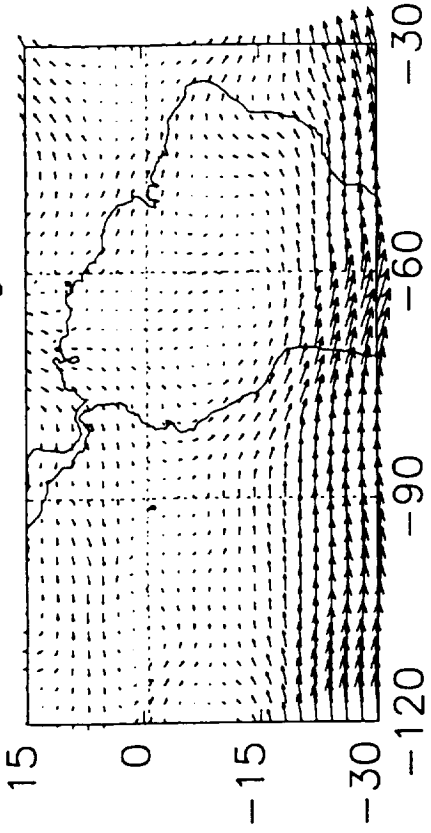
Max wind = 16.1279 m/s

CO source October
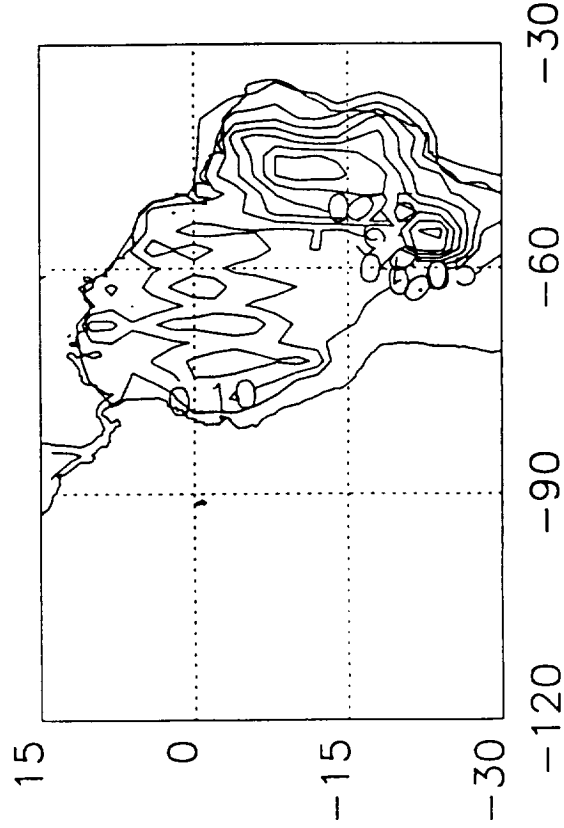
Oct 90–Oct 93 CO at 300 hPa
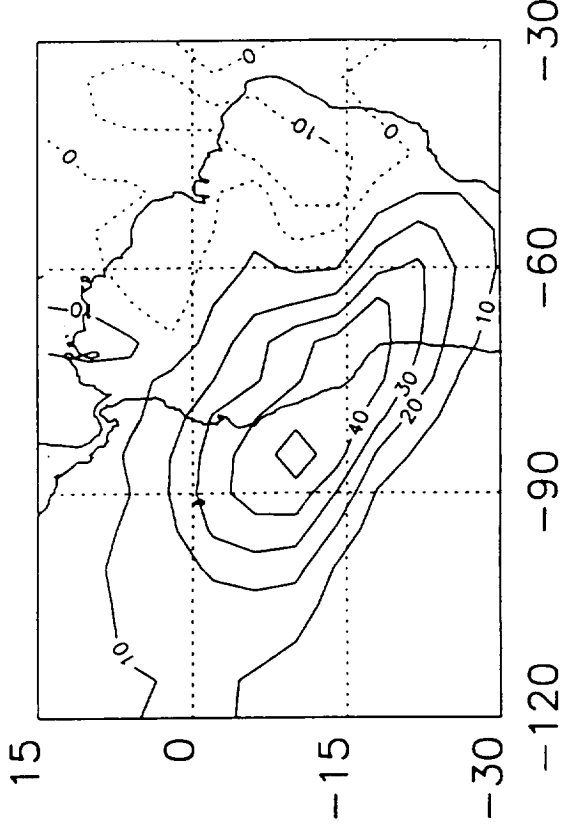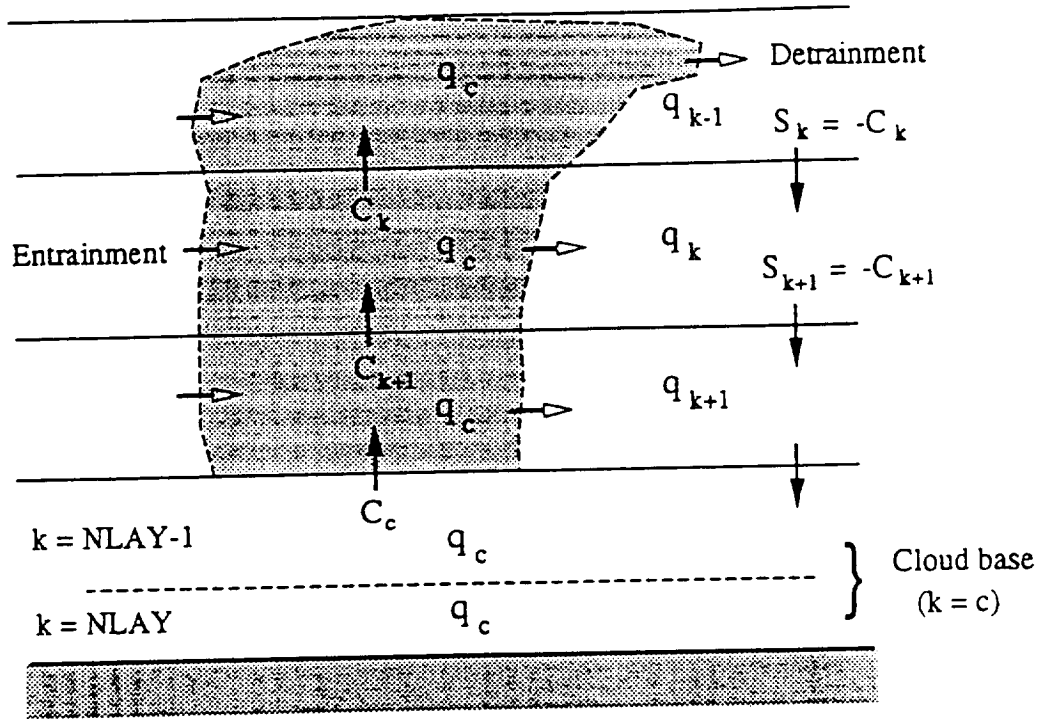
Fig. 1 Schematics of the cloud mass flux model

APPENDIX C

INTERCOMPARISON OF GLOBAL ATMOSPHERIC TRANSPORT MODELS

USING ^{222}Rn AND OTHER SHORT-LIVED TRACERS

Daniel J. Jacob[1], Michael J. Prather[2], Philip J. Rasch[3], Johann Feichter[4], Ines Köhler[5], Prasad S. Kasibhatla[6], Gé Verver[7], P.J.M. Van Velthoven[7], Jane E. Dignon[8], Joyce E. Penner[8], Daniel J. Bergmann[8], Christophe Genthon[9], Yves J. Balkanski[10], Michel Ramonet[11], Peter Zimmermann[12], Stephen R. Beagley[13], J. de Grandpré [13], W.T. Blackshear[14], W.L. Grose[14], Douglas A. Rotman[8], Masaru Chiba[15], Martyn Chipperfield[16], Zoe Stockwell[16], Run-Lie Shia[17], Kathy Law[16], Oliver Wild[16], Claire E. Reeves[18], Margaret Brown[19,20], Hu Yang[19], M.A. Kritz[21]

[1] Division of Applied Sciences and Department of Earth & Planetary Sciences, Harvard University, Cambridge, MA 02138, USA

[2] Department of Geoscience, U. California at Irvine, Irvine, CA 92717, USA

[3] National Center for Atmospheric Research, Boulder, CO 80303, USA

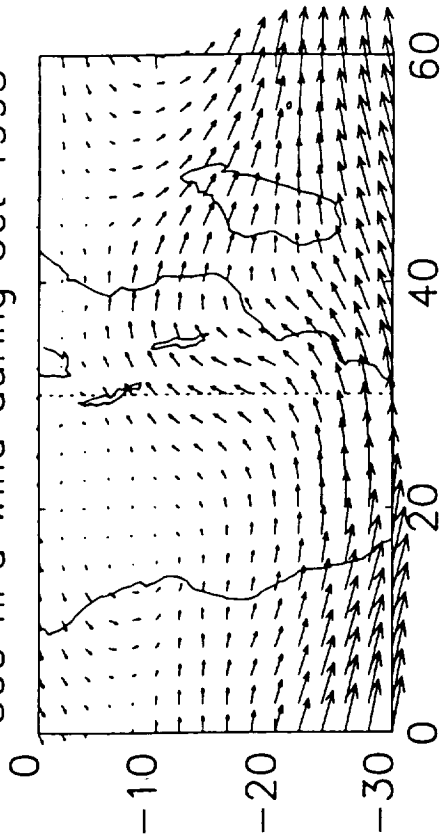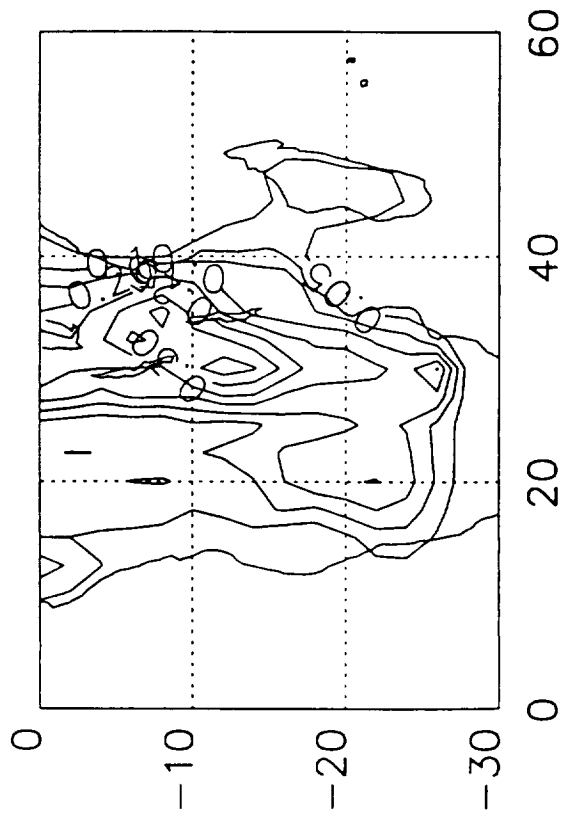[4] Max-Planck-Institut für Meteorologie, Bundesstr. 55, D-20146 Hamburg, GERMANY

[5] Institut für Physik der Atmosphäre, DLR Oberpfaffenhofen, D-82234 Wessling, GERMANY

[6] School of Earth and Atmospheric Sciences, Georgia Institute of Technology, Atlanta, GA 30332, USA

[7] Royal Netherlands Meteorological Institute (KNMI), P.O.Box 201, 3730 AE De Bilt THE NETHERLANDS

[8] Lawrence Livermore National Laboratory, P.O.B. 808, Livermore, CA 94550, USA

[9] Laboratoire de Glaciologie et Géophysique de l'Environnement, CNRS, Domaine Universitaire BP 96, Saint Martin d'Hères, 38402, FRANCE

[10] Laboratoire de Modèlisation du Climat et de l'Environnement, CEA, Gif sur Yvette Cedex - 91191 FRANCE

[11] Centre des Faibles Radioactivités, Laboratoire mixte CNRS/CEA, Gif sur Yvette Cedex, 91198 FRANCE

[12] Max-Planck Institut fur Chemie, Postfach 3060, Mainz, D-6500 GERMANY

[13] York Univ., 4700 Keele St. Petrie Bldg #153, North York, ON M3J 1P3 CANADA

[14] NASA Langley Research Center, Hampton, VA 23681, USA

[15] Second Laboratory of Climate Research Devision, Meteorological Research Institute. 1-1, Nagamine, Tsukuba, Ibaraki, 305 JAPAN

[16] Dept. Chemistry, Univ. Cambridge, Lensfield Rd., Cambridge CB2 1EW ENGLAND

[17] AER Inc., 840 Memorial Dr., Cambridge, MA 02139

[18] School of Environmental Sciences, University of East Anglia, Norwich NR4 7TJ, ENGLAND

[19] Department of Applied Mathematics, University of Washington, Seattle, WA 98195

[20] now at Battelle Pacific Northwest Lab, POB 999, Richland, WA 99352

[21] Atmospheric Sciences Research Center, State University of New York, Albany, Western Field Office, P.O. Box 468, Moffett Field, CA 94035-0468

[Address correspondence to D.J. Jacob, Pierce Hall, 29 Oxford St., Cambridge, MA 02138; phone 617-495-1794; fax 617-495-9837; email djj@io.harvard.edu]

ABSTRACT

An intercomparison of global atmospheric transport models using short-lived tracers was held in December 1993 to evaluate the ability of these models to capture the contributions of convective and synoptic processes to global-scale transport. Twenty models participated including nine established three-dimensional (3-D) models with resolved synoptic-scale meteorology, one established 3-D model with monthly averaged transport, six 3-D synoptic models under development, and four 2-D models. Primary focus was on simulation of ^{222}Rn, a gaseous tracer emitted by soils and removed by radioactive decay with an e-folding lifetime of 5.5 days. Additional simulations were conducted for aircraft and lightning tracers released in the upper troposphere, and for aerosol ^{210}Pb produced in the atmosphere by decay of ^{222}Rn (only four models conducted this last simulation). The seasonal statistics of ^{222}Rn concentrations simulated by the established 3-D synoptic models were in general consistent with available observations. However, none of the models were able to capture the high ^{222}Rn concentrations observed in the upper troposphere over the North Pacific, and large discrepancies between models were found in the simulation of meridional transport in the upper troposphere. Remarkable similarity was found between the established 3-D models in the simulated vertical gradients of ^{222}Rn and other tracers, implying that the diverse subgrid convective parameterizations used in the different models yield comparable vertical mass fluxes. Models under development that did not include a subgrid parameterization of convective transport underestimated considerably the ^{222}Rn concentrations in the upper troposphere. The 2-D models yielded mean meridional transport rates consistent with the 3-D models but tended to underestimate vertical exchange between the lower and upper troposphere. The four models participating in the ^{210}Pb aerosol intercomparison yielded global mean aerosol residence times against deposition ranging from 7 to 13 days; the lower end appears to be most consistent with observations.

1. INTRODUCTION

Convective and synoptic processes play a major role in the global transport of heat, momentum, and trace gases in the atmosphere. Capturing these processes in global models is a challenge because of the coarse model resolution (typically 100-1000 km in the horizontal). Convection is subgrid on these scales and must be parameterized. Synoptic motions are near the grid scale. In December 1993 the World Climate Research Program (WCRP) held an intercomparison of global atmospheric transport models to test the ability of these models to capture the contributions of convective and synoptic processes to global-scale transport. Twenty models from seven countries participated, spanning the range of current modeling approaches including three-dimensional (3-D) and 2-D; Eulerian, spectral, Lagrangian, and semi-Lagrangian; 8 different general circulation models (GCMs) and two assimilated meteorological data sets. We report here on the principal results.

The intercomparison used simulations of short-lived tracers as sensitive diagnostics. Primary focus was on ^{222}Rn, a natural radioisotope emitted ubiquitously from soils by decay of ^{226}Ra [Nazaroff, 1992] and removed from the atmosphere by radioactive decay with an e-folding lifetime of 5.5 days. Because of its simple source and sink, ^{222}Rn has long been recognized as a useful tracer of convective and synoptic-scale transport in global atmospheric models [Liu et al., 1984; Brost and Chatfield, 1989; Feichter and Crutzen, 1990; Jacob and Prather, 1990; Allen et al., 1995; Mahowald et al., 1995; Rind and Lerner, 1995]. A comparative analysis of two GCMs using ^{222}Rn as a tracer was recently reported by Genthon and Armengaud [1995a].

Also included in the intercomparison were simulations of artificial short-lived tracers descriptive of aircraft and lightning emissions. These simulations were aimed at examining downward transport and horizontal motions in the upper troposphere, complementing the simulation of ^{222}Rn. The results could not be compared to observations but still allowed an assessment of differences between models.

Four models participated in an intercomparison of ^{210}Pb, an aerosol tracer produced in the atmosphere by decay of ^{222}Rn [Turekian et al., 1977]. Wet deposition is the principal mechanism for aerosol removal from the atmosphere, and is highly sensitive to the frequency of precipitation and to the parameterization of aerosol scavenging [Giorgi and Chameides, 1985, 1986; Feichter et al., 1991; Balkanski et al., 1993]. A large data base of ^{210}Pb observations is available from surface sites around the world, and there are also a limited number of observations at altitude [Lambert et al., 1982]. The ^{210}Pb intercomparison was a preliminary exercise; a more extensive intercomparison of aerosol transport in global models was conducted by WCRP in August 1995 (organizers were P.J. Rasch, H. Feichter, K. Law, and J.E. Penner).

2. SIMULATIONS

Table 1 lists the 20 participating models; descriptions of each are given in the Appendix. Sixteen of the models were 3-D and four were 2-D (latitude-altitude). All 3-D models except MOGUNTIA resolved daily weather (i.e., used meteorological data with resolution finer than one day) and are referred to as "synoptic" models. Most models had a recorded history of use prior to the intercomparison and are referred to as "established". Other models were still under development at the time of the intercomparison and are identified as such in Table 1. Participation of 2-D models made it possible to document the extent to which these models can reproduce the zonal mean features of the 3-D models. Because of their computational advantage, 2-D models have been used extensively in tropospheric chemistry assessments involving simulation of short-lived species such as nitrogen oxides (NO_x) [Intergovernmental Panel on Climate Change, 1992, 1994].

The intercomparison consisted of four simulations, described in Table 2. The ^{222}Rn simulation (case A) used a uniform emission of 1.0 atoms cm^{-2} s^{-1} from land excluding polar regions. This source is probably accurate to within 25% on the global

scale and a factor of 2 on the regional scale [Wilkening et al., 1975; Turekian et al., 1977; Schery et al., 1989; Graustein and Turekian, 1990; Nazaroff, 1992; Balkanski et al., 1993]. The dominant causes of variability are the ^{226}Ra abundance in soil, the location of ^{226}Ra within the soil grains, soil moisture, and soil freezing [Jacob and Prather, 1990; Nazaroff, 1992; Ussler et al., 1993]. These effects are not well quantified on a global scale, and there is therefore little justification for using a more complicated source than given in Table 2. Ignoring the effect of soil freezing overestimates the source at high latitudes in winter [Jacob and Prather, 1990; Genthon and Armengaud, 1995a]. The assumed oceanic source of 0.005 atoms cm^{-2} s^{-1} is an upper limit [Wilkening and Clements, 1975; Lambert et al., 1982], and is unimportant except for defining background concentrations in the marine boundary layer.

The tracers in cases B and C had the same lifetimes as ^{222}Rn but were released in the upper troposphere (400-200 mb column) at northern mid-latitudes and in the tropics respectively. Their source distributions were intended to be illustrative of emissions from aircraft (case B) and tropical lightning (case C). Simulation of nitrogen oxide (NO_x) emissions from these two sources is of particular importance for modeling of global tropospheric chemistry.

The ^{210}Pb simulation used the ^{222}Rn decay rates computed in case A to specify the ^{210}Pb source. Loss of ^{210}Pb by wet deposition was left up to the participants to compute using their own schemes for scavenging a submicrometer, water-soluble aerosol. Additional loss of ^{210}Pb by dry deposition was imposed with a uniform dry deposition velocity of 0.1 cm s^{-1} referenced to 10-m altitude.

Simulations were conducted for two four-month periods, May-August and November-February, starting from zero tracer concentrations. The first month served as initialization; model output was sampled for the last 3 months. Since different models were based on different meteorological years, only 3-month seasonal statistics were used for intercomparison. It should be noted that discrepancies between model results may

reflect not only differences in modeling approaches but also interannual variability in weather.

The intercomparison diagnostics requested from each model are listed in Table 3. Diagnostics for cases A-C included contour plots of 3-month average concentrations, and time series of concentrations at 7 sites and three altitudes: 300 m above the surface (mixed layer), 600 mb, and 300 mb. Diagnostics for the ^{210}Pb simulation consisted of global inventories and latitude-pressure cross-sections of 3-month average concentrations. Concentration units for the diagnostics were molar mixing ratios (mol/mol); conversion factors to common radioactivity units are given in Table 3a.

The sites for the time series (Table 3b) were chosen for the availability of ^{222}Rn observations and also to sample a range of different environments. The time series for the mixed layer were sampled only once a day in early afternoon, when the mixed layer depth is near its maximum and hence when model results are least sensitive to details in the vertical gridding near the surface and subgrid surface layer parameterizations. Time series at 600 mb and 300 mb were sampled at all times of day. No coastal sites were used for intercomparison because the sharp concentration gradient across the coastline makes results for these sites strongly dependent on details in the grid geometry of the model [Genthon and Armengaud, 1995a]. Thus we did not consider Chester, New Jersey, where a particularly long record of ^{222}Rn observations is available (Jacob and Prather [1990] and references therein).

Participants were requested to submit their results prior to an intercomparison workshop which was held on 30 November - 3 December, 1993 and was attended by representatives of almost all models. Participants were not allowed to revise their submitted results following the workshop except for correcting errors in input conditions and output diagnostics. They were however allowed to withdraw. One participant withdrew its simulations for Cases B and C. Two participants withdrew their ^{210}Pb simulations. There were no other withdrawals.

3. CASE A (^{222}Rn): COMPARISONS WITH OBSERVATIONS

Reviews of the observational data base for ^{222}Rn have been presented by Lambert et al. [1982], Gesell [1983], and Liu et al. [1984]. Only a few data sets are sufficiently extensive to offer seasonal statistics suitable for model evaluation. For these data sets the original time series of observations are generally unavailable, so that the only usable comparison statistics are those that can be retrieved from the literature. We focus our attention on Cincinnati, United States (40°N, 84°W); Crozet Island, Indian Ocean (46°S, 51°E), and 200 mb over Hawaii (20°N, 155°W); these locations offer the best published statistics for comparison with model results in continental interior, marine air, and upper troposphere environments. We will also compare the vertical profiles simulated by the models over northern mid-latitudes continents to the observational averages reported by Liu et al. [1984].

Cincinnati, United States

Figure 1 (top panel) shows the seasonal frequency distributions of ^{222}Rn concentrations simulated by the models at Cincinnati, Ohio at 1400h local time in June-August. Cincinnati is in the continental interior of the United States, where the principal influence on ^{222}Rn concentrations should be the vertical mixing and ventilation of the continental boundary layer. A 4-year data set of observations at Cincinnati has been reported by Gold et al. [1964]. Dashed lines in Figure 1 indicate the interannual range of the observed June-August means in early afternoon (80-105x10^{-21} mol/mol). The observations were made a few meters above the ground, while the models were sampled at 300-m altitude; the difference in concentration between these two altitudes is small during daytime summer as the surface layer is unstable and the mixed layer extends above 300-m altitude [Moses et al., 1960].

The degree of agreement between model and observations is assessed by comparing the June-August 1400h means in the models (white bands in Figure 1) to the interannual

range of the corresponding means in the observations (dashed lines). Most 3-D models are consistent with observations to within the uncertainty of ^{222}Rn emission. The 2-D models [R-U] are too low, as would be expected because of zonal averaging of the ^{222}Rn source over land and ocean. Concentrations in CCM2 [A], MOGUNTIA [J], and LLNL/IMPACT (n) are only slightly higher than the 2-D models and lower than observed, implying excessive boundary layer mixing. Post-intercomparison inspection of CCM2 revealed that boundary layer depths were indeed excessive, and subsequent versions of the CCM2 are improved. Concentrations in ECHAM3 [B] are much higher than observed, in part because the model was sampled twice a day rather than at 1400h local time as in the other models; still, additional diagnostics indicate that the average continental boundary layer concentrations simulated by ECHAM3 are a factor of 2 higher than in the other established 3-D synoptic models.

The published observational statistics for Cincinnati do not include information on day-to-day variability. As seen in Figure 1, all 3-D synoptic models show pronounced day-to-day variability reflecting weather disturbances. The variability is remarkably similar in all established 3-D models except ECHAM3; relative standard deviations (σ/μ) vary over a narrow range from 15% in LLNL/E (G) to 29% in CCM2. Higher variability is found in ECHAM3, MRI [o], TOMCAT [p], and UGAMP [q], reflecting frequent occurrences of anomalously high concentrations (ECHAM3 was sampled in both day and night, but only a small fraction of the variability is due to the diel cycle because sampling was at 300-m altitude). Occurrences of high concentrations would normally be caused by lack of ventilation of the 0-300 m column. In the extreme case of full mixing up to 300-m and no mixing above, ^{222}Rn concentrations in the 0-300 m column would build up to a steady-state value of 640×10^{-21} v/v (limited by the e-folding lifetime of 5.5 days against radioactive decay). The seasonal maximum reported by TOMCAT is still higher than this theoretical maximum.

Crozet Island, Indian Ocean

The middle panel of Figure 1 shows the frequency distributions of ^{222}Rn concentrations simulated by the models in June-August at Crozet Island. Crozet is located in the subantarctic Indian Ocean 2800-km from the African coast. Twenty years of continuous measurements have been made at this site [Polian et al., 1986]. The data indicate a low background of $0.1-1\times10^{-21}$ mol/mol interrupted about once a month by high- ^{222}Rn episodes lasting typically 1-2 days [Lambert et al., 1970; Polian et al., 1986]. The episodes are caused by fast boundary layer transport of air from Africa in a circulation driven by the semi-permanent subtropical Mascarene High to the north and transient mid-latitude cyclones to the south [Balkanski and Jacob, 1990; Heimann et al., 1990; Miller et al., 1993]. The peak ^{222}Rn concentrations observed during the episodes are usually $5-10\times10^{-21}$ mol/mol, with exceptional occurrences of up to 25×10^{-21} mol/mol [Polian et al., 1986]. Seasonal statistics in the models should thus yield 75th percentiles less than 5×10^{-21} mole/mole and maxima in the range of $5-25\times10^{-21}$ mole/mole.

We see from Figure 1 that all established 3-D synoptic models reproduce qualitatively the observed temporal structure of low ^{222}Rn background interrupted by occasional high- ^{222}Rn episodes. The seasonal maxima are consistent with observations except in GFDL/ZODIAC [C] where one episode is anomalously high. The median concentrations ($1-2\times10^{-21}$ mol/mol) are higher than observed, probably due to overestimate of the oceanic source. Inspection of individual time series indicates that the established 3-D synoptic models simulate between 3 and 8 high- ^{222}Rn episodes over the 3-month period, and that none of the episodes lasts longer than 3 days, consistent with observations. It thus appears that the models resolve the time scale of the transient weather systems advecting continental air to Crozet. The sharp structure of the high- ^{222}Rn episodes in the models demonstrates further their ability to transport continental air masses over the ocean without appreciable numerical diffusion.

Among the 3-D models under development, only MRI [o] yields statistics comparable to the established 3-D models. CCCA-GCM [k] and especially LLNL/IMPACT [n]

have too high medians; LaRC [m] does not simulate high- ^{222}Rn episodes; TOMCAT [p]

has an anomalously high maximum; and UGAMP [q] produces negative concentrations.

The 2-D models yield higher ^{222}Rn concentrations at Crozet than the 3-D models, a

difference that can be explained by inclusion of the South American land mass in the

zonal means at 46°S (latitude of Crozet). Inspection of zonal mean concentrations at

46°S indicates in fact agreement to within a factor of 2 between the 2-D models and the

established 3-D models.

The 3-D model MOGUNTIA [J], which uses monthly mean winds and a 10°x10°

horizontal resolution, shows median concentrations at Crozet that are comparable to the

2-D models and higher than observed, suggesting that the model resolution is too coarse

to capture the gradient between the African continent and the island. Genthon and

Armengaud [1995a] found a similar problem when using the GISS GCM with 8°x10°

resolution to simulate high- ^{222}Rn episodes at Kerguelen Island, near Crozet; the problem

disappears when the 4°x5° resolution version of the GCM is used [Balkanski and Jacob,

1990].

Upper troposphere over Hawaii

Kritz et al. [1990] reported 61 aircraft measurements of ^{222}Rn concentrations at

200 mb over the North Pacific between California and Hawaii in July-August 1983-1984.

Seventeen of these measurements were made near Hawaii at 18-25°N (the individual

measurements are shown in Balkanski et al. [1992]). Each measurement was a 30-

minute average, representing an aircraft travel distance of about 250 km. The median

concentration for the 17 points was 2.5×10^{-21} mol/mol; 3 of the 17 points had concentra-

tions higher than 10×10^{-21} mol/mol, and the highest concentration was 26×10^{-21}

mol/mol. Kritz et al. [1990] showed that the extremely high concentrations were due to

deep convection over eastern Asia followed by rapid transport over the Pacific in the sub-

tropical jet.

Simulated frequency distributions of ^{222}Rn concentrations in the upper troposphere over Hawaii in summer are shown in the bottom panel of Figure 1. The observed median and extrema of Kritz et al. [1990] are shown respectively as dashed and dotted lines. The model results are for 300 mb, whereas the Kritz et al. [1990] observations are at 200 mb; however, inspection of seasonally averaged latitude-altitude cross-sections in the models at the dateline indicates less than 30% vertical differences in concentrations between 300 and 200 mb at the latitude of Hawaii. The model statistics at 300 mb can therefore be justifiably compared to the Kritz et al. [1990] data.

We see from Figure 1 that all 3-D models except LLNL/E [G] underestimate the observed median concentrations by typically a factor of 2. The maxima are underestimated by a greater factor, i.e., the models do not capture the large relative variability in the observations. Concentrations simulated by LaRC [m] and LLNL/IMPACT [n] never exceed 0.1×10^{-21} mol/mol, which may be explained by the lack of a subgrid convective parameterization to transport ^{222}Rn to high altitudes in these models. All 2-D models except UW [U] show concentrations lower than the observed median, even though concentrations over Hawaii should be less than the zonal mean. This apparent underestimate of ^{222}Rn probably reflects insufficient accounting of deep convective motions in the 2-D models, as discussed further below.

One possible explanation for the failure of the 3-D models to reproduce the high concentrations observed over Hawaii would be the presence of an anomalously high ^{222}Rn source in eastern Asia. P. Kasibhatla and N. Mahowald [personal communication] have proposed such an explanation to account for the unusually high ^{222}Rn concentrations observed at Mauna Loa Observatory, Hawaii. There are to our knowledge no measurements of ^{222}Rn concentrations or ^{222}Rn emission fluxes over eastern Asia. Deposition flux data for ^{210}Pb available from one site in Japan indicate values more than twice higher those found at any site in the United States or Europe [Fukuda and Tsunogai, 1975; Turekian et al., 1977; Balkanski et al., 1993].

Vertical profiles over continents

Seasonal mean vertical profiles of ^{222}Rn concentrations over northern mid-latitude continents have been compiled by Liu et al. [1984] by averaging together measurements made at different locations in North America and Europe. The data base is scant, consisting of 23 profiles at 6 locations in summer and 7 profiles at 3 locations in winter. The mean profiles for summer and winter are shown in Figure 2 along with standard errors ($\sigma/\sqrt{n}$). Because the data are from a small number of locations, the standard errors certainly underestimate the actual uncertainties on the mean ^{222}Rn concentrations over northern mid-latitude continents.

We compare the Liu et al. [1984] profiles in Figure 2 to the results from the individual models averaged over the three continental sites for which time series were archived (Kirov, Cincinnati, Socorro). Most of the established 3-D models reproduce the observed profiles to within a factor of 2 at all altitudes. Exceptions are LLNL/E [G] in summer, where deep convection is too weak, and ECHAM3 [B] where mixed layer concentrations are a factor of 2 higher than in other established 3-D models for both summer and winter. Considerable underestimate of concentrations in the middle and upper troposphere is found in 3-D models under development that do not include a subgrid parameterization of convective transport (LaRC [m], LLNL/IMPACT [n], TOMCAT [p]). The 2-D models generally underestimate the observations, as would be expected due to the zonal averaging in these models; however UW [U] overestimates concentrations in the middle and upper troposphere in winter, implying excessive vertical mixing.

Deep convective transport over continents is an episodic process, and concentrations of continental tracers in the upper troposphere are known to be highly variable [Dickerson et al., 1987; Pickering et al., 1995]. There are few ^{222}Rn observations available in the upper troposphere over continents for evaluating the variability in the models. The largest single source of upper troposphere data in the compilation of Liu et al. [1984] is from four aircraft flights over eastern Ukraine in July [Nazarov et al., 1970].

We compare in Figure 3 the range of values reported by Nazarov et al. [1970] at 300 mb to the summertime frequency distributions simulated by the established 3-D synoptic models at the same altitude over Kirov. The seasonal ranges in the models encompass the range defined by the observations, but not by much; considering that the observational range is defined by just four individual measurements, while the model ranges are from continuous sampling of a 3-month time series, it appears that the 3-D models underestimate the variability of ^{222}Rn in the continental upper troposphere.

4. CASES A-C: GLOBAL DISTRIBUTIONS

Global distributions of seasonally averaged concentrations afford a more general intercomparison of model results. We limit our analysis to the established models and to CCCA-GCM; as pointed out above, some of the models under development exhibited major anomalies when compared to observations.

Figure 4 compares the global distributions of ^{222}Rn concentrations at 300 mb in June-August for the different 3-D models. All models show remarkably similar patterns of convective pumping over continents and long-range transport over the oceans. Exceptions are MOGUNTIA, CCCA-GCM, and the LLNL models (especially the Eulerian version, LLNL/E), where concentrations are generally a factor of two lower than the other models. ECHAM3 shows particularly high concentrations in polar regions, reflecting strong meridional transport from middle to high latitudes in the upper troposphere.

Zonal mean cross-sections of ^{222}Rn concentrations as a function of altitude and latitude in June-August are compared in Figure 5. Meridional and vertical structures in the 3-D models are similar to a high degree of detail, as seen for example in the patterns of deep convection in the tropics, lower-level convection at northern mid-latitudes, and meridional gradients in the lower and middle troposphere. There are however some differences. In particular, GISS/H/I features a secondary maximum of concentrations in the equatorial upper troposphere due to frequent deep convection, but none of the other

models show such a maximum. All 2-D models except UW underestimate concentrations in the upper troposphere, a problem likely caused by inadequate treatment of convection. UW captures successfully much of the structure of the 3-D models.

Figure 6 shows the mean June-August concentrations simulated by the 3-D models at 300 mb for the aircraft tracer of Case B. All models show remarkably similar large-scale horizontal dispersion of the tracer. Zonal mean cross-sections for Case B in June-August are presented in Figure 7. Most models show similar vertical gradients at northern mid-latitudes, implying similar rates of downward transport, except KNMI/TM2 where this transport is unusually rapid. Large differences are found between the 3-D models in the rates of meridional transport in the upper troposphere. GISS/H/I and ECHAM3 show particularly slow interhemispheric transport at high altitudes, resulting in tracer concentrations in the southern tropics that are one order of magnitude lower than in the LLNL models and CCM2 where interhemispheric transport is particularly rapid. Transport from northern mid-latitudes to the Arctic in the upper troposphere also varies considerably between 3-D models; concentrations at the North Pole differ by more than one order of magnitude between MOGUNTIA (where transport is fastest) and GFDL/ZODIAC (slowest). A more recent version of MOGUNTIA using ECMWF winds shows a substantial reduction of transport to high latitudes, resulting in tracer concentrations at the North Pole that are more consistent with the other 3-D models. The zonal mean cross-sections of concentrations in the 2-D models are generally consistent with the range of results from the 3-D models, although the latitude range of maximum downward transport appears to be misplaced in UW.

Figure 8 shows the zonal mean cross-sections of concentrations in December-February for the tropical lightning tracer (Case C). All 3-D models show similar vertical gradients in the tropics, implying again close similarity in the computed rates of downward transport. An exception is MOGUNTIA, which features tracer concentrations in the lower tropical troposphere that are five times higher than the other established 3-D

models. A more recent version of MOGUNTIA shows much improvement. Meridional transport rates from the tropics to high latitudes in the upper troposphere show considerable differences between 3-D models, in a manner similar to those found in case B. Downward transport in the tropics in the 2-D models is too fast in UW and rather too slow in AER and UCAMB. Meridional transport rates in the 2-D models are consistent with the range of values in the 3-D models.

5. AEROSOL ^{210}Pb

Four models participated in the ^{210}Pb aerosol intercomparison: GISS/H/I, LLNL/GRANTOUR, UCAMB, and HARWELL. Each model uses a different scheme for wet scavenging of aerosols. GISS/H/I scavenges aerosol in subgrid wet convective updrafts and also has a first-order rainout scheme for large-scale precipitation. LLNL/GRANTOUR assumes a first-order loss rate normalized to precipitation intensity. UCAMB uses specified aerosol lifetimes as a function of altitude. HARWELL predicts rainfall rates on the basis of the local relative humidity and assumes similarity between scavenging of aerosols and water vapor. References for the various schemes are given in the Appendix.

Figure 9 shows the global ^{210}Pb inventories simulated by each model for August 31 and February 28, partitioned into three altitude bands. Also shown is the global inventory of 1.4 moles obtained by Lambert et al. [1982] by partitioning geographically and averaging the available data base of observations from surface sites, ship cruises, and aircraft. There are few aircraft observations in the troposphere, and Lambert et al. [1982] had to relie heavily on vertical extrapolation of surface observations. They did not account for seasonality in their inventory, arguing that it would be small; indeed, none of the model inventories in Figure 9 differ by more than 20% between February and August.

The global inventories simulated by the models are 1.4 moles in UCAMB, 1.8 moles in LLNL/GRANTOUR, 2.1 moles in GISS/H/I, and 2.7 moles in HARWELL.

UCAMB agrees well with Lambert et al. [1982], while other models are too high. Considering that all models have the same source of ^{210}Pb, the total atmospheric loadings can be converted to global mean aerosol residence times (shown as additional ordinate in Figure 9) ranging from 7 days in UCAMB to 13 days in HARWELL.

In order to evaluate the vertical distribution of ^{210}Pb in the models, we reconstructed the global inventory of Lambert et al. [1982] by following their procedures and retaining information on vertical resolution. Their inventory of 1.4 moles can thus be partitioned into 0.58 moles below 600 mb, 0.34 moles at 600-300 mb, and 0.52 moles above 300 mb; 80% of the inventory above 300 mb is in the stratosphere. The large contribution of the stratosphere to the ^{210}Pb inventory is a well-known feature of the observations and is due to a combination of ^{222}Rn-rich air entering the stratosphere and the absence of aerosol removal processes within the stratosphere [Lambert et al., 1990]. It appears from Figure 9 that HARWELL is too high in the lower troposphere while GISS/H/I is too high above 300 mb. Previous studies using GISS/H/I have documented problems related to insufficient scavenging of aerosols in the upper troposphere [Koch et al., 1995] and excessive transport of air from the troposphere to the stratosphere [Spivakovsky and Balkanski, 1994]. Both of these problems would contribute to an overestimate of ^{210}Pb above 300 mb.

6. CONCLUSIONS

Intercomparison of 20 global atmospheric transport models representing the state-of-the-science as of December 1993 indicates that these models can capture to a significant degree the contributions of convective and synoptic processes to global-scale transport. The current cohorte of established 3-D models is in general successful at reproducing the observed concentrations of ^{222}Rn over continents, including both surface air concentrations and vertical gradients in the tropospheric column. These 3-D models also capture the observed episodic structure of long-range transport of ^{222}Rn

over the oceans. However, none of the models can reproduce the high ^{222}Rn concentrations observed in the upper troposphere over Hawaii. Models under development at the time of the intercomparison were in general less successful in reproducing the ^{222}Rn observations.

The 3-D models revealed remarkable similarity in their simulations of mean vertical gradients for ^{222}Rn and other tracers, despite the diversity of parameterizations used to describe boundary layer meteorology and convective transport. This result suggests that the parameterization of convection in 3-D models is better constrained than is usually assumed, i.e., that different parameterizations yield comparable convective mass fluxes. The 3-D models under development that did not include a subgrid parameterization of convective transport underestimated considerably the ^{222}Rn concentrations in the upper troposphere.

Large differences were found between established 3-D models in the representations of meridional transport in the upper troposphere, including in particular interhemispheric transport. This result suggests that the models may have widely different interhemispheric exchange times; the issue needs to be investigated further by simulations of long-lived tracers such as chlorofluorocarbons (CFCs) or ^{85}Kr.

Comparisons of zonal mean quantities in the 2-D vs. 3-D models indicated that the 2-D models offer a reasonable simulation of large-scale meridional transport in the troposphere. However, they fail in general to reproduce the vertical gradients obtained by the 3-D models, presumably because they do not account adequately for deep convection.

Four models (two 3-D and two 2-D) participated in an intercomparison of ^{210}Pb aerosol simulations. The global ^{210}Pb inventories simulated by the models tended to be higher than observed, which could indicate insufficient rates of aerosol scavenging by precipitation. There are however substantial uncertainties in the inventories derived from observations.

- 18 -

APPENDIX: DESCRIPTION OF PARTICIPATING MODELS.

A. NCAR CCM2: A 3-D model using instantaneous meteorological fields (with a time step of 15 minutes) from the standard version of the CCM2 [Hack, 1993; Hack et al., 1993, 1994]. Horizontal resolution: 2.8 degrees longitude by 2.8 degrees latitude. Vertical resolution: 18 layers up to 5 mb, with 11 in the troposphere. Convective mass fluxes are calculated as described in Hack [1994]. The scheme adjusts the moist static energy over three adjacent layers, allowing for entrainment in the bottom layer, condensation and rainout in the middle layer, and detrainment in the upper layer. The method is applied sequentially, beginning at the surface, until all of the tropospheric levels have

been adjusted. The conservative convective transport of trace constituents is also treated according to this vertical mass exchange. Resolved scale transport is performed using a shape preserving semi-Lagrangian transport algorithm [Rasch, 1990]. A "non-local" boundary layer parameterization [Holtslag and Boville, 1993] diagnoses a boundary layer depth and determines diffusivity profiles and non-local turbulent transports of heat and constituents within the boundary layer. These algorithms have been used in a variety of chemical transport studies [i.e., Rasch et al., 1994, 1995; Hartley et al., 1994].

B. ECHAM3. An atmospheric general circulation model developed for climate studies [Roeckner et al., 1992]. Prognostic variables: Vorticity, divergence, temperature, surface pressure, water vapor, cloud water, turbulent kinetic energy, chemical species. Horizontal advection: spectral transform (vorticity, divergence, temperature, surface pressure) with triangular truncation (T21). Nonlinear and physical terms are calculated on a Gaussian grid (5.6°x5.6°). Vertical resolution: 19 levels up to 10 hPa. Model time-step: 40 minutes. Water vapor, cloud water and chemicals are treated by a semi-Lagrangian method [Rasch and Williamson, 1990]. Boundary layer: surface fluxes of momentum, heat, moisture and chemical tracers are calculated from Monin-Obukhov theory. Within the boundary layer and also in the free atmosphere, turbulent transfer is calculated on the basis of a higher-order closure scheme. Mass flux scheme for penetrative, shallow and mid-level convection is from Tiedtke [1989]. The scheme considers convective transport of heat, moisture, cloud water, chemicals and momentum in downdrafts and updrafts. The model has been used in many climate sensitivity experiments [Cess et al., 1990; Cubasch et al., 1992; Roeckner et al., 1994], tracer transport [Brost et al.,1991; Feichter et al., 1991a,b] and tropospheric chemistry studies [Roelofs and Lelieveld, 1995; Feichter et al., 1995].

C. GFDL/ZODIAC. A 3-D model using 6-hour time-average meteorological fields from a Geophysical Fluid Dynamics Laboratory GCM [Manabe et al., 1974]. Horizontal

resolution: ~265 km. Vertical resolution: 11 levels up to 10 mb, with 6-7 in troposphere. Vertical transport by dry and moist convective processes is parameterized in terms of a Richardson number diffusion. The model has been used in many tracer transport studies [Mahlman and Moxim, 1978; Levy et al., 1985; Levy and Moxim, 1989; Kasibhatla et al., 1991, 1993].

D. GISS/H/I. A 3-D model using 4-hour time-average meteorological fields from the Goddard Institute of Space Studies GCM 2 [Hansen et al., 1983]. Horizontal resolution: 4° latitude x 5° longitude. Vertical resolution: 9 layers up to 10 mb, with 7-8 in troposphere (sigma coordinate). Convective mass fluxes are diagnosed from the GCM. Wet removal of soluble tracers includes both scavenging in convective updrafts and first-order rainout and washout in large-scale precipitation, as described by Balkanski et al. [1993]. The GISS/H/I model has been used in many tropospheric chemistry studies (for example Prather et al. [1987], Spivakovsky et al. [1990], Jacob et al. [1993], Chin and Jacob [1995]).

E. KNMI-TM2 A 3-D model based on the TM2 model of Heimann [1989] and the GISS model of Hansen et al. [1983]. The transport model uses meteorological information obtained from the ECMWF forecast model. From analyzed data (wind, temperature, geopotential height and humidity) collected every 6 or 12 hours, the horizontal and vertical transport of air mass is calculated. The ECMWF data are analyzed at 14 standard pressure levels (1000, 850, 700, 500, 400, 300, 250, 200, 150, 100, 70, 50, 30 and 10 hPa) on a horizontal scale of 2.5°x2.5°. The transport model KNMI-TM2 has a resolution of 5°x4° and 15 sigma levels in the vertical (up to approximately 30 km altitude). Advection of trace gases in KNMI-TM2 is calculated by the slopes scheme of Russell and Lerner [1981], which is modified in order to avoid negative concentrations. Cumulus convection is parameterized according to the mass-flux scheme of Tiedke [1989]. In this scheme the humidity convergence, obtained from ECMWF data, determines the upward

mass-flux. The parcel buoyancy determines the height of the convective transport in the model column. Turbulent transport in the boundary layer is parameterized using the Richardson number [Louis, 1979], obtained from ECMWF data. For this WCRP exercise we use ECMWF fields for June-August 1989 and December-February 1989-1990, analyzed every 12 hours.

F. LLNL/GRANTOUR. The GRANTOUR model [Walton et al. 1988] is a 3-D model using 12-hour time-averaged meteorological fields from the National Center for Atmospheric Research CCM1 GCM [Williamson et al., 1987]. Resolution: 50,000 constant-mass air parcels whose dimensions average 100 mb x 330 km x 330 km. Parcel information is periodically mapped to the CCM1 grid which has resolution of 4.4° latitude x 7.5° longitude x 12 vertical layers up to 10 mb with 8-9 layers in the troposphere. Convective mass fluxes are diagnosed from the CCM1 GCM. Advection is by a non-diffusive Lagrangian scheme. Mixing ratio changes due to both diffusion and convection are calculated on the CCM1 fixed grid and then mapped to the parcels. Wet scavenging is proportional to the precipitation rate obtained from the CCM1 with a large scale scavenging coefficient of 2 cm^{-1} and convective scavenging coefficient of 0.6 cm^{-1}. The GRANTOUR model has been used in many tropospheric chemistry studies (for example Ghan et al. [1988]; Erickson et al. [1991]; Penner et al. [1991ab, 1993, 1994]). The simulations reported here are fully documented by Dignon [1993].

G. LLNL/E. A 3-D model identical to LLNL/GRANTOUR except that the atmosphere is discretized solely by the Eulerian grid used in the CCM1 (no constant-mass air parcels are used). A second-order diffusion-limited Van Leer advection scheme is used. Diffusion, convection and scavenging have all been included in this new model. The simulations reported here are fully documented by Bergmann et al. [1994].

H. LMD. A 3-D tracer model implemented in-line within the Laboratoire de Météorologie Dynamique (CNRS, Paris) GCM [Sadourny and Laval, 1984]. Horizontal

grid is linear in longitude (5.6° resolution) and in sine of latitude (3.6° mean resolution). Vertical resolution: 4 levels in the boundary layer, 4 in the troposphere and 3 in the stratosphere. GCM-triggered dry and moist convections induce uniform vertical tracer mixing within the unstable layers and over a GCM-selected fraction of the column horizontal section. Vertical tracer diffusion in the boundary layer is parameterized using GCM-calculated diffusion coefficients. The LMD tracers/climate model is fully described in two recently published studies of ^{222}Rn, ^{210}Pb and other tracers [Genthon and Armengaud, 1995ab].

I. TM2Z. A 3-D model using 12-hour instantaneous meteorological fields analyzed by the ECMWF for the year 1990. The model is a new version of the TM1 model developed by Heimann and Keeling [1989] . Horizontal resolution: 2.5°x2.5°. Vertical resolution: 9 layers up to 10 mb, with 7-8 in troposphere. Convective mass fluxes are calculated using the cloud mass flux scheme of Tiedtke [1989] . Turbulent vertical transport is calculated based on the stability of the air using the scheme of Louis [1979] . The implementation of these schemes in the transport model is described by Heimann [1994] . The TM2Z model has been used to simulate ^{222}Rn and CO_2 concentrations [Ramonet, 1994; Ramonet et al., 1995].

J. MOGUNTIA. The MOGUNTIA model [Zimmermann, 1988; Zimmermann et al., 1989] has been designed to numerically simulate the transport of trace constituents and the background photochemistry of the global troposphere and lower stratosphere. Grid resolution is 10°x10° x100 hPa. The large-scale transport is based on observed monthly mean temperature and wind fields. Turbulent diffusion is parameterized proportional to the day-by-day deviation of the winds. Deep convection is performed explicitly according to observational occurrence of cumulus clouds [Feichter and Crutzen, 1990].

k. CCCA-GCM. A 3-D climate GCM producing dynamical and tracer fields every 15 minutes. The model uses spectral transport with a horizontal resolution of 32

wavenumbers and a vertical resolution of 10 levels up to 10mb, with 6-7 levels in the troposphere. Convective transport and PBL mixing are parameterized. The convective tracer transport occurs for moist and dry events using a diffusive mixing associated with the convective adjustment scheme of the model. The degree of mixing is dependent upon the local strength of the convective column instability. The GCM is the second generation CCCA-GCM [McFarlane et al., 1992], an established climate simulation model, which was modified to include ^{222}Rn and ^{210}Pb tracers in a developmental form.

m. LaRC. The LaRC general circulation model is a 3-D, sigma coordinate, quasi-spectral, primitive equation formulation [Grose et al., 1987; Pierce et al., 1993]. It has 34 levels in the vertical, spanning the region from the Earth's surface to approximately 95-km altitude. The levels are spaced about 100 mb apart from the Earth's surface to about 200 mb. Above 200 mb, they are spaced about 3-km apart. A semi-implicit integration technique is used with a 15-minute time step. A 1-2-1 time filter is applied every sixth time step to control time splitting. Orographic forcing is approximated by using a smoothed spherical harmonic representation of the Earth's topography. Throughout the model atmosphere a biharmonic diffusion is applied to the vorticity, divergence, and temperature prognostics. In the equatorial upper troposphere an additional linear damping term is incorporated to parameterize the effects of "cumulus" friction. A surface drag proportional to the wind speed is applied in the lowest model level. Vertical diffusion of momentum and temperature are incorporated via a non-linear, time-split technique. Above 55-km altitude, a Rayleigh friction term is applied to vorticity and divergence, increasing to a peak damping time of 0.4 days at the top model level. Above about 100 mb, a radiative transfer scheme is used that incorporates the effects of absorption of UV radiation by O_2 and O_3 and the infrared contribution of CO_2, O_3, and H_2O. Diabatic heating in the troposphere is parameterized by a 2-term Taylor's series "type" expansion which incorporates observed heating rates and climatological temperature distributions.

n. LLNL/IMPACT. A 3-D model using 6 hour meteorological fields from the tropospheric data assimilation model of the Data Assimilation Office at NASA/Goddard. Horizontal resolution is 2°x2.5°. Vertical resolution is 20 layers, to 10 mb. At the time of this simulation, the 3-D model was very much under development. Most important to this simulation, the model did not have any convective transport mechanism, making ^{222}Rn simulations difficult. LLNL/IMPACT has since undergone upgrades and is now better able to perform simulations such as these.

o. MRI. A 3-D semi-Lagrangian transport model using 2-hourly meteorological fields from the MRI global spectral atmospheric circulation model [Shibata and Chiba, 1990]. Spectral horizontal resolution is R24 and vertical resolution is 23 levels up to 0.05 hPa. Mixing of tracer in PBL is parameterized by using the scheme of Louis (1979). Convective transport is not included.

p. TOMCAT. A 3-D model using 6-hourly meteorological fields from the UGAMP GCM (see model q). Horizontal resolution: 2.8° latitude x 2.8° longitude. Vertical resolution: 19 levels up to 10mb. Tracer transport is performed using the second-order-moments scheme of Prather [1986]. TOMCAT was developed at Météo France, Toulouse and University of Cambridge. The model has been used in many stratospheric chemistry studies [e.g. Chipperfield et al., 1993, 1994, 1995]. and is being developed for tropospheric studies. For the experiments described in this paper the TOMCAT runs did not contain any tracer transport other than advection. Since the WCRP workshop treatments of convection [Tiedtke 1989] and vertical turbulent diffusion [Louis 1979] have been added to the model.

q. UGAMP. A 3-D spectral general circulation model derived from Cycle 27 of the ECMWF model [ECMWF Research Manual 2]. Spectral horizontal resolution: T42 [Simmons et al., 1988]. Chemical tendencies and parameterized physical processes are resolved on a Gaussian grid: 2.8° latitude x 2.8° longitude [Tiedtke et al. 1988]. Vertical

resolution: 19 hybrid levels up to 10mb. Planetary boundary layer modeled explicitly using 5 model levels and a 30-minute time step. Morcrette [1990] radiation scheme. Fourth-order Total Variation Diminishing (TVD) vertical advection [Thuburn 1993]. Betts-Miller convective adjustment scheme for moisture [Betts 1986; Betts & Miller 1993]. No convective transport of tracers.

R. AER A 2-D model using the diabatic circulation based on calculated heating rates and a horizontal eddy diffusion coefficient function of latitude, altitude, and season. Horizontal resolution: 9.5°. Vertical resolution: ~3.5-km up to 60-km. The model with full photochemistry module has been used in many stratospheric chemistry studies (for example Ko et al. [1984, 1985, 1986, 1989, 1991]; Sze et al. [1989]; Rodriguez et al. [1991]; Weisenstein et al. [1991, 1992]; Plumb and Ko [1992]).

S. UCAMB. A 2-D classical Eulerian model. Eddy diffusion coefficients are specified and the mean circulation is calculated, based on forcing by latent and radiative heating and eddy transport processes. This gives updated fields of temperature and velocity every 4 hours. There is additional vertical mixing in the model if air becomes unstable with respect to the dry adiabat. A full description of the model formulation and tropospheric chemistry is given in Harwood and Pyle [1980] and Law and Pyle [1993]. Horizontal resolution: 9.5°. Vertical resolution: ~3.5 km up to 60-km. Treatments of dry and wet deposition are included in the model. The latter is modeled simply as the reciprocal of the lifetime (with respect to rainout) following Logan et al. [1981]. The model has been used in tropospheric chemistry studies (e.g. Law and Pyle [1993], Bekki et al, [1994]).

T. HARWELL. A 2-D zonally averaged model with 12 vertical layers, each of 2-km height, and 24 equal-area latitudinal bands. The model uses circulation derived by Plumb and Mahlman [1987], who used the output from a 3-D GCM [Mahlman et al., 1980] to derive a mean meridional circulation and a tensor describing the eddy motions present in this zonal flow. The rainfall in each grid cell is set as a smooth function of the

local relative humidity and the wet removal of a soluble aerosol is calculated as a function of this removal of the water vapor. The water or soluble species removed from a given cell is transported to the cell immediately below, giving the potential for re-evaporation, except for the lowest layer when it appears as rain or wet deposition at the surface. The differential equations are solved employing the FACSIMILE integration package [Curtis and Sweetenham, 1987], which uses a variable order Gear's method. The transport has been tested by comparison with observations of the atmospheric tracers ^{85}Kr, $CFCl_3$ and CF_2Cl_2 [Hough, 1989] and, with the inclusion of a chemical mechanism, comparison with observations of CH_4, CO, non-methane hydrocarbons, O_3, peroxy-acetylnitrate (PAN), and peroxides [Hough, 1991; Hough and Derwent, 1990; Hough and Johnson, 1991; Johnson et al, 1992].

U. UW. The University of Washington 2-D chemical transport model has been developed by Tung, Yang, and Olaguer [Tung, 1982, 1986; Yang et al., 1990, 1991; Olaguer et al., 1991]. Formulated in isentropic coordinates, the model is run with 18 latitudinal bands each 10° wide. There are 48 levels vertically from 0 to 54-km. Eight of these levels are below 100 mb (average pressures are approximately 880, 670, 500, 370, 280, 230, 180, and 140 mb). Transport parameters derived from observed 1980 atmospheric temperatures are used. Recently, the model has been validated using tracers which are sensitive to tropospheric transport and chemical parameters. In the work of Brown [1993], model simulations of ^{85}Kr, CFC-11, CFC-12, and methylchloroform are shown to be in good agreement with observations. The distribution of ^{222}Rn in the troposphere is sensitive to the vertical diffusion parameter K_{zz}. Values of K_{zz} used here are 50 m^2 s^{-1} in the tropics and 10 m^2 s^{-1} at higher latitudes. These values are the same as those used by Brown [1993] and are consistent with those discussed in the works of Plumb and McConalogue [1988] and Plumb and Mahlman [1987].

REFERENCES.

Allen, D.J, R.B. Rood, A.M. Thompson, and R.D. Hudson, Three-dimensional Rn-222 calculations using assimilated meteorological data and a convective mixing algorithm, submitted to *J. Geophys. Res.*

Balkanski, Y.J., and D.J. Jacob, Transport of continental air to the subantarctic Indian Ocean, *Tellus 42B*, 62-75, 1990.

Balkanski, Y.J., D.J. Jacob, R. Arimoto, and M.A. Kritz, Long-range transport of radon-222 over the North Pacific Ocean: implications for continental influence, *J. Atmos. Chem.*, *14* 353-374, 1992.

Balkanski, Y.J., D.J. Jacob, G.M. Gardner, W.M. Graustein, and K.K. Turekian, Transport and residence times of continental aerosols inferred from a global 3-dimensional simulation of ^{210}Pb, *J. Geophys. Res.*, *98*, 20573-20586, 1993.

Bekki, S., K.S. Law, and J.A. Pyle, Effect of ozone depletion on atmospheric CH_4 and CO concentrations, *Nature*, *371*, 595-597, 1994.

Bergmann, D., J. Dignon, J. Penner, and J. Walton, Results from the LLNL Eulerian Grantour Model for the WCRP '93 Workshop on the Parameterization of Sub-Grid Scale Tracer Transport, Virginia Beach, VA. LLNL report UCRL-ID 116544, 1994.

Betts, A. K., A New Convective Adjustment Scheme. Part I: Observational and theoretical basis, *Q. J. R. Meteorol. Soc.*, *112*, 677-691, 1986.

Betts, A. K., and M.J. Miller, The Betts-Miller Scheme, in *The Representation of Cumulus Convection in Numerical Models of the Atmosphere*, eds. K. Emmanuel and D. Raymond, American Meteorological Society, 1993.

Brost, R. A. and R. B. Chatfield, Transport of radon in a three-dimensional, subhemispheric model, *J. Geophys. Res.*, *94*, 5095-5120, 1989.

Brost R. A., J. Feichter, and M. Heimann, Three-dimensional simulation of ^{7}Be in a global climate model, *J. Geophys. Res.*, *96*, 22423-22445, 1991.

Brown, M., Deduction of emissions of source gases using an objective inversion algorithm and a chemical transport model, *J. Geophys. Res.*, *98*, 12639-12660, 1993.

Cess, R.D., et al., Intercomparison and interpretation of climate feedback processes in 19 atmospheric general circulation models, *J. Geophys. Res.*, *95*, 16601-16615, 1990.

Cubasch, U., K. Hasselmann, H. Hoeck, E. Maier-Reimer, U. Mikolajewicz, B. D. Santer, and R. Sausen, Time-dependent greenhouse warming computations with a coupled ocean-atmosphere model, *Clim. Dyn.*, *8*, 55-69, 1992.

Carroll, M.A., and A.M. Thompson, NO_x in the non-urban troposphere, in *Advances in Physical Chemistry*, ed. J. Barker, World Scientific Publishing Com., 1995 (in press).

Chin, M., and D.J. Jacob, Anthropogenic and natural contributions to atmospheric sulfate: a global model analysis, submitted to *J. Geophys. Res.*, 1995.

Chipperfield, M.P., D. Cariolle, P. Simon, R. Ramaroson, and D.J. Lary, A three-dimensional modeling study of trace species in the Arctic lower stratosphere during winter 1989-1990, *J. Geophys. Res.*, *98*, 7199-7218, 1993.

Chipperfield, M.P., D. Cariolle, and P.Simon, A 3-D chemical transport model study of chlorine activation during EASOE, *Geophys. Res. Lett.*, *21*, 1467-1470, 1994.

Chipperfield, M.P., J.A. Pyle, C.E. Blom, N. Glatthor, M. Hopfner, T. Gulde, C. Piesch, and P. Simon,

The Variability of ClONO$_2$ and HNO$_3$ in the Arctic Polar Vortex: Comparison of Transall MIPAS measurements and 3-D Model Results, *J. Geophys. Res.*, *100*, 9115-9129, 1995.

Curtis, A.R., and W.P. Sweetenham, FACSIMILE/CHEKMAT user's manual, AERE-R12805, HMSO, London.

Dickerson, R.R., and 15 others, Thunderstorms: an important mechanism in the transport of air pollutants, *Science*, *235*, 460-465, 1987.

Dignon, J., The WCRP '93 Workshop on the Parameterization of Sub-Grid Scale Tracer Transport: Results from the LLNL GRANTOUR Model. LLNL report UCRL-ID-115607, 1993.

Erickson III, D.J., J.J. Walton, S.J. Ghan, and J.E. Penner, Three-dimensional modeling of the global atmospheric sulfur cycle: A first step, *Atmos. Environ.*, *25A*, 2513-2520, 1991.

European Center for Medium-Range Weather Forecasting, Research Manual 2. ECMWF Forecast Models Adiabatic Part, ECMWF Research Department, 1988.

Feichter, J., and P.J. Crutzen, Parameterization of vertical tracer transport due to deep cumulus convection and its evaluation with ^{222}Radon measurements, *Tellus*, *42B*, 100-117, 1990.

Feichter, J., R. A. Brost, and M. Heimann, Three-dimensional modeling of the concentration and deposition of ^{210}Pb aerosols, *J. Geophys. Res.*, *96*, 22447-22469, 1991a.

Feichter, J., E. Roeckner, U. Schlese, and M. Windelband, Tracer transport in the Hamburg climate model, in *Air Pollution Modeling and Its Applications VIII*, eds. H. van Dop and D. G. Steyn, Plenum Press, New York, 1991b.

Feichter J., E. Kjellstrom, H. Rodhe, F. Dentener, J. Lelieveld, and G.-J Roelofs, Simulation of the tropospheric sulfur cycle in a global climate model, submitted to *Atmos. Environ.*, 1995.

Fukuda, K., and S. Tsunogai, Pb-210 in precipitation in Japan and its implication for the transport of continental aerosols across the ocean, *Tellus*, *27*, 514-521, 1975.

Genthon C., and A. Armengaud, Radon 222 as a comparative tracer of transport and mixing in two general circulation models of the atmosphere, *J. Geophys. Res.*, *100*, 2849-2866, 1995a.

Genthon C., and A. Armengaud, GCM simulations of atmospheric tracers in the polar regions: South Pole (Antarctica) and Summit (Greenland) cases, *Sci. Total Environ. 160/161*, 101-116, 1995b.

Gesell, T.F., Background atmospheric ^{222}Rn concentrations outdoors and indoors: a review, *Health Physics*, *45*, 289-302, 1983.

Ghan, S.J., M.C. MacCracken, and J.J. Walton, Climatic Response to Large Atmospheric Smoke Injections: Sensitivity Studies with a Tropospheric General Circulation Model, *J. Geophys. Res.*, *93*, 8315-8337, 1988.

Giorgi, F. and Chameides, W.L., The rainout parameterization in a photochemical model, *J. Geophys. Res.*, *90*, 7872-7880, 1985.

Giorgi, F., and W.L. Chameides, Rainout lifetimes of highly soluble aerosols and gases as inferred from simulation with a general circulation model, *J. Geophys. Res.*, *91*, 14,367-14,376, 1986.

Gold, S., H. Barkhau, W. Shleien, and B. Kahn, Measurement of naturally occurring radionuclides in air, in *The Natural Radiation Environment*, eds. J.A.S. Adams and W.M. Lowder, University of Chicago Press, 369-382, 1964.

Graustein, W. C. and Turekian, K.K., Radon fluxes from soils to the atmosphere measured by 210Pb - 226Ra disequilibrium in soils, *Geophys. Res. Lett.*, *17*, 841-844, 1990.

Grose, W.L., J.E. Nealy, R.E. Turner, and W.T. Blackshear, Modeling the transport of chemically active constituents in the stratosphere, in *Transport Processes in the Middle Atmosphere*, ed. by G. Visconti, Reidel, 485 pp., 1987.

Hack, J.J., Parameterization of moist convection in the NCAR Community Climate Model, CCM2, *J. Geophys. Res., 98*, 5551--5568, 1993.

Hack, J.J., B.A. Boville, J.T. Kiehl, P.J. Rasch, and D.L. Williamson, Climate statistics from the NCAR Community Climate Model CCM2, *J. Geophys. Res., 99*, 20,785-20,813, 1994.

Hack, J.J., B.A. Boville, B.P. Briegleb, J.T. Kiehl, P.J. Rasch, and D.L. Williamson, Description of the NCAR Community Climate Model (CCM2) NCAR Tech. Note, NCAR/TN--382+STR, Boulder, Colo., 108 pp., 1993.

Hansen, J., G. Russell, D. Rind, P. Stone, A. Lacis, S. Lebedeff, R. Ruedy, and L. Travis, Efficient three-dimensional global models for climate studies: models I and II, *Mon. Weath. Rev., 111*, 609-662, 1983.

Hartley, D., D.L. Williamson, P.J. Rasch, and R. Prinn, Examination of tracer transport in the NCAR CCM2 by comparison of $CFCl_3$ simulations with ALE/GAGE Observations, *J. Geophys. Res., 99*, 12885-12896, 1994.

Harwood, R.S., and J.A. Pyle, The dynamical behavior of a two--dimensional model of the stratosphere, *Q. J. Roy. Meteorol. Soc., 106*, 395-420, 1980.

Heimann, M., The global atmospheric tracer model TM2: model description and user manual, Max-Planck-Institut fur Meteorologie, 1994.

Heimann, M., and C.D. Keeling, A three-dimensional transport model for atmospheric CO_2: 2. Model description and simulated tracer experiments. Report No. 33, Hamburg: Max-Planck-Institut fur Meteorologie, 105 pp., 1989.

Heimann, M., P. Monfray, and G. Polian, Modeling the long-range transport of [222]Rn to subantarctic and antarctic areas, *Tellus, 42B*, 83-99, 1990.

Holtslag, A.A.M., and B.A. Boville, Local versus non-local boundary-layer diffusion in a global climate model, *J. Clim., 6*, 1825--1842, 1993.

Hough, A.M., The development of a two-dimensional global tropospheric model- 1. The model transport, *Atmos. Environ, 23*, 1235-1261, 1989.

Hough, A.M., Development of a two-dimensional global tropospheric model: Model chemistry, *J. Geophys. Res, 96*, 7325-7362, 1991.

Hough, A.M., and R.G. Derwent, Changes in the global concentration of tropospheric ozone due to human activities, *Nature, 344*, 645-650, 1990.

Hough, A.M., and C.E. Johnson, Modelling the role of nitrogen oxides, hydrocarbons and carbon monoxide in the global formation of tropospheric oxidants, *Atmos. Environ, 25*, 1819-1835, 1991.

Intergovernmental Panel for Climate Change, *Climate Change 1992*, ed. by J.T. Houghton, B.A. Callander, and S.K. Varney, WMO/UNEP, Cambridge University Press, Cambridge, UK, 1994.

Intergovernmental Panel for Climate Change, *Climate Change*, ed. by J.T. Houghton, G.J. Jenkins, and J.J. Ephraums, WMO/UNEP, Cambridge University Press, Cambridge, UK, 1994.

Jacob, D.J., and M.J. Prather, Radon-222 as a test of boundary layer convection in a general circulation model, *Tellus, 42B*, 118-134, 1990.

Jacob, D.J., J.A. Logan, R.M. Yevich, G.M. Gardner, C.M. Spivakovsky, S.C. Wofsy, J.W. Munger, S. Sillman, M.J. Prather, M.O. Rodgers, H. Westberg, and P. R. Zimmerman, Simulation of summertime ozone over North America, *J. Geophys. Res.*, *98*, 14797-14816, 1993.

Johnson C., J. Henshaw, and G. McInnes, Impact of aircraft and surface emissions of nitrogen oxides on tropospheric ozone and global warming, *Nature*, *355*, 69-71, 1992.

Kasibhatla, P.S., H. Levy, W.J. Moxim, and W.L. Chameides, The relative importance of stratospheric photochemical production on tropospheric NO_y levels: a model study, *J. Geophys. Res.*, *96*, 18631-18646, 1991.

Kasibhatla, P.S., H. Levy II, and W.J. Moxim, Global NO_x, HNO_3, PAN, and NO_y distributions from fossil-fuel combustion emissions: a model study, *J. Geophys. Res.*, *98*, 7165-7181, 1993.

Ko, M.K.W., N.D. Sze, M. Livshits, M.B. McElroy, and J.A. Pyle, The seasonal and latitudinal behavior of trace gases and O_3 as simulated by a two-dimensional model of the atmosphere, *J. Atmos. Sci.*, *41*, 2381-2408, 1984.

Ko, M.K.W., K.K. Tung, D.K. Weisenstein, and N.D. Sze, A zonal mean model of stratospheric tracer transport in isentropic coordinates: Numerical simulation for nitrous oxide and nitric acid, *J. Geophys. Res.*, *90*, 2313-2329, 1985.

Ko, M.K.W., M.B. McElroy, D.K. Weisenstein, and N.D. Sze, Lightning: A possible source of stratospheric odd nitrogen, *J. Geophys. Res.*, *91*, 5395-5404, 1986.

Ko, M.K.W., N.D. Sze, and D.K. Weisenstein, The roles of dynamical and chemical processes in determining the stratospheric concentration of ozone in one-dimensional and two-dimensional models, *J. Geophys. Res.*, *94*, 9889-9896, 1989.

Ko, M.K.W., N.D. Sze, and D.K. Weisenstein, Use of satellite data to constrain model calculated atmospheric lifetimes for N2O: Implications for other trace gases, *J. Geophys. Res.*, *96*, 7547-7552, 1991.

Koch, D.M., D.J. Jacob, and W.C. Graustein, Vertical transport of aerosols in the troposphere as indicated by ^{7}Be and ^{10} ^{210}Pb in a chemical tracer model, submitted to *J. Geophys. Res.*

Kritz, M.A., J-C. Le Roulley, and E.F. Danielsen, The China Clipper. Fast advective transport of radon rich air from the Asian boundary layer to the upper troposphere near California, *Tellus*, *42B*, 46-61, 1990.

Lambert, G., G. Polian, and D. Taupin, Existence of periodicity in radon concentrations and the large-scale circulation at latitudes between 40° and 70° South, *J. Geophys. Res.*, *75*, 2341-2345, 1970.

Lambert, G., G. Polian, J. Sanak, B. Ardouin, A. Buisson, A. Jegou and J. C. Leroulley, Cycle du radon et de ses descendants: application à l'étude des échanges troposphère-stratosphère, *Ann. Geophys.*, *38*, 497-531, 1982.

Lambert, G., J.-C. Le Roulley, and M. Kritz, Box models for radon transfers into the stratosphere, *Tellus*, *42B*, 135-141, 1990.

Law, K.S., and J.A. Pyle, Modelling Budgets of Tropospheric Trace Gases. I : Ozone and Odd Nitrogen, *J. Geophys. Res.*, *98*, 18,377-18400, 1993.

Levy, H. II, J.D. Mahlman, W.J. Moxim, and S.C. Liu, Tropospheric ozone: the role of transport, *J. Geophys. Res.*, *90*, 3753-3772, 1985.

Levy II, H., and W.J. Moxim, Simulated global distribution and deposition of reactive nitrogen emitted by fossil fuel combustion, *Tellus*, *41*, 256-271, 1989.

Liu, S.C., McAfee, J.R., and Cicerone, R.J., Radon 222 and tropospheric vertical transport, *J. Geophys.*

Res., *89*, 7291-7297, 1984.

Logan J.A., M.J. Prather, S.C. Wofsy, and M.B. McElroy, Tropospheric chemistry: A global perspective, *J. Geophys. Res.*, *86*, 7210-7254, 1981.

Louis, J. F., A parametric model of vertical eddy fluxes in the atmosphere, *Boundary-Layer Meteor. 17*, 187-202, 1979.

Mahlman, J.D., and W.J. Moxim, Tracer simulation using a general circulation model: Results from a midlatitude source experiment, *J. Atmos. Sci.*, *35*, 1340-1374, 1978.

Mahlman, J.D., H. Levy, and W.J. Moxim, Three-dimensional tracer structure and behavior as simulated in two ozone precursor experiments, *J. Atmos. Sci.*, *37*, 655-685, 1980.

Mahowald, N.M., P.J. Rasch, and R.G. Prinn, Cumulus parameterizations in chemical transport models, *J. Geophys. Res.*, in press.

Manabe, S., D.G. Hahn, and J.L. Holloway, Jr., The seasonal variation of the tropical circulation as simulated by a global model of the atmosphere, *J. Atmos. Sci.*, *31*, 43-83, 1974.

McFarlane, N.A. G.J.Boer, J.-P. Blanchet, and M. Lazare, The Canadian Climate Centre second generation GCM and its equilibrium climate, *J. Clim.*, *5*, 1013-1044, 1992.

Miller, J.M., J.L. Moody, J.M. Harris, and A. Gaudry, A 10-year trajectory flow climatology for Amsterdam Island, 1980-1989, *Atmos. Environ.*, *27A*, 1909-1916, 1993.

Morcrette, J-J., Impact of changes to the radiation transfer parametrization plus cloud optical properties in the ECMWF model, *Mon. Weath. Rev.*, *118*, 847-873, 1990.

Moses, H., A.F. Stehney, and H.F. Lucas, Jr., The effect of meteorological variables upon the vertical and temporal distributions of atmospheric radon, *J. Geophys. Res.*, *65*, 1223-1238, 1960.

Nazaroff, W.W., Radon transport from soil to air, *Rev. Geophys.*, *30*, 137-160, 1992.

Nazarov, L.E., A.F. Kuzenkov, S.G. Malakhov, L.A. Volokitina, Ya.I. Gasiyev, and A.S. Vasil'yev, Radioactive aerosol distribution in the middle and upper troposphere over the USSR in 1963-1968, *J. Geophys. Res.*, *75*, 3575-3588, 1970.

Olaguer, E.P., H. Yang, and K.K. Tung, A reexamination of the radiative balance of the stratosphere, *J. Atmos. Sci.*, *49*, 1242-1263, 1992.

Penner, J.E., C.S. Atherton, J. Dignon, S.J. Ghan, J.J. Walton, and S. Hameed, Tropospheric nitrogen: A three-dimensional study of sources, distribution, and deposition, *J. Geophys. Res.*, *96JfR 959-990, 1991a*.

Penner, J.E., S.J. Ghan, and J.J. Walton, The role of biomass burning in the budget and cycle of carbonaceous soot aerosols and their climate impact, in Global Biomass Burning, ed. by J. Levine, MIT press, Cambridge, MA, 387-393, 1991b.

Penner, J.E., C.A. Atherton, and T. Graedel, Global emissions and models of photochemically active compounds, in *Global Atmospheric-Biospheric Chemistry*, ed. R. Prinn, Plenum Publishing, N.Y., 223-248, 1994.

Penner, J.E., H. Eddleman and T. Novakov, Towards the development of a global inventory of black carbon emissions, *Atmos. Environ.*, *27A*, 1277-1295, 1993.

Pereira, E.B., Radon-222 time series measurements in the Antarctic peninsula (1986-1987), *Tellus 42B*, 39-45, 1990.

Pickering, K.E., et al., Convective transport of biomass burning emissions over Brazil during TRACE-A,

submitted to *J. Geophys. Res.*, 1995.

Pierce, R.B., W.T. Blackshear, T.D. Fairlie, W.L. Grose, and R.E. Turner, The interaction of radiative and dynamical processes during a simulated sudden stratospheric warming, *J. Atmos. Sci.*, *50*, 3829-3851, 1993.

Plumb, R.A., and J.D. Mahlman, The zonally-averaged transport characteristics of the GFDL general circulation/transport model, *J. Atmos. Sci.*, *44*, 298-327, 1987.

Plumb, R.A., and D.D. McConalogue, On the meridional structure of long lived tropospheric constituents, *J. Geophys. Res.*, *93*, 15897-15913, 1988.

Plumb, R.A., and M.K.W. Ko, Interrelationships between mixing ratios of long-lived stratospheric constituents, *J. Geophys. Res.*, *97*, 10,145-10,156, 1992.

Polian, G., G. Lambert, B. Ardouin, and A. Jegou, Long-range transport of radon in subantarctic and antarctic areas, Tellus, 38B, 178-189, 1986.

Prather, M.J., M.B. McElroy, S.C. Wofsy, G. Russell, and D. Rind, Chemistry of the global troposphere: fluorocarbons as tracers of air motion, *J. Geophys. Res.*, *92*, 6579-6613, 1987.

Ramonet M., Variabilite du CO_2 atmosph   erique en regions australes: comparaison modele-mesures, Thesis, University of Paris 7, 295 pp., 1994.

Ramonet M., J.C. Le Roulley, P. Bousquet, and P. Monfray, Radon-222 measurements during the TROPOZ II campaign and comparison with a global atmospheric transport model, *J. Atmos. Chem.*, in press, 1995.

Rasch, P, and D. Williamson, Computational aspects of moisture transport in global models of the atmosphere, *Q. J. R. Meteorol. Soc.*, *116*, 1071-1090, 1990.

Rasch, P.J., X.X. Tie, B.A. Boville, and D.L. Williamson, A three-dimensional transport Model for the stratosphere, *J. Geophys. Res.*, *99*, 999-1018, 1994.

Rasch, P.J., B.A. Boville, and G.P. Brasseur, A three-dimensional general circulation model with coupled chemistry for the middle atmosphere, *J. Geophys. Res.*, *100*, 9041-9071, 1995.

Rind, D., and J. Lerner, The use of on-line tracers as a diagnostic tool in GCM model development, submitted to *J. Geophys. Res.*, 1995.

Rodriguez, J.M., M.K.W. Ko, and N.D. Sze, Role of heterogeneous conversion of N2O5 on sulphate aerosols in global ozone losses, *Nature*, *352*, 134-137, 1991.

Roeckner E., K. Arpe, L. Bengtsson, S. Brinkop, L. D=FCmenil, M. Esch, E. Kirk, F. Lunkeit, M. Ponater, B. Rockel, R. Sausen, U. Schlese, S. Schubert, and M. Windelband, Simulation of the present-day climate with the ECHAM model: Impact of model physics and resolution, Rep. No. 93, Max-Planck-Institute for Meteorology, Hamburg, Germany, 1992.

Roeckner, E., T. Siebert and J. Feichter, Climatic response to anthropogenic sulfate forcing simulated with a general circulation model, in *Aerosol Forcing of Climate*, eds. R.J. Charlson and J. Heintzenberg, Wiley, 1995.

Roelofs, G.-J., and J. Lelieveld, Distribution and budget of O_3 in the troposphere calculated with a chemistry-general circulation model, submitted to *J. Geophys. Res.*, 1995.

Russell, G.L., and J.A. Lerner, A new finite-differencing scheme for the tracer transport equation, *J. Appl. Meteor. 20*, 1483-1498, 1981.

Sadourny R., and K. Laval, January and July performances of the LMD-GCM, in *New Perspectives in*

Climate Modelling, ed. by A. L. Berger and C. Nicolis, pp. 173-197, Elsevier, New York, 1984.

Schery, S. D., S. Whittlestone, K. P. Hart and S. E. Hill, The flux of radon and thoron from Australian soils, *J. Geophys. Res.*, *94*, 8567-8576, 1989.

Senko, E.E., Diurnal variations in Rn exhalation and atmospheric concentrations, *I. Z. V. Atmos. and Ocean Phys.*, *4*, 533-539, 1968.

Shibata, K., and M. Chiba, A simulation of seasonal variation of the stratospheric circulation with a general circulation model, *J. Meteor. Soc. Japan*, *68*, 687-703, 1990.

Simmons, A., D. Burridge, M. Jarraud, C. Girard, and W. Wergen, The ECMWF medium-range prediction model: development of the numerical formulations and the impact of increased resolution, *Meteorol. Atmos.Phys.*, *40*, 28-60, 1988.

Spivakovsky, C.M., and Y.J. Balkanski, Tropospheric OH: constraints imposed by observations of ^{14}CO and methylchloroform, in *Report of the WMO-sponsored meeting of carbon monoxide (CO) experts*, P.C. Novelli and R.M. Rosson, eds., Global Atmospheric Watch, World Meteorological Organization, Geneva, 1994.

Spivakovsky C.M., R. Yevich, J.A. Logan, S.C. Wofsy, M.B. McElroy, and M.J. Prather, Tropospheric OH in a three dimensional chemical tracer model: an assessment based on observations of CH_3CCl_3, *J. Geophys. Res.*, *95*, 18441-18472, 1990.

Sze, N.D., M.K.W. Ko, D.K. Weisenstein, J.M. Rodriguez, R.S. Stolarski, and M.R. Schoeberl, Antarctic ozone hole: Possible implications for ozone trends in the southern hemisphere, *J. Geophys. Res.*, *94*, 11,521-11,528, 1989.

Thuburn, J., Use of a Flux-limited Scheme for Vertical Advection in a GCM, *Q. J. R. Meteorol. Soc.*, *119*, 469-487, 1993.

Tiedtke, M., A comprehensive mass flux scheme for cumulus parameterization in large-scale models, *Mon. Weath. Rev.*, *117*, 1779-1800, 1989.

Tiedtke, M., W. Heckley, and J. Slingo, Tropical forecasting at ECMWF: The influence of physical parametrization on the mean structure of forecasts and analyses, *Q. J. R. Meteorol. Soc.*, *114*, 639-664, 1988.

Tung, K.K., On the two-dimensional transport of stratospheric gases in isentropic coordinates, *J. Atmos. Sci.*, *39*, 2600-2618, 1982.

Tung, K.K., Nongeostrophic theory of zonally averaged circulation. Averaged circulation. Part I. Formulation, *J. Atmos. Sci.*, *43*, 2600-2618, 1986.

Turekian, K.K., Y. Nozaki, and L.K. Benninger, Geochemistry of atmospheric radon and radon products, *Ann. Rev. Earth Planet. Sci.*, *5*, 227-255, 1977.

Ussler, W. III, P.S. Bakwin, and C.S. Martens, Determining vertical trace gas transport within the atmospheric boundary layer using radon-222: preliminary results from a tall tower in eastern North Carolina, *EOS Supp.*, *74*, 70, 1993.

Walton, J.J., M.C. MacCracken and S.J. Ghan, A global-scale Lagrangian trace species model of transport, transformation, and removal processes, *J. Geophys. Res.*, *93*, 8339-8354, 1988.

Weisenstein, D.K., M.K.W. Ko, J.M. Rodriguez, and N.D. Sze, Impact of heterogeneous chemistry on model calculated ozone change due to high speed civil transport aircraft, *Geophys. Res. Lett.*, *18*, 1991-1994, 1991.

Weisenstein, D.K., M.K.W. Ko, and N.D. Sze, The chlorine budget of the present day atmosphere: A

modeling study, *J. Geophys. Res.*, *97*, 2547-2559, 1992.

Wilkening, M.H., Daily and annual courses of natural atmospheric radioactivity, *J. Geophys. Res.*, *64*, 521-526, 1959.

Wilkening, M.H., W.E. Clements and D. Stanley, Radon 222 flux measurements in widely separated regions, in *The Natural Radiation Environment II*, U.S. Energy and Research Development Administration, Oak Ridge, Tenn., 717-730. 1975.

Wilkening, M.H., and W.E. Clements, Radon 222 from the ocean surface, *J. Geophys. Res.*, *80*, 3828-3830, 1975.

Williamson, D.L., J.T. Kiehl, V. Ramanathan, R.E. Dickinson, and J.J. Hack, Description of NCAR Community Climate Model (CCM1), NCAR Tech. Note NCAR/TN-285+STR, Natl. Cent. for Atmos. Res., Boulder, Colo., 1987. (Available as NTIS PB87-203782, 112 pp., from Natl. Tech. Inf. Serv., Springfield Va.)

Yang, H., K.K. Tung, and E. Olaguer, Nongeostrophic theory of zonally averaged circulation. Part II. Eliassen-Palm flux divergence and isentropic mixing coefficient, *J. Atmos. Sci.*, *47*, 215-241, 1990.

Yang, H., E., Olaguer, and K.K. Tung, Simulation of the present-day atmospheric ozone, odd nitrogen, chlorine and other species using a coupled 2-D model in isentropic coordinates, *J. Atmos. Sci.*, *48*, 442-471, 1991.

Zimmermann, P.H., MOGUNTIA: A handy global tracer model, in *Air Pollution Modeling and its Applications VI*, ed. by H. van Dop, pp.593-608, NATO/CCMS, Plenum, New York, 1988.

Zimmermann, P.H., H. Feichter, H.K. Rath, P.J. Crutzen, and W. Weiss, A global three-dimensional source-receptor model investigating ^{85}Kr, *Atmos. Environ.*, *23*, 25-35, 1989.

Table 1. Participating models

	Simulations	Correspondent
established 3-D synoptic models		
A. CCM2	A,B,C	Rasch
B. ECHAM3	A,B,C	Feichter, Köhler
C. GFDL/ZODIAC	A,B,C	Kasibhatla
D. GISS/H/I	A,B,C, ^{210}Pb	Jacob
E. KNMI/TM2	A,B,C	Verver, Van Velthoven
F. LLNL/GRANTOUR	A,B,C, ^{210}Pb	Dignon, Penner
G. LLNL/E	A,B,C	Bergmann
H. LMD	A	Genthon
I. TM2Z	A,B,C	Balkanski, Ramonet
established 3-D model *with monthly mean winds*		
J. MOGUNTIA	A,B,C	Zimmermann
3-D synoptic models under development		
k. CCCA-GCM	A	Beagley, de Grandpré
m. LaRC	A	Grose, Blackshear
n. LLNL/IMPACT	A,B,C	Rotman
o. MRI	A,B,C	Chiba
p. TOMCAT	A,B,C	Chipperfield
q. UGAMP	A,B,C	Stockwell
2-D models		
R. AER	A,B,C	Shia
S. UCAMB	A,B,C, ^{210}Pb	Law, Wild
T. HARWELL	A,B,C, ^{210}Pb	Reeves
U. UW	A,B,C	Brown, Yang

A description of each model is given in the Appendix. "Synoptic" models use meteorological fields with resolution finer than one day.

Table 2. Simulations

Case A: ^{222}Rn

Source: 72 moles yr^{-1} distributed as follows:
    70-90°S and 70-90°N: no emission
    60-70°S and 60-70°N: 0.005 atoms cm^{-2} s^{-1}
    60°S-60°N, oceans: 0.005 atoms cm^{-2} s^{-1}
    60°S-60°N, land: 1.0 atoms cm^{-2} s^{-1} (adjusted as necessary
        to yield a global source of 72 moles yr^{-1})

Sink: radioactive decay ($k = 2.1 \times 10^{-6}$ s^{-1})

Case B: aircraft tracer

Source: 72 moles yr^{-1} distributed uniformly in the 400-200 mb column over four line segments (18 moles yr^{-1} for each segment): Japan-California (34°N, 120°E-120°W) California-New York (40°N, 120-75°W) Boston-Rome (42°N, 75°W-10°E), and Rome-Oslo (42-60°N, 10°E).

Sink: same as in case A

Case C: tropical lightning tracer

Source: 72 moles yr^{-1} distributed uniformly in the 400-200 mb column at 10°S-10°N over three longitudinal belts: 75-45°W, 10-40°E, and 100-130°E.

Sink: same as in case A

^{210}Pb *aerosol*

Source: radioactive decay of ^{222}Rn from case A

Sink: wet and dry deposition (see text).

Table 3a. Model output diagnostics

Cases A, B, C, Jun-Aug and Dec-Feb

1. Three-month average contour plots of concentrations as a function of latitude and pressure: zonal mean, dateline (180°), and Greenwich meridian (0°).

2. Three-month average contour plots of concentrations as a function of latitude and longitude: 300 m above local surface, 600 mb, and 300 mb.

3. Plots and seasonal statistics of 3-month time series of concentrations at 7 sites (Table 3b) and 3 altitudes per site: 300 m above local surface, 600 mb, and 300 mb. The time series at 300-m altitude are sampled once a day at 1400h local time. The time series at 600 mb and 300 mb are sampled at all times of day. Seasonal statistics include means, variances, medians, quartiles, and extremes.

^{210}*Pb aerosol*

1. Global atmospheric inventory at the end of the 4-month simulation (February 28 and August 31) partitioned into three altitude bands: below 600 mb, 600-300 mb, and above 300 mb.

2. Three-month average (Jun-Aug and Dec-Feb) contour plots of concentrations as a function of latitude and pressure: zonal mean, dateline, and Greenwich meridian.

Units: All output reported in units of moles and molar mixing ratios (mol/mol). Conversion factors to common radioactivity units for ^{222}Rn are 1 mole = 3.4×10^7 Curies (Ci) = 1.25×10^6 Becquerels (Bq); and 1×10^{-21} mol/mol = 1.52 pCi/SCM = 5.6×10^{-2} Bq/SCM (where SCM is a standard cubic meter of air at 273.15 K and 1 atm). Conversion factors for ^{210}Pb are 1 mole = 1.6×10^4 Ci = 5.9×10^{14} Bq; and 1×10^{-21} mol/mol = 0.71 fCi/SCM = 2.6×10^{-5} Bq/SCM.

Table 3b. Sites for time series

Site	Available observations
Kirov, Russia (58°N, 49°E)	Senko [1968]
Cincinnati (40°N, 84°W)	Gold et al. [1964]
Socorro, New Mexico (34°N, 107°W)	Wilkening [1959]
Hawaii (20°N, 155°W)	Kritz et al. [1990]
Samoa (14°S, 171°W)	none
Crozet Island (46°S, 51°E)	Polian et al. [1986]
Ferraz, Antarctica (62°S, 58°W)	Pereira [1990]

Observations are for surface air except at Hawaii (200 mb).

FIGURE CAPTIONS.

Figure 1. Seasonal frequency distributions of simulated ^{222}Rn concentrations at Cincinnati (mixed layer, 1400h local time), Crozet Island (ibid.), and Hawaii (300 mb, all times of day) in June-August. See Table 3a for conversion of mol/mol to common radioactivity units. Models are identified by letter code (see Table 1). Values for the 2-D models (R-U) are zonal mean concentrations. Boxplots for each model show seasonal extrema (whiskers) and quartiles (shaded box); the white band indicates the mean concentration (Cincinnati) or the median (Crozet, Hawaii). The concentrations at Cincinnati and Crozet were sampled at 1400h local time except in ECHAM3 where they were sampled as 12-hour averages. Dashed lines in the Cincinnati panel show the interannual range of observed mean afternoon concentrations in June-August reported by Gold et al. [1964]. Dotted lines in the Crozet panel show the range of maximum concentrations observed during high-^{222}Rn episodes recurring·about once a month [Polian et al., 1986]. Dashed and dotted lines in the Hawaii panel show respectively the median and the extrema of 17 aircraft measurements at 200 mb over Hawaii in July-August [Kritz et al., 1990]; the minimum indicated by the dotted line (0.7×10^{-21} mol/mol) is the detection limit of the instrument.

Figure 2. Mean vertical profiles of ^{222}Rn concentrations over northern mid-latitude continents in (a) June-August and (b) December-February. The solid lines are the mean profiles obtained by Liu et al. [1984] by averaging aircraft observations from various locations in North America and Europe; the horizontal bars are the associated standard errors (standard deviations on the means). Model results (symbols) are seasonal means at 300-m above ground, 600 mb (shown as 4.2-km), and 300 mb (shown as 9.2-km) averaged for Kirov, Cincinnati, and Socorro. Some symbols have been moved up or down from the actual sampling altitude to improve legibility. The models are identified by the letter code of Table 1. See Table 3a for unit conversion factors.

Figure 3. Frequency distribution of ^{222}Rn concentrations simulated by the established 3-D models at 300 mb over Kirov in June-August. Models are identified by letter code (Table 1). Boxplots show seasonal extrema (whiskers), quartiles (shaded box), and medians (white band). Dashed lines indicate the observed range of concentrations at 300 mb from four measurements over eastern Ukraine in July [Nazarov et al., 1970].

Figure 4. Mean ^{222}Rn concentrations simulated by the established 3-D models and CCCA-GCM at 300 mb in June-August. Units are 1×10^{-21} mol/mol; see Table 3a for conversion factors.

Figure 5. Zonal mean ^{222}Rn concentrations (units of 1×10^{-21} mol/mol) simulated by the established models and CCCA-GCM in June-August. Data for LMD are missing.

Figure 6. Mean concentrations at 300 mb in June August for the tracer released in the upper troposphere at northern mid-latitudes (case B). Units are 1×10^{-21} mol/mol. Data for MOGUNTIA are missing.

Figure 7. Zonal mean concentrations in June-August for the aircraft tracer released in the upper troposphere at northern mid-latitudes (case B). Units are 1×10^{-21} mol/mol.

Figure 8. Zonal mean concentrations in December-February for the tropical lightning tracer released in the upper troposphere (case C). Units are 1×10^{-21} mol/mol.

Figure 9. Global atmospheric inventory of ^{210}Pb partitioned by altitude bands.

^{222}Rn, 10^{-21} mol/mol

RADON STATISTICS FOR JUN-AUG

Cincinnati

1063

Crozet

396

Hawaii (300 mb)

MODEL

Figure 1

ALTITUDE ABOVE GROUND, km

^{222}Rn, 10^{-21} mol/mol

JJA

Figure 2a

ALTITUDE ABOVE GROUND, km
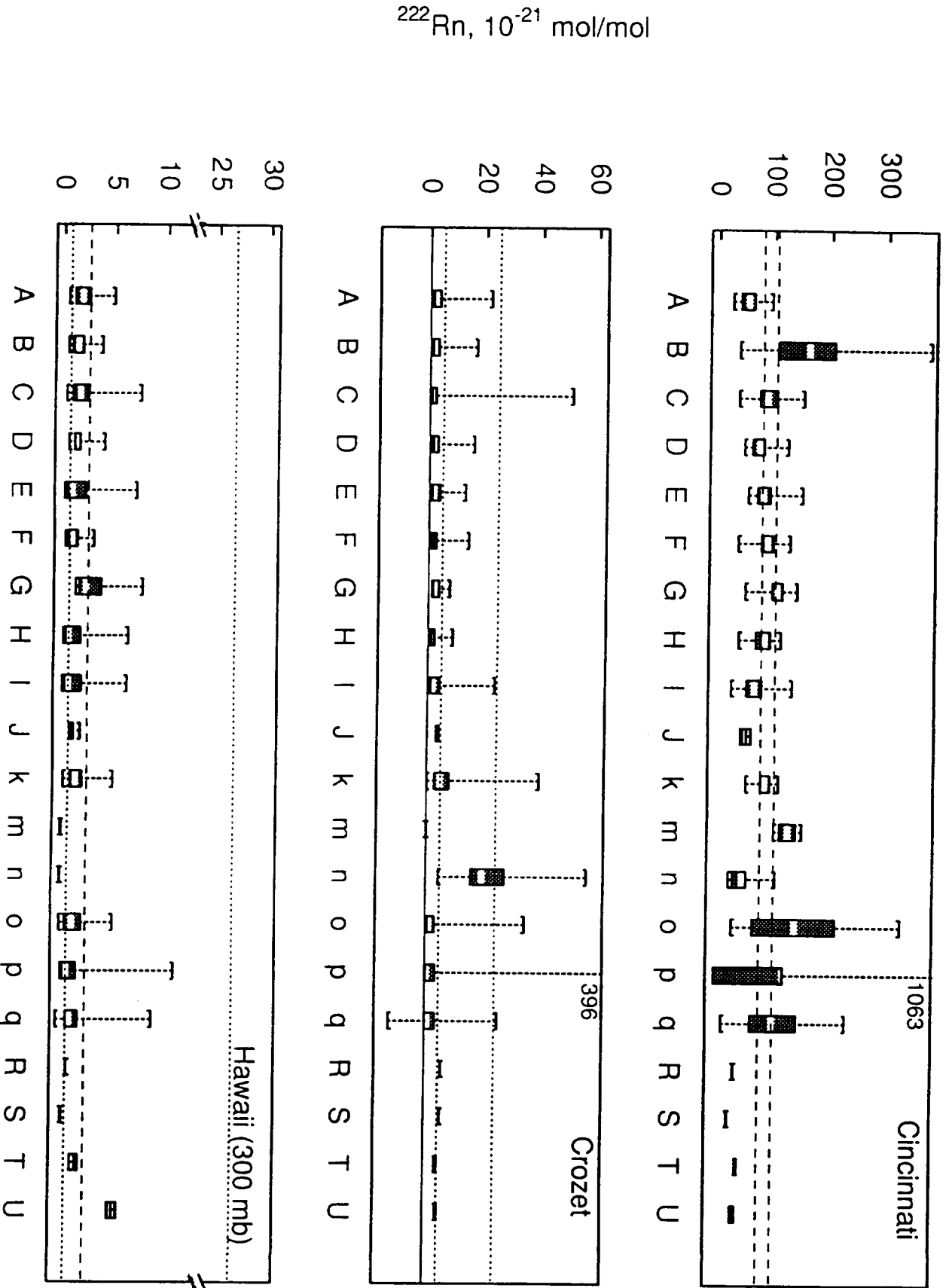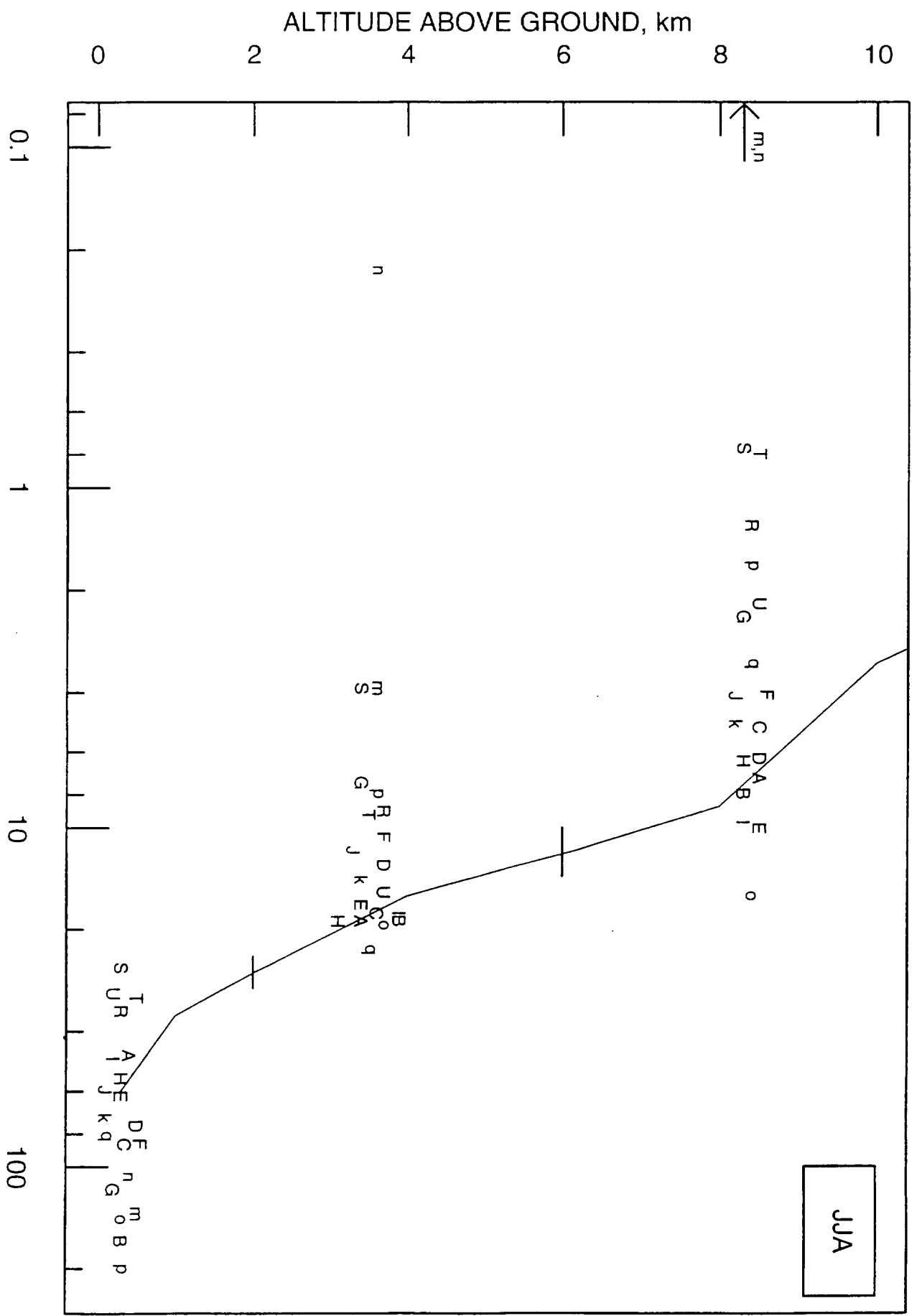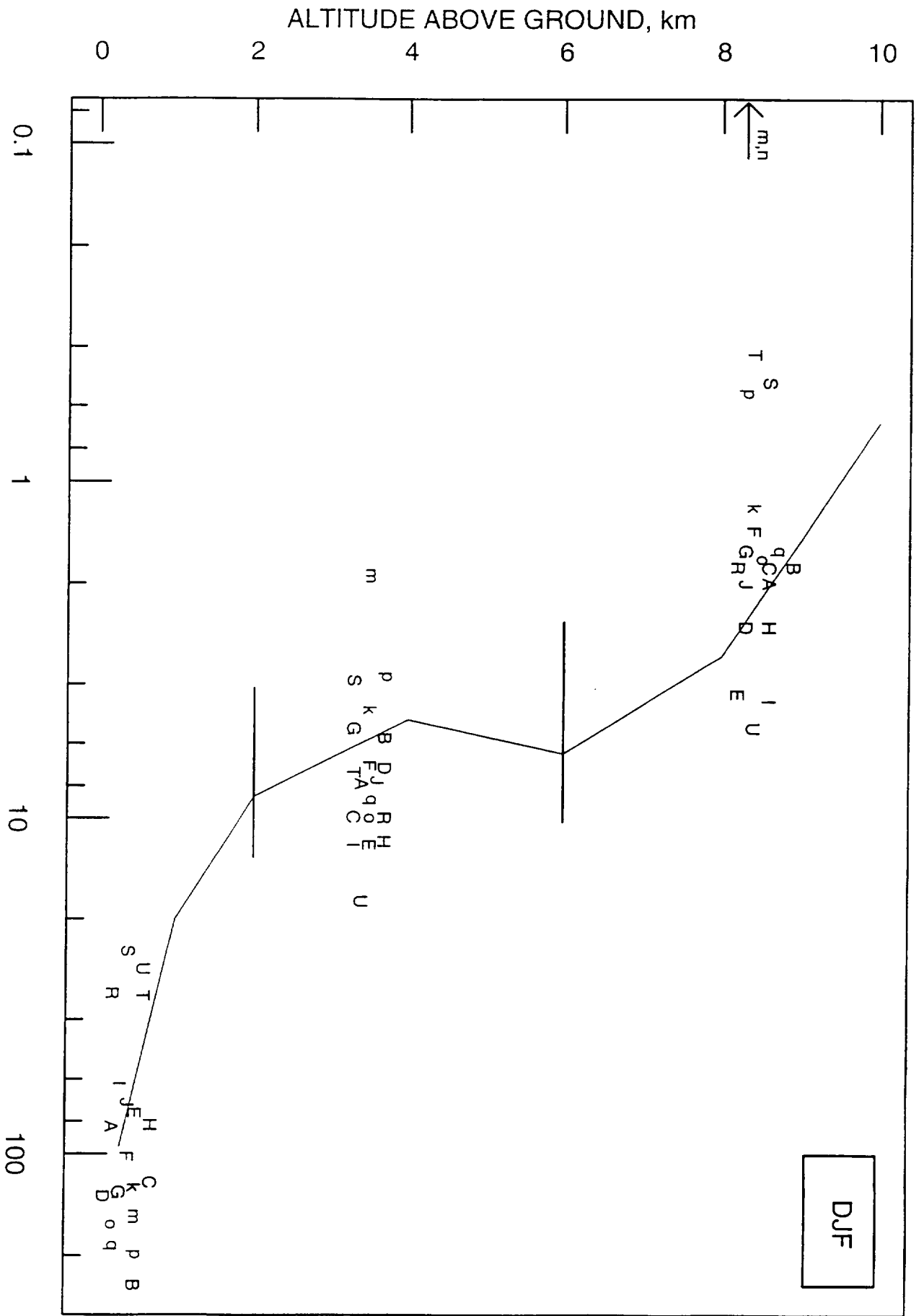
^{222}Rn, 10^{-21} mol/mol

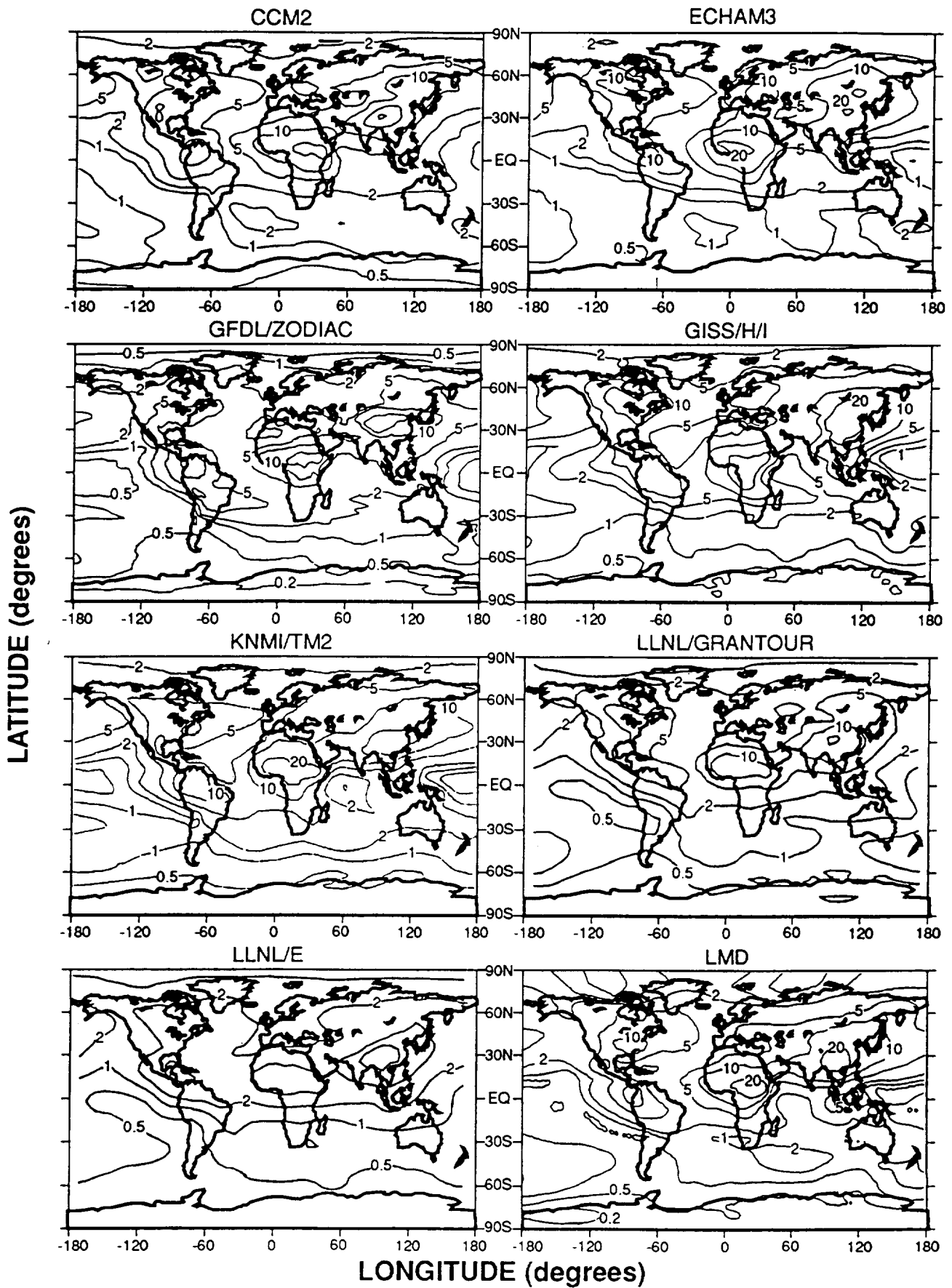Figure 2 b

Figure 3

Figure 4

TM2Z

MOGUNTIA
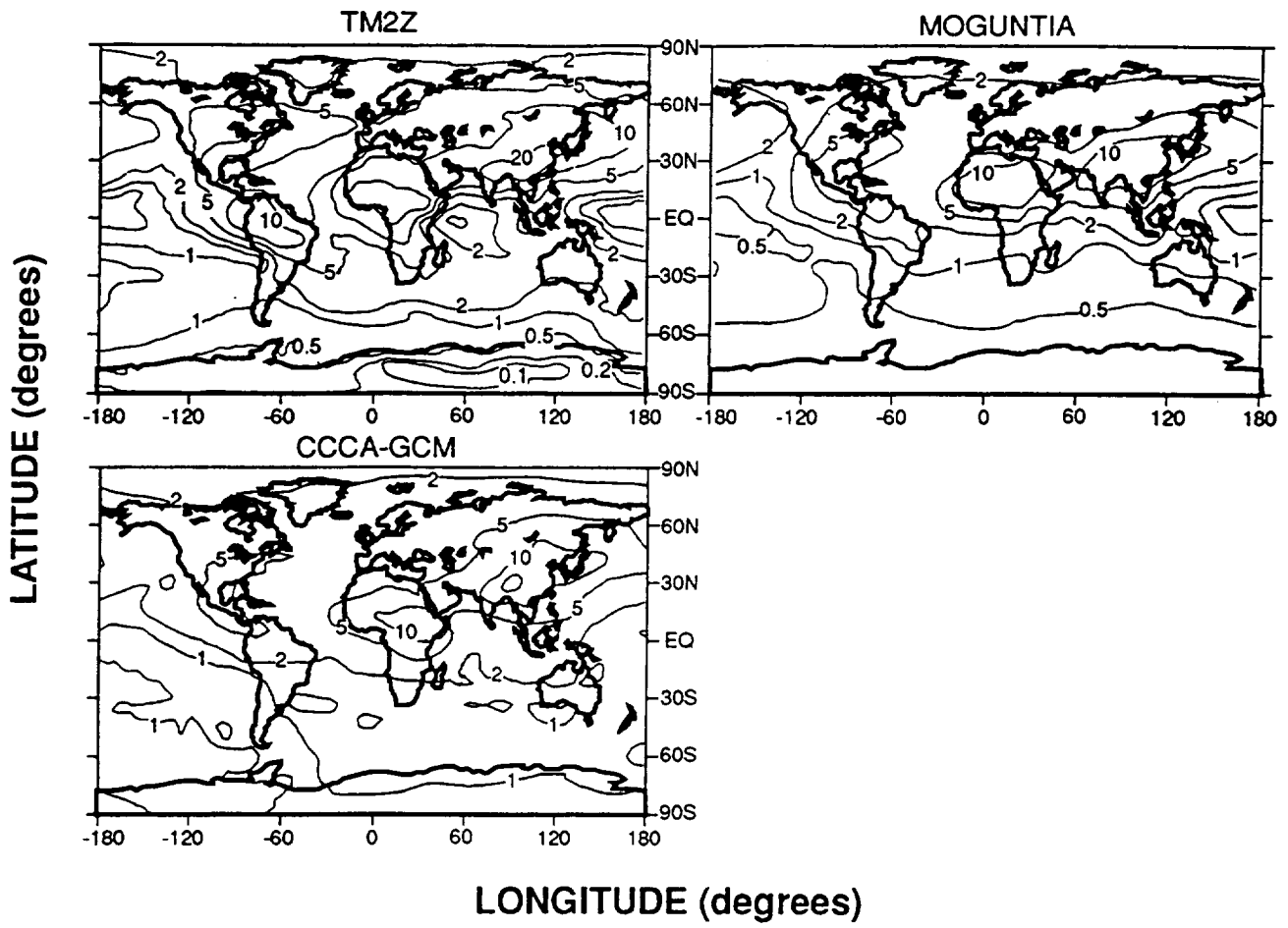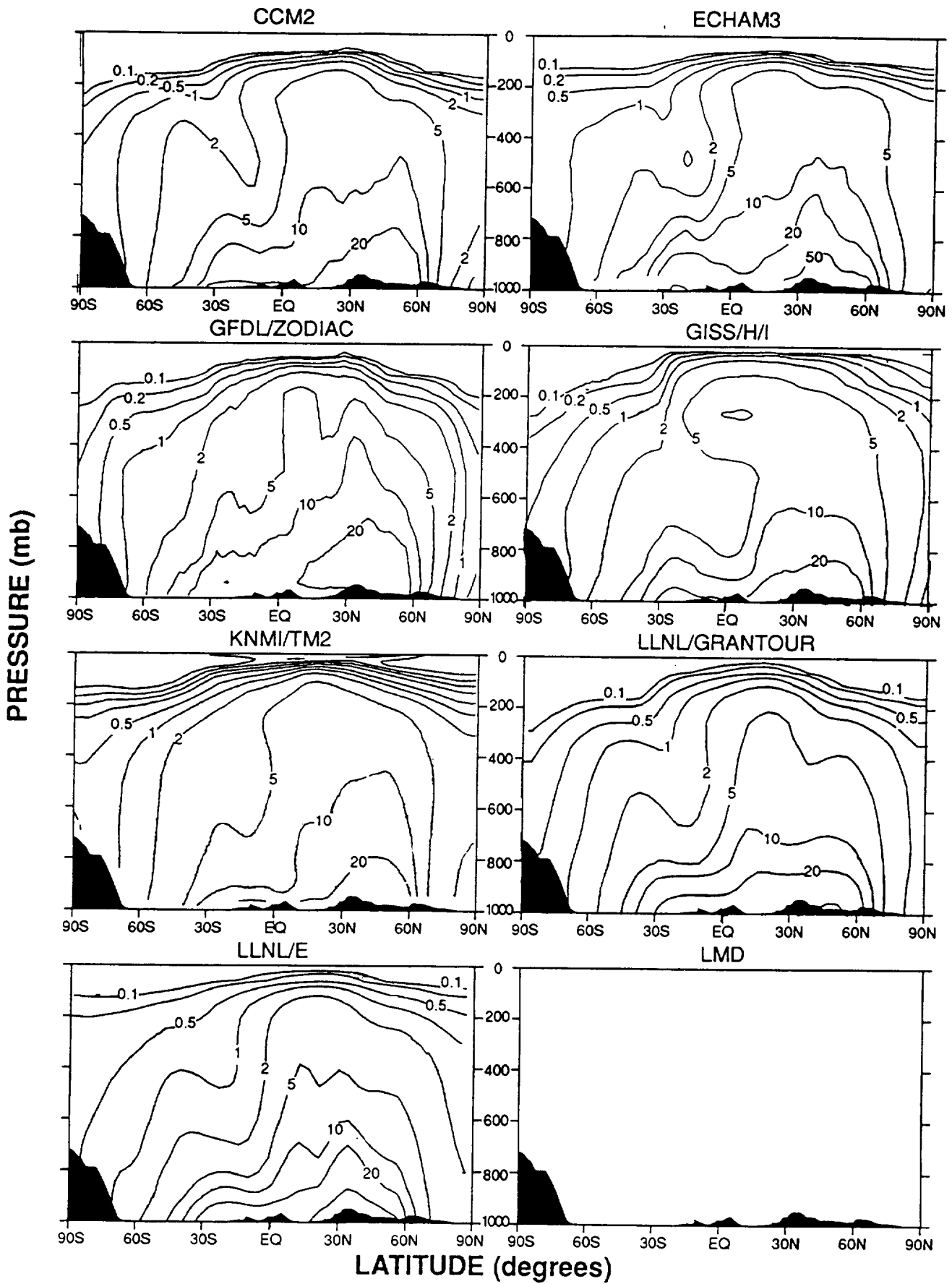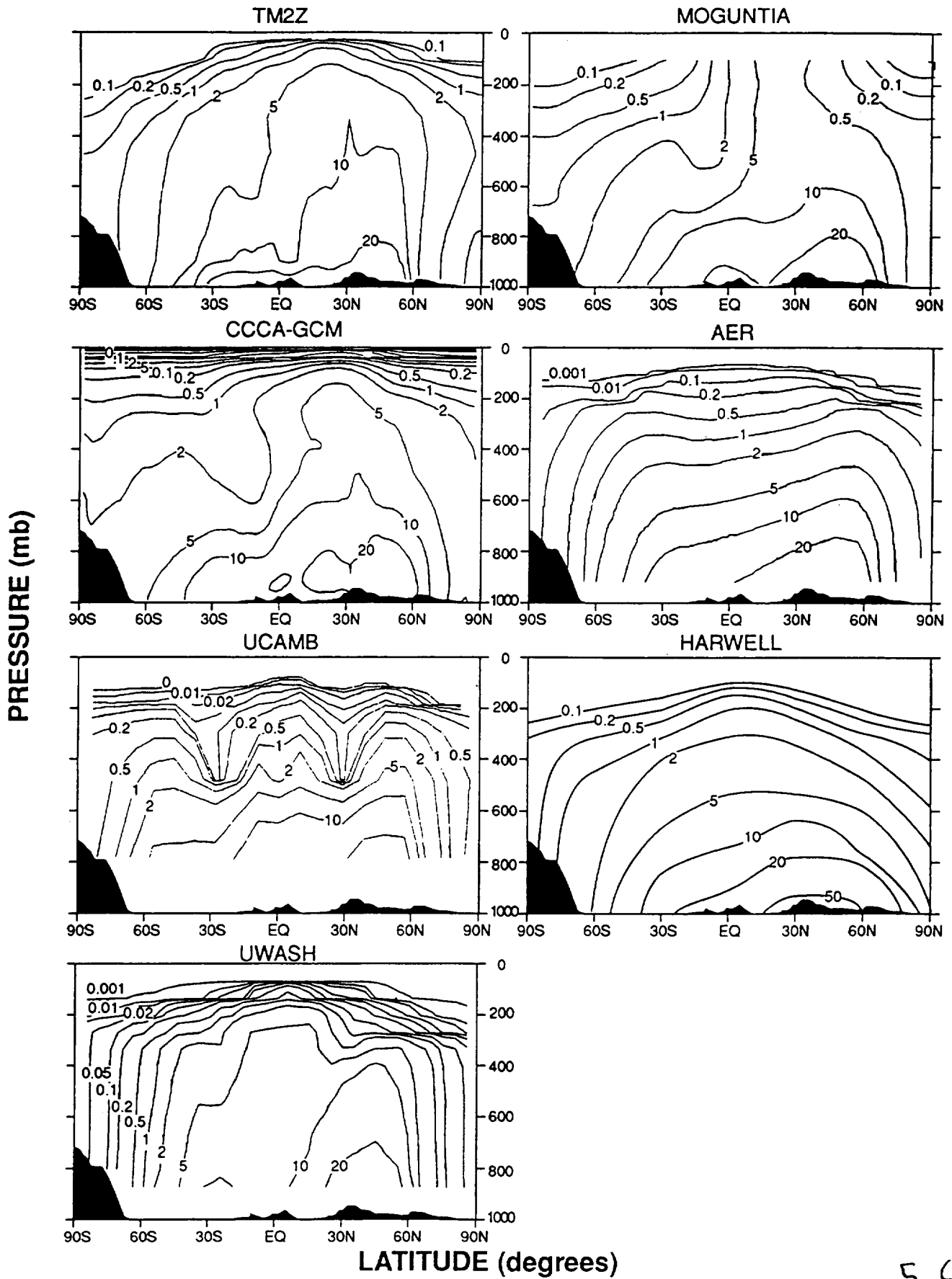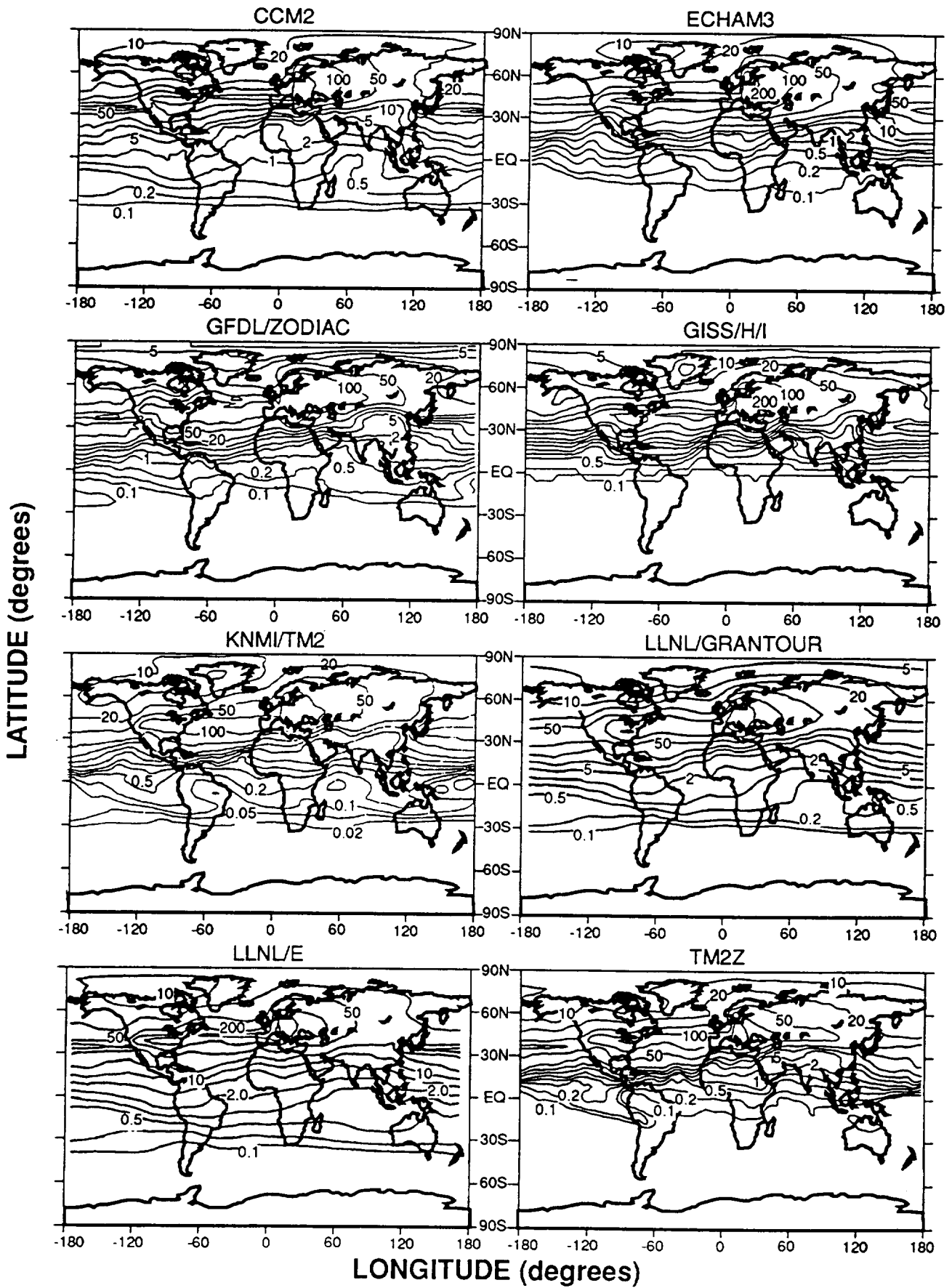
CCCA-GCM

LATITUDE (degrees)

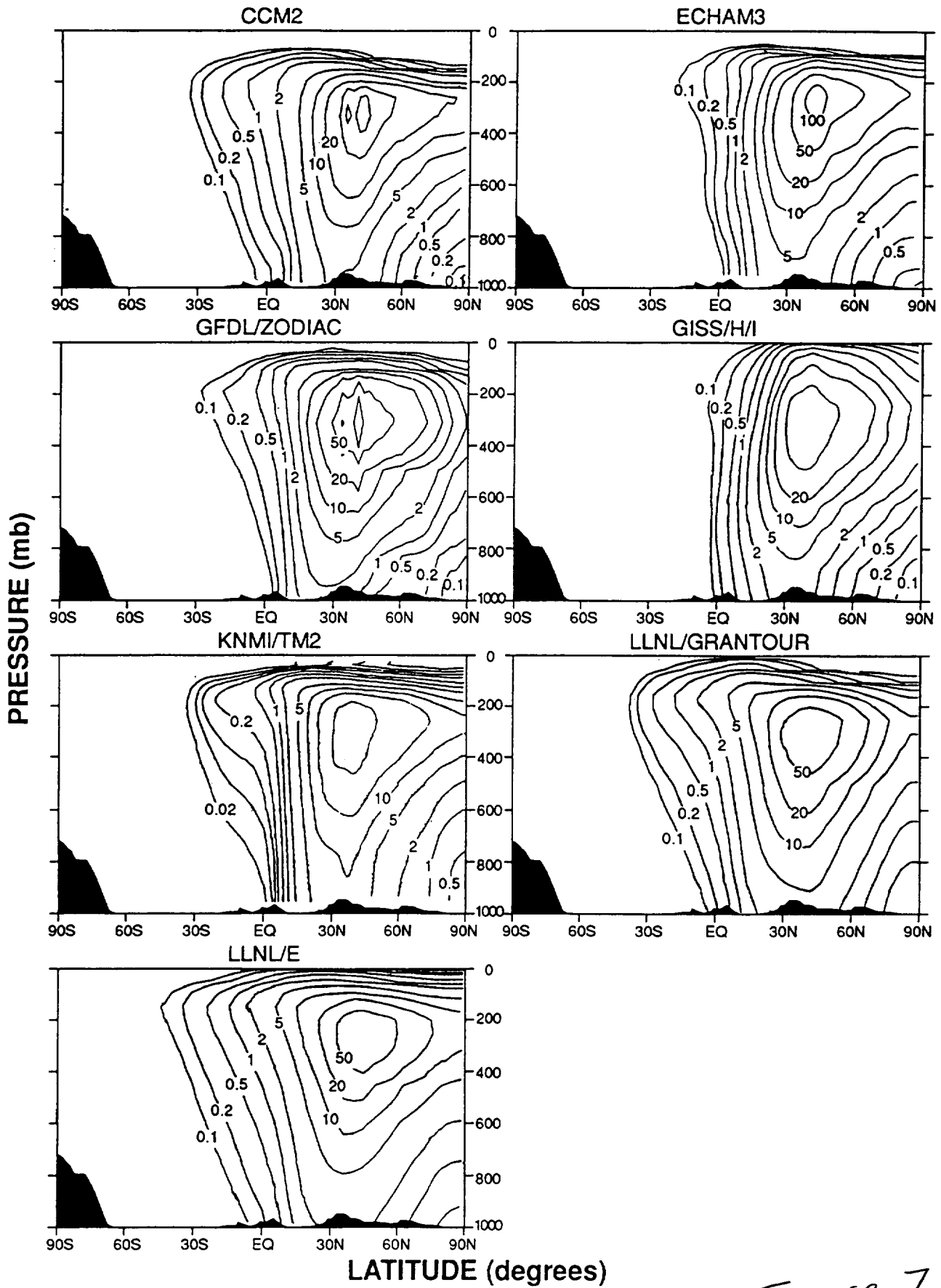LONGITUDE (degrees)
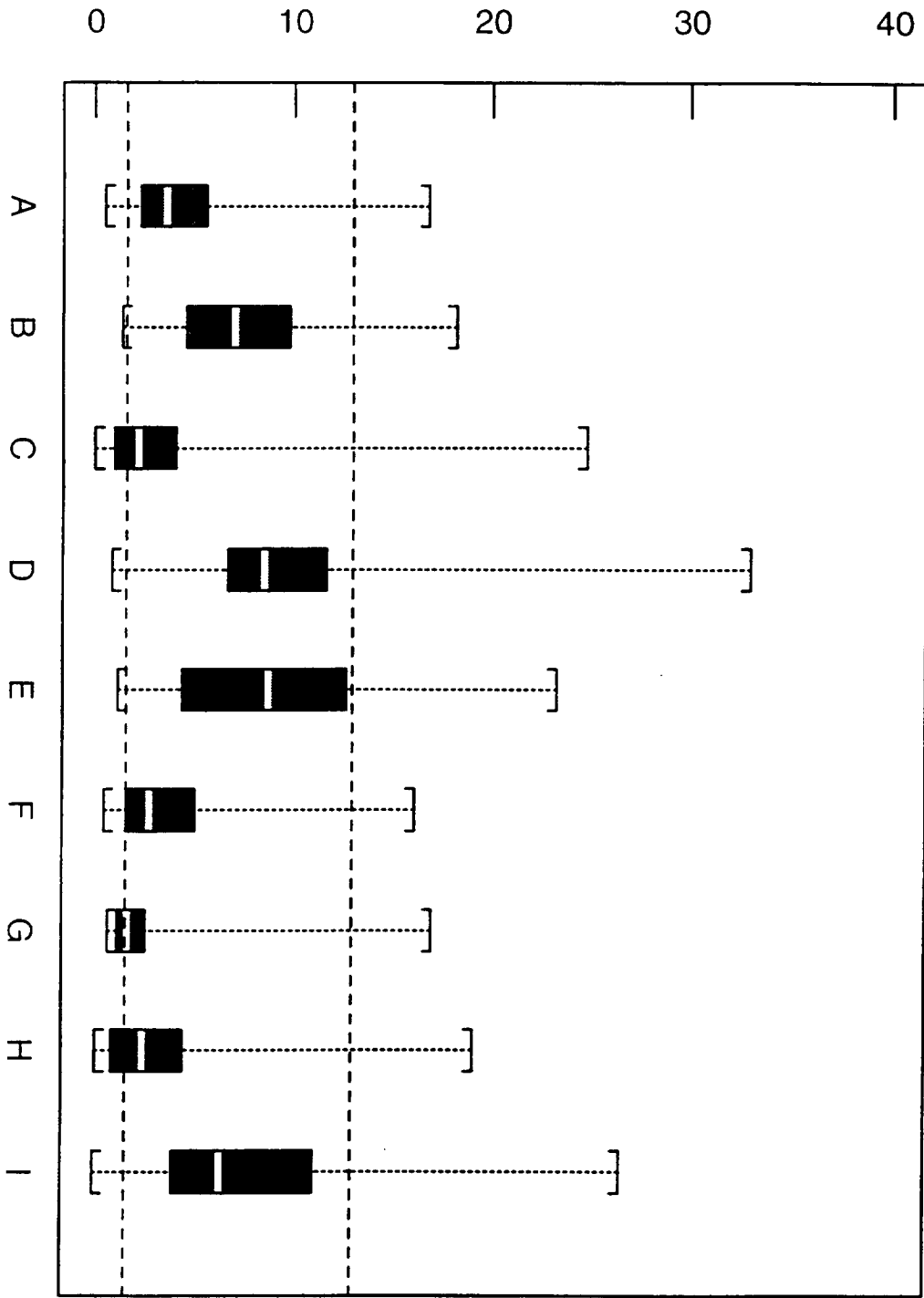
Figure 4 (cont.)

Figure 5

Figure 5 (cont.)

Figure 6

Figure 7

Figure 7 (cont.)

CCM2

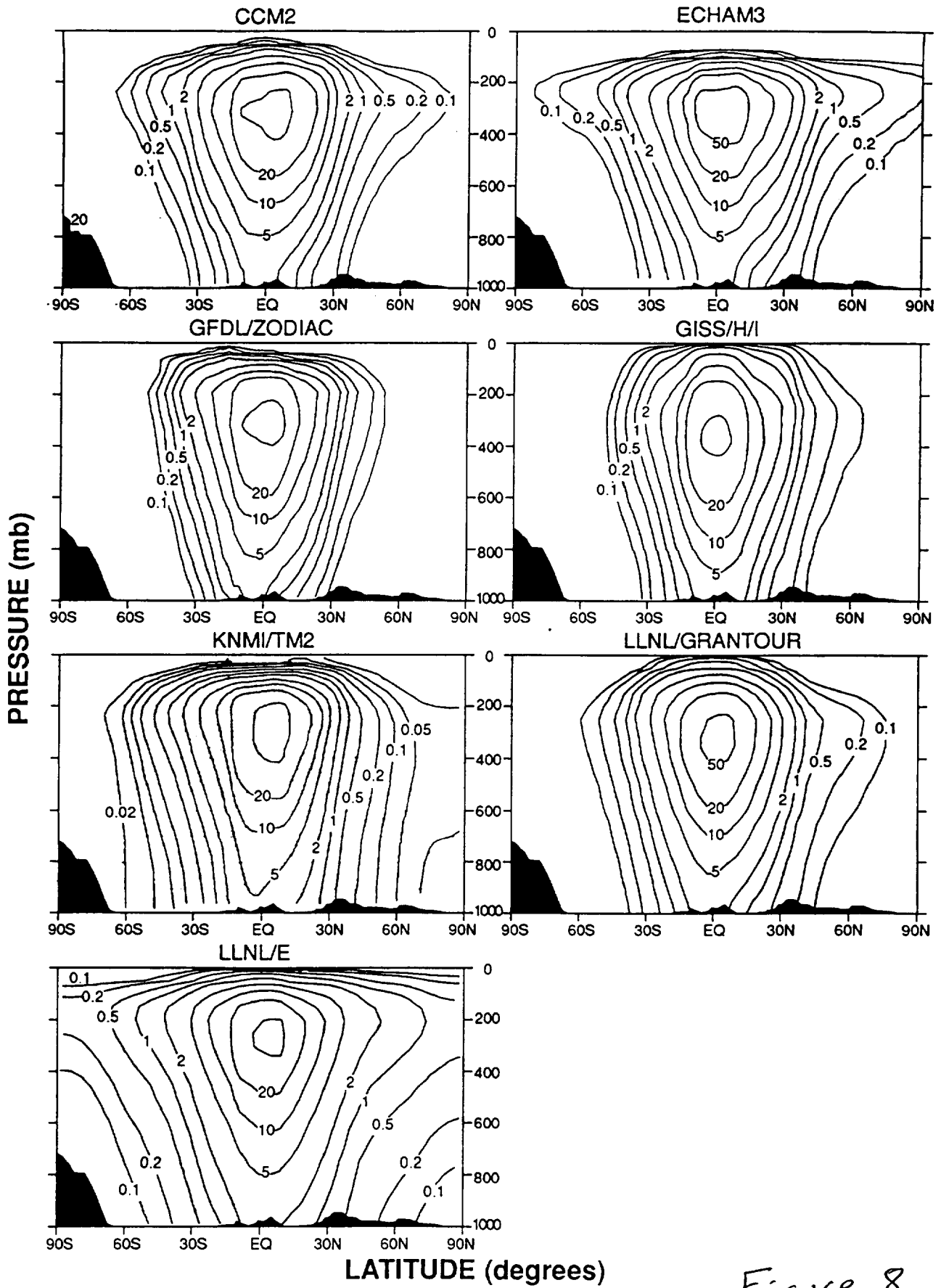ECHAM3

GFDL/ZODIAC

GISS/H/I

KNMI/TM2

LLNL/GRANTOUR

LLNL/E

PRESSURE (mb)

LATITUDE (degrees)
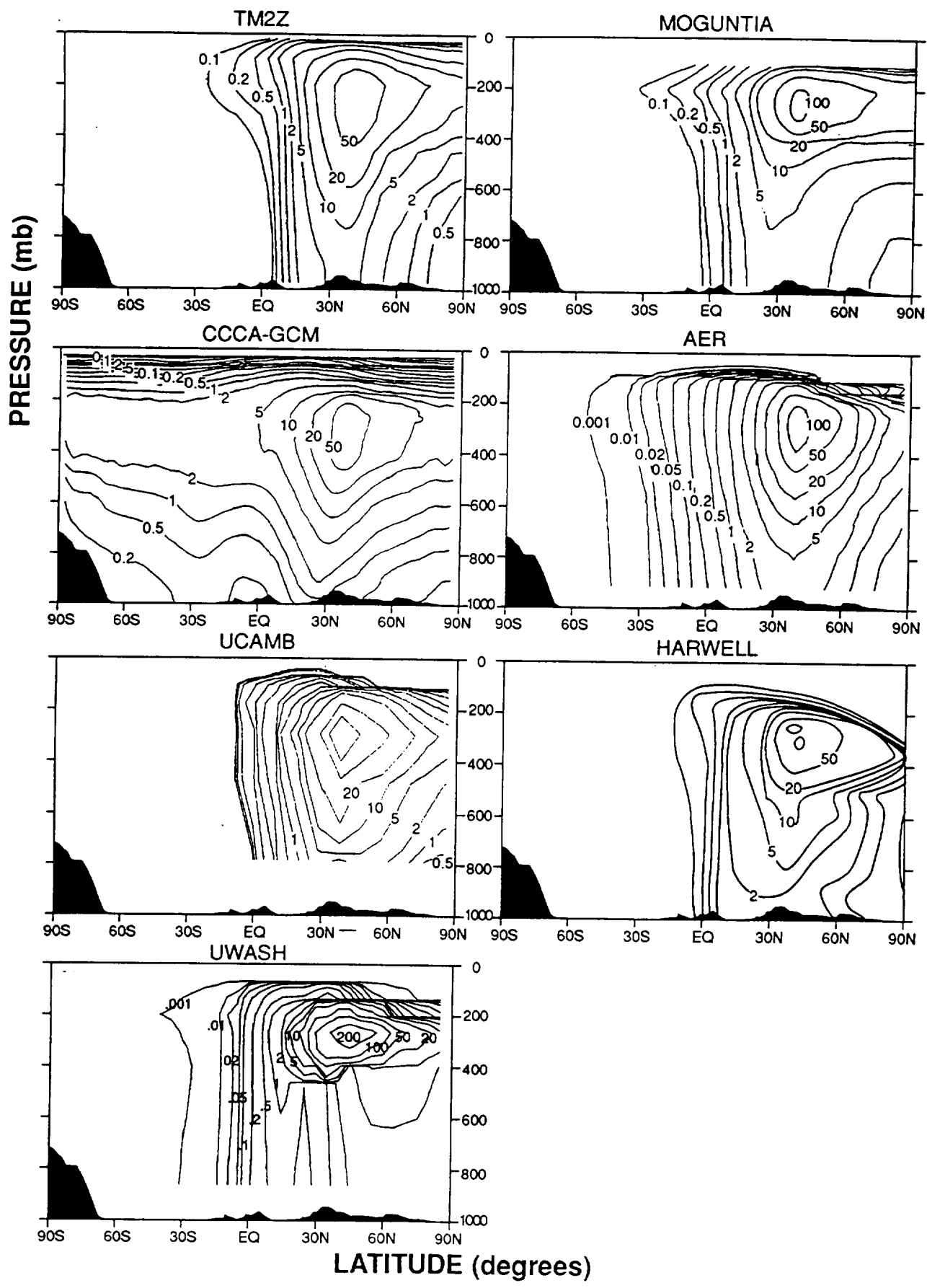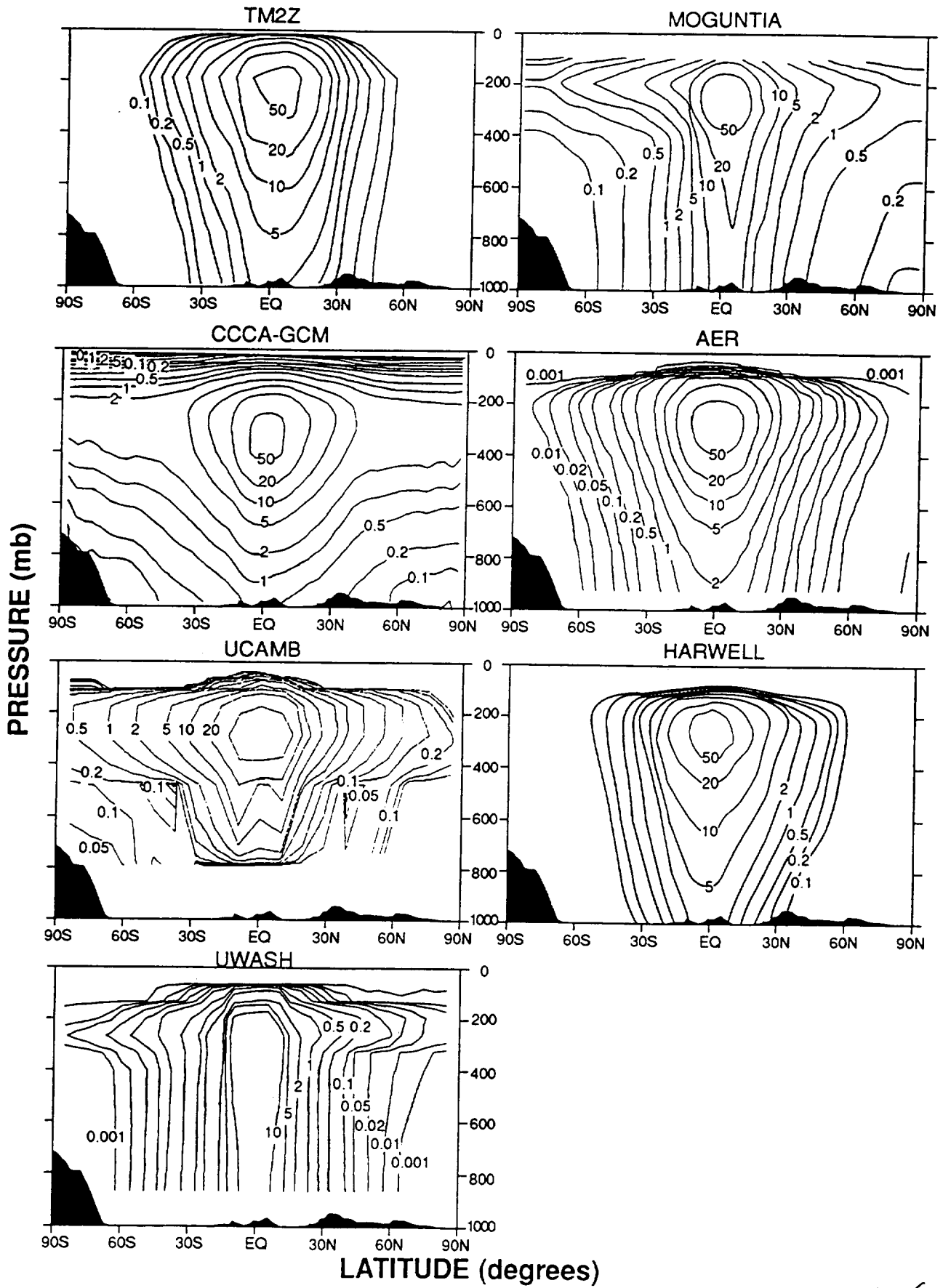
Figure 8

Figure 8 (cont.)

Figure 9

GLOBAL 210Pb INVENTORIES
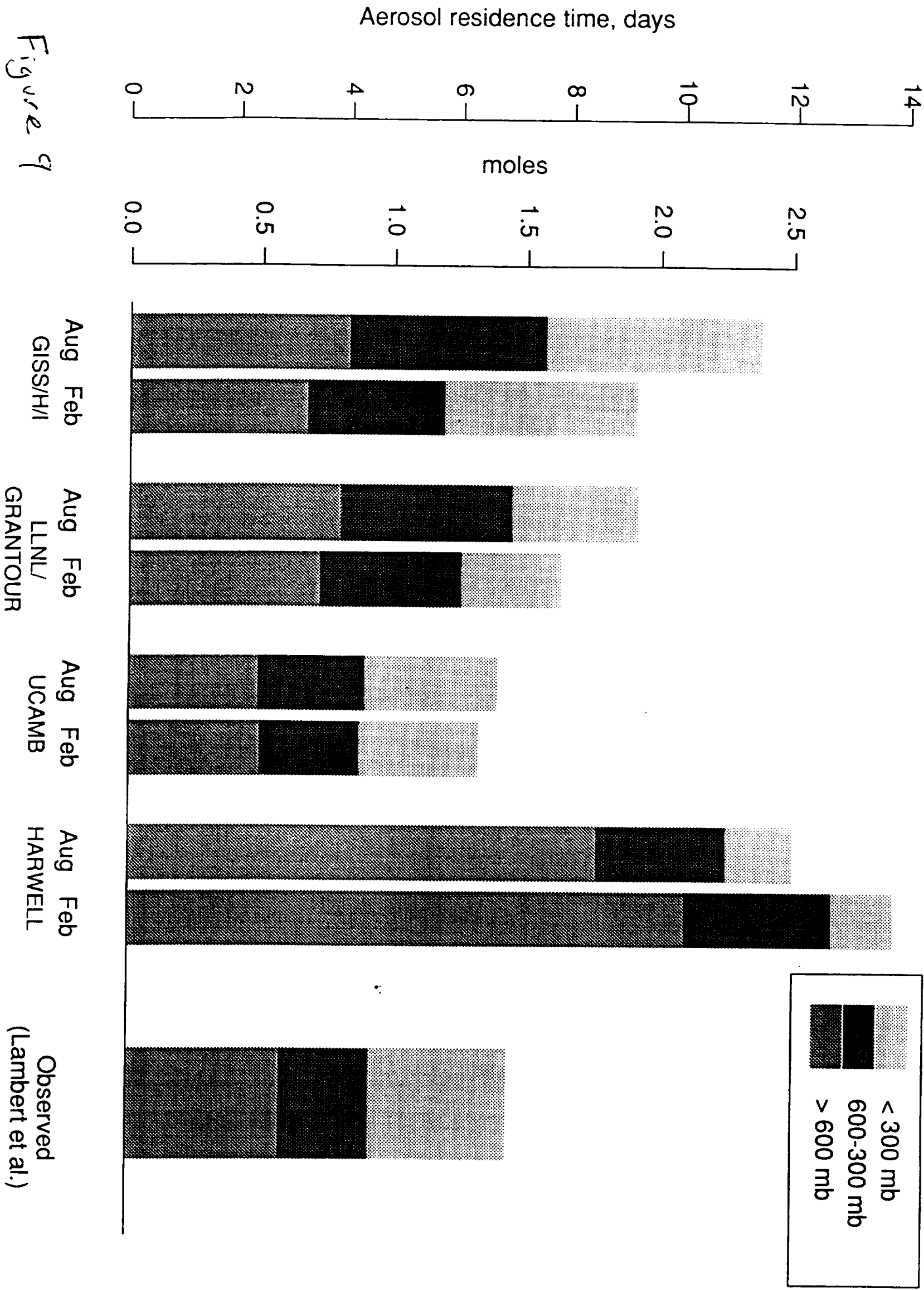
Proposed Budget
(7/1/96 -12/31/96)

Direct Labor (ITD) P Kasibhatla 83% FTE	25,898
Benefits	10,660
Total Direct Labor	36,558
Direct Labor Overhead (ITD)	15,164

Expenses:

Travel	2,000
Materials and Supplies	5,074
Equipment	0
Lease	1,244
Subtotal Expenses	8,318
Total MCNC Incurred	60,040

Subcontract Expense:

Georgia Tech	10,010
Total Subcontracts	10,010
Subtotal Contract Costs	70,050
General and Administration	6,634
TOTAL FUNDING REQUEST	76,684

Provisional Rates	
Benefits	41.16%
Tech Ovhd	41.48%
G & A	9.47%

6/17/96

Drug-Free Workplace Certification

I. MCNC certifies that it will provide a drug-free workplace by:

   A. Publishing a statement notifying employees that the unlawful manufacture, distribution, dispensing, possession or use of a controlled substance in the grantee's workplace and specifying the actions that will be taken against employees for violation of such prohibition;

   B. Establishing a drug-free awareness program to inform employees about--

      1. The dangers of drug abuse in the workplace;

      2. The grantee's policy of maintaining a drug-free workplace;

      3. Any available drug counseling, rehabilitation, and employee assistance programs: and

      4. The penalties that may be imposed upon employees for drug abuse violations occurring in the workplace;

   C. Making it a requirement that each employee to be engaged in the performance of the grant/contract be given a copy of the statement required by paragraph (A);

   D. Notifying the employee in the statement required by paragraph (A) that, as a condition of employment under the grant, the employee will--

      1. Abide by the terms of the statement; and

      2. Notify the employer of any criminal drug statute conviction for a violation occurring in the workplace no later than five days after such conviction;

   E. Notifying the agency within ten days after receiving notice under subparagraph (D)(2) from an employee or otherwise receiving actual notice of such conviction;

   F. Taking one of the following actions, within 30 days of receiving notice under subparagraph (D)(2). with respect to any employee who is so convicted--

      1. Taking appropriate personnel action against such an employee, up to and including termination: or

      2. Requiring such employee to participate satisfactorily in a drug abuse assistance or rehabilitation program approved for such purposes by a Federal, State, or local health, law enforcement, or other appropriate agency;

   G. Making a good faith effort to continue to maintain a drug-free workplace through implementation of paragraphs (A), (B), (C), (D), (E) and (F).

II. MCNC shall insert in the space provided below the site(s) for the performance of work done in connection with the specific grant/contract:

Place of Performance (Street address, city, county, state, zip code)

Highway 54, 200 Park, Suite 112

Research Traingle Park, NC 27709

Durham County

CERTIFICATION REGARDING DEBARMENT, SUSPENSION, PROPOSED DEBARMENT, AND OTHER RESPONSIBILITY MATTERS-PRIMARY COVERED TRANSACTIONS

(1)   The prospective primary participant certifies, to the best of its knowledge and belief, that it and its principals:

        (a)   Are not presently debarred, suspended, proposed for debarment, declared ineligible, or voluntarily excluded from covered transactions by any Federal department or agency;

        (b)   Have not within a three-year period preceding this proposal been convicted of or had a civil judgment rendered against them for commission of fraud or a criminal offense in connection with obtaining, attempting to obtain, or performing a public (Federal, State or local) transaction or contract under a public transaction; violation or Federal or State antitrust statutes or commission of embezzlement, theft, forgery, bribery, falsification or destruction of record, making false statements, or receiving stolen property;
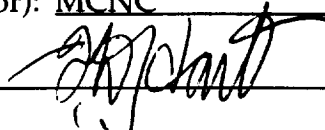
        (c)   Are not presently indicted for or otherwise criminally or civilly charged by a government entity (Federal, State or local) with commission of any of the offenses enumerated in paragraph (1) (b) of this certification; and

        (d)   Have not within a three-year period preceding this application/proposal had one or more public transactions (Federal, State or local) terminated for cause or default.

(2)   Where the prospective primary participant is unable to certify to any of the statements in this certification, such prospective participant shall attach an explanation to this proposal.

Organization (Offeror): MCNC

Signature: _____

Typed Name: Franklin D. Hart

Title: President   Date: 06/18/96

DISCLOSURE OF LOBBYING ACTIVITIES

Complete this form to disclose lobbying activities to 31 U.S.C. 1352

1. Type of Federal Action: N/A	2. Status of Federal Action: N/A	3. Report Type:
☐ a. contract b. grant c. cooperative agreement d. loan e. loan guarantee f. loan insurance	☐ a. bid/offer/application b. initial award c. post-award	[a] a. initial filing b. material change **For Material Change Only:** year _____ quarter _____ date of last report _____

4. Name and Address of Reporting Entity:	5. If Reporting Entity in No. 4 is Subawardee, Enter Name and Address of Prime:
☐ Prime ☐ Subawardee Tier _____ , *if known:* MCNC 3021 Cornwallis Road Research Triangle Park, NC 27709 Congressional District, *if known:* 4th	 Congressional District, *if known:*

6. Federal Department/Agency: N/A	7. Federal Program Name/Description: N/A CFDA Number, *if applicable:* _____

8. Federal Action Number, *if known:* N/A	9. Award Amount, *if known:* N/A $

10. a. Name and Address of Lobbying Entity *(if individual, last name, first name, MI):* Barfield, Vic Barfield and Wilson 888 16th Street, NW, Suite 714 Washington, DC 20006	b. Individuals Performing Services *(including address if different from No. 10a)* (last name, first name, MI): Barfield, Vic

<center>(attach Continuation Sheet(s) SF-LLL-A, if necessary)</center>

11. Amount of Payment (check all that apply): $ 13,000/mo [x] actual [x] planned	13. Type of Payment (Check all that apply): [x] a. retainer ☐ b. one-time fee ☐ c. commission ☐ d. contingent fee ☐ e. deferred [x] f. other; specify: monthly payments of $13,000
12. Form of Payment (check all that apply): [x] a. cash ☐ b. in-kind; specify: nature _____ value _____	

14. Brief Description of Services Performed or to be Performed and Date(s) of Service, including officer(s), employee(s), or Member(s) contacted, for Payment Indicated in Item 11:

Serve as consultant to MCNC sith responsibility for strategic, analysis and budgetary matters before the U.S. Congress and assist MCNC with other federal and private funding opportunities.

<center>(attach Continuation Sheet(s) SF-LLL-A, if necessary)</center>

15. Continuation Sheet(s) SF-LLL-A attached:	[x] YES ☐ NO

16. Information requested through this form is authorized by title 31 U.S.C. section 1352. This disclosure of lobbying activities is a material representation of fact upon which reliance was placed by the tier above when this transaction was made or entered into. this disclosure is required pursuant to 31 U.S.C. 1352. This information will be reported to the Congress semi-annually and will be available for public inspection. Any person who fails to file the required disclosure shall be subject to a civil penalty of not less than $10,000 and not more than $100,000 for each such failure.	Signature: _____ Print Name: Franklin D. Hart Title: President Telephone No.: (919) 248-1810 Date: 18-Jun-96
	Authorized for Local Reproduction Standard Form - LLL

DISCLOSURE OF LOBBYING ACTIVITIES

Complete this form to disclose lobbying activities to 31 U.S.C. 1352

10a. FBA, Inc.
1620 L. St., NW, Suite 875
Washington, DC 20036

10b. McNelis, David N.
Kirkland, J. R.